THE FEASIBILITY OF USING COMPUTATIONAL ELECTROMAGNETIC MODELLING FOR THE STUDY OF BACKSCATTER FROM MARINE ICE

by

RICHARD TREMBINSKI

Thesis submitted to the University of Ottawa
in partial Fulfillment of the requirements for the
Master of Applied Science degree in
Electrical Engineering

School of Electrical Engineering and Computer Science
Faculty of Engineering
University of Ottawa

ABSTRACT

Current marine navigation radars are capable of high-resolution imagery of marine ice but are not able to classify the marine ice. Classifying marine ice means identifying the ice as first-year ice, multi-year ice or glacier ice. The latter two ice types are as hard as concrete and capable of damaging even ice hardened vessels such as icebreakers. The Canadian Coast Guard has identified the ability of marine navigation radars to classify marine ice as the single greatest improvement to be made in the safety of Arctic navigation.

This thesis presents new research that improves our understanding of electromagnetic backscatter from marine ice. The goal of this work was two-fold: to demonstrate the feasibility of using commercial computational electromagnetic modelling software to simulate real-world marine ice targets, and to identify an optimum frequency or range of frequencies at which the marine ice targets can be definitively classified.

Engineering models for scattering from electrically large objects made of a highly variable, complex, heterogenous, three-phase mixture of ice, air and brine are developed. To do so, an extensive literature review of the Arctic environment, and the physical and electrical properties of marine ice, is conducted to distill the required geophysical parameters of the three marine ice types of interest in this work. Using well-established dielectric mixing theory, these parameters are applied to homogenize the marine ice and model the target (in the presence of a flat sea halfspace) using a surface integral equation formulation. To reduce the computational resources required to numerically solve the integral equation models using the method of moments, computational electromagnetic modelling studies are conducted to select a suitable seawater halfspace representation and determine if the properties of larger objects can be inferred from scaled down models of the object.

A case study is presented for backscatter from marine ice from 6 to 10 GHz, which explores the effects of frequency on the co- and cross-polarized backscatter intensity (and hence the apparent radar cross-section) of the three marine ice types of interest. Good agreement is found between the co- and cross-polarized backscatter intensity responses found from the engineering model computations and some existing experimental data from real-world marine ice targets.

This work: (a) proves the feasibility of using computational electromagnetic modelling to simulate real-world marine ice targets, providing a new, cost-effective method for the study of backscatter from marine ice; (b) confirms the viability of using cross-polarization as a method of classification; and (c) identifies 10 to 16 GHz as a potential optimal frequency range for the classification of marine ice using dual-polarization radar.

ACKNOWLEDGEMENTS

First and foremost, I would like to thank my family for their love, encouragement and support over the last two years, which made this all possible.

Second, I would like to thank my advisor, Dr. Derek McNamara, for his continuous guidance, mentorship, and most importantly, his time.

My research would not have been possible without major contributions from many partners. I would like to thank everyone at Altair™, Compute Ontario (www.computeontario.ca), West Grid (www.westgrid.ca) and Compute Canada (www.computecanada.ca) for the enabling this research and providing technical support for their software and high performance networks.

A special thanks goes to my colleagues at the Department of National Defence, Quality Engineering and Test Establishment, particularly Dr. Greg Hiltz and Pradiv Sooriyadevan, for allowing me to use their purpose-built high-performance computing cluster. Without this access I would not have been able to complete my thesis on time.

Finally, I would like to acknowledge, and thank, the Department of National Defence and the Royal Canadian Navy for the funding and opportunity to complete this post-graduate study.

TABLE OF CONTENTS

LIST OF TABLES

LIST OF FIGURES

LIST OF SYMBOLS AND ACRONYMS

Symbol	Definition
a_x, a_y, a_z	Semi-axis dimensions of an ellipse
A_{FOV}	Areal field of view in square metres
$\bar{B}$	Magnetic flux density vector in Vs/m^2
c	Speed of light in a vacuum = 299 792 458 m/s
$\bar{D}$	Electric flux density vector in As/m^2 or C/m^2
$\bar{E}$	Electric field vector in V/m
f, f_v	Fractional volume
$\bar{F}$	Electric field intensity in V
G	Gain of the antenna
h_a	Height of the antenna in metres
h_t	Height of the target in metres
$\bar{H}$	Magnetic field vector in A/m
$\bar{J}$	Volume electric current density vector in A/m^2
$\bar{M}$	Volume magnetic current density vector in V/m^2
N	Normality of brine
$N_x, N_y, N_z,$	Depolarization factor
$\bar{P}$	Average electric polarization vector
P_{rx}	Power received by the radar in W
P_{tx}	Transmitted power of the receiver in W
R	Range from the radar to the target
S	Salinity in parts per thousand (ppt)
T	Temperature in °C
V^4	Propagation factor (a unitless value between 0 and 16)
α	Attenuation constant
β_h	Horizontal beamwidth in radians
δ_p	Penetration depth in m
ε	Permittivity in F/m
ε_c	Complex permittivity
ε_{eff}	Effective permittivity
ε_h	Permittivity of the host medium

Symbol	Definition
ε_i	Permittivity of the inclusion
ε_o	Free space permittivity = 8.854×10^{-12} F/m
ε_r	Relative permittivity
ε_s	Relative static permittivity of brine
ε'	Dielectric constant
ε''	Dielectric loss factor
ε_∞	Relative microwave dielectric constant
λ	Wavelength of the electromagnetic wave in metres
λ_o	Free space wavelength in metres
μ	Permeability in H/m
μ_o	Free space permeability in Henries = $4\pi \times 10^{-7}$ H
ρ_{br}	Density of brine in g/cm^3
ρ_e	Electric volume charge density scalar in As/ m^2
ρ_m	Magnetic volume charge density in Vs/ m^2
$\rho_{pure\ ice}$	Density of pure ice in g/cm^3
ρ_{total}	Bulk density of ice in g/cm^3
σ	Conductivity in S/m
σ_{DC}	DC conductivity in S/m
σ_{app}	Apparent radar cross-section
σ_c	Clutter cross-section
σ_t	Radar cross-section of the target
σ^o	Normalized radar cross-section or clutter cross-section per unit area
$\sigma^o{}_{HH}$	Co-polarized normalized radar cross-section
$\sigma^o{}_{HV}$	Cross-polarized normalized radar cross-section
τ	Relaxation time in seconds
τ_0	Pulse width in seconds
v	Free space angular frequency of the electromagnetic wave
v_1	First Debye relaxation frequency in Hz
v_2	Second Debye relaxation frequency in Hz
ω	Angular frequency of the wave in Hz
χ_e	Electric susceptibility of the material

Acronym	Definition
cm	Centimetre
CEM	Computational electromagnetic modelling
CPU	Central processing unit
dB	Decibels
dBsm	Decibel square metres
dBV	Decibel volts
DND	Department of National Defence
FEKO™	Commercial CEM software suite by Altair©
FYI	First-year ice
GB	Gigabytes
GI	Glacier ice
GHz	Gigahertz
HH	Co-polarized signal or radar return
HV	Cross-polarized signal or radar return
kHz	Kilohertz
m	Metre
mm	Millimetre
MHz	Megahertz
MoM	Method of moments
MYI	Multi-year ice
NRCS	Normalized radar cross-section
PEC	Perfect electric conductor
PMC	Perfect magnetic conductor
ppt	Part per thousand
RAM	Random access memory
RCS	Radar cross-section
TB	Terabytes
V	Volts
WMO	World Meteorological Organization

1. INTRODUCTION

This thesis presents new research into the study of electromagnetic modelling and simulation of marine ice for the detection and classification of marine ice by surface-based (specifically marine) radar. This includes the development of reliable, efficient and accurate engineering models of marine ice and the extensive study of microwave scattering from these models using commercially available electromagnetic modelling software. The long-term research goal of which the work in this thesis forms a part is to further the understanding of the link between the physical characteristics and microwave scattering signature of marine ice types, and use this information to develop a specification for a marine radar optimized for ice detection and classification. The frequency range of interest is from 1 to 40 GHz, which is associated with wavelengths from 30cm to 7.5mm.

1.1 Overview and Motivation

Over the past 30 years, the Canadian Arctic has experienced a continued long-term warming trend, resulting in significant reductions in the overall ice cover [1] [2] [3]. As a result, the famed "Northwest Passage" is now open to summer navigation for four to five months of the year. During this period, the Arctic is not completely free of ice. Ice flows of first-year ice and multi-year ice move in and out of the bays and channels throughout the archipelago, pushed by the winds and currents. Glacier ice, such as icebergs, growlers, and bergy bits, may also be present. The multi-year ice and glacier ice are considered hazardous ice, as they can severely damage even ice hardened vessels, such as icebreakers.

With the growing access to the arctic and the resulting increasing interest in arctic tourism, shipping, exploration and research comes increased risk of collisions with hazardous ice. This could result in environmental disasters or loss of life. The primary tool used by ships for the collision avoidance in all weather conditions is the marine navigation radar.

Through an increased understanding of the link between the physical characteristics and the microwave scattering signature of the various types of marine ice, we will be able to develop a specification for a radar capable of not only detecting ice but classifying the ice as either (relatively) "safe" first-year ice, or "hazardous" multi-year ice or glacier ice.

1.2 Research Rationale

The relationship between the physical characteristics of, and microwave scattering by, marine ice has been extensively studied and is well-known from the perspective of satellite-based remote sensing [4] [5]. Although this research and knowledge will be leveraged in this study, it should be noted that the backscatter signature of marine ice for satellite-based radar is not necessarily indicative of scattering from surface-based radar (ie. shipborne radar). Since marine ice has a complex geometry and physical structure, it will experience different scattering effects at low incident angles than at high incident angles. The satellite-based radar remote sensing is concerned with low incident angles (ie. near nadir), whereas marine radar remote sensing is concerned with high incident angles (ie. near 90 degrees). To highlight this difference, surface-based remote sensing often refers to "grazing" angles (eg. 0-5 degrees), instead of "incident" angles (eg. 85-90 degrees). Additionally, satellite remote sensing images large areas, tens or hundreds of square kilometres, as opposed to surface-based radars which have a resolution cell of square metres.

Using computational electromagnetic modelling, this thesis will improve our understanding of the relationship between frequency, polarization and the physical properties of the ice with the goal of improving the classification of ice types by marine radars. This thesis will explore the frequency band from 6 to 10 GHz, to attempt to identify the optimum frequency band for ice classification, postulating that the current dominance of X-band (ie. 10 GHz) in marine radars was solely driven by the technology available at the time shipborne radars came into service in World War II.

It is our hope that this will eventually lead to the development of a purpose-built, marine radars capable of reliably identifying ice hazards, thereby:

- Improving the safety of navigation in the Arctic and North Atlantic maritime regions;
- Reducing the risk of damage to vessel and oil platforms operating in ice prone areas;
- Reducing fuel consumption;
- Reducing the risk of environmental accidents; and
- answering the Canadian Coast Guards' call for a marine radar capable of automatic and reliable detection of hazardous ice using cross-polarization [6].

This research will:

- Provide reliable, efficient and accurate engineering models of marine ice that can be used with commercial computational electromagnetic modelling software to explore scattering from marine ice;
- Provide a better understanding of the relationship between the physical properties and the backscatter signature of ice, at low grazing angles;
- Provide a better understanding of the effect of surface- and volume-scattering phenomena on the backscatter signature of ice targets at low grazing angles;
- Fill the gap in the research by exploring electromagnetic scattering across a wide frequency band (1-40 GHz) and expanding on the current knowledge for specific frequencies (X, S, Ku or Ka-band); and
- Identify a potential optimal frequency range for the classification of ice types between relatively safe first-year ice and hazardous multi-year and glacial ice.

To the best of our knowledge, this will be the first study to develop and validate engineering models implemented using commercial computational electromagnetic modelling (CEM) software, to study the backscatter signature of the various ice types of interest (first-year, multi-year and glacial ice) by surface-based radar.

1.3 Outline of the Thesis

The thesis is divided into the following chapters:

Chapter 1 – Introduction

Chapter 2 – Problem Definition & Background

Chapter 3 – Selection, Organization & Clarification of Technical Background;

Chapter 4 – Model Construction & Methodology;

Chapter 5 – Case Study & Validation;

Chapter 6 – Conclusions & Future Work.

The topics covered in Chapter 2 are somewhat different than those normally included in an engineering thesis. Most people have heard of the Arctic, but most of us who have not experienced the Arctic, truly understand the Arctic environment. This chapter provides important non-technical background to help the reader (and the author) understand the real-world problem being solved, the problem of modelling ice and the environment being modelled. At the very least, all readers unfamiliar with the study of marine ice and Arctic navigation should read Sections 2.3 and 2.4, which will provide a summary of the nomenclature used in the literature and throughout this work.

Before the electromagnetic (back)scattering from an ice object can be computed, the properties (namely the effective complex permittivity) of the object needs to be specified. Marine ice is a complex heterogeneous mixture of ice, air and seawater brine (dielectric materials). The effective permittivity can be found analytically using dielectric mixing formulas, but requires knowledge of the geophysical and electrical properties of the marine ice and the environment in order to do so. These geophysical and electrical properties must be obtained experimentally. Chapter 3 provides an extensive review of the current experimental research related to marine ice and the Arctic environment. Enough information has been included here to allow the reader to identify a time of year and select the appropriate geophysical parameters to define the effective complex permittivity of first-year ice, multi-year ice and glacier ice. Chapter 3 also discusses the theory related to radar cross-section, scattering phenomena and wave polarization which will be used in the discussion of the results in Chapter 5. Finally, Chapter 3 presents the most current experimental research in the area of surface-based radar remote sensing of marine ice, which will be used in the discussions in Chapter 5 to validate the engineering models.

Chapter 4 summarizes the selected geophysical and electrical properties for three marine ice types of interest and applies the appropriate dielectric mixing theory, presented in Chapter 3, to calculate the effective permittivity of the three marine ice types across the frequency band of interest. Finally, the engineering electromagnetic scattering models for the three marine ice types are constructed and tested. This includes determining the appropriate mesh size, the halfspace representation of the sea surface and the geometrical size of the ice objects, to minimize the computational resources while ensuring sufficient accuracy for the analysis of backscatter from marine ice.

With the methodology established, the engineering models are applied in Chapter 5 to study the backscatter from marine ice from 6 to 10 GHz. Specifically, the backscatter signatures for the three marine ice types are compared to determine the suitability of each frequency for the use of cross-polarization as a method of classification. The results are then discussed and validated against the most current experimental research presented in Section 3.11.

Finally, Chapter 6 highlights the key findings of this thesis, the contributions made to this area of research and suggests some areas for future work. The major findings and contributions of this work are as follows:

- Developed and validated, a reliable and efficient methodology for building engineering models of marine ice for use in computational electromagnetic modelling;
- Proved the feasibility of using computational electromagnetic modelling to study backscattering from marine ice;
- Demonstrated that dual polarization radar has the potential to be used to classify marine ice as either “safe” ice (first-year ice) or “hazardous” ice (multi-year ice or glacier ice) at 10 GHz with a confidence level of approximately 85%; and
- Showed that the trend suggests the optimal frequency for ice classification using dual polarization radar exists between 10 and 16 GHz.

2. PROBLEM DEFINITION & BACKGROUND

2.1 Introduction

This chapter is organized into the following sections:

Section 2.2 – The Arctic Environment;

Section 2.3 – Ice Nomenclature;

Section 2.4 – Ice Navigation;

Section 2.5 – Ice Surveillance;

Section 2.6 – Surface-based Radar; and

Section 2.7 – Conclusions.

This chapter provides non-technical background information and the motivation for this work. Section 2.2 provides a brief history of the North-West Passage and the environmental changes that have opened up the famed passage to navigation. Section 2.3 presents the nomenclature that is commonly used in the study of marine ice and will be used throughout this thesis. Finally, Sections 2.4 through 2.7 outline the problem being solved and the motivation for this work.

2.2 The Arctic Environment

The first recorded expedition into the Canadian Arctic was conducted by Martin Frobisher in 1576. The most notable expedition was the Great Northern Expedition by Vitus Bering in 1733, who first attempted to find a "North-West Passage" between the Atlantic and Pacific Oceans. Bering concluded that the route was not navigable due to the sea ice[1] cover. This remained the case until recently.

Over the past 30 years, as shown in Figure 2.1, the Canadian Arctic has experienced a long-term warming trend, resulting in a significant reduction in the overall age and extent of the ice pack. In

---

[1] As will be discussed in Section 2.3, "sea ice" will refer specifically to ice that forms at sea from seawater. "Marine ice" will be the collective term to refer to all ice found at sea, which includes sea ice and glacier ice (eg. icebergs) formed on land from fresh water.

2017, the thicker, multi-year ice pack accounted for only 21% of the overall ice extent compared to 45% in 1985. The minimum sea ice extent at the end of the summer of 2016 tied the 2007 record as the second lowest since satellite recording started in 1979 [1] [2]. Along with the reduced ice extent, the Arctic is also experiencing an overall increase in average annual temperature. During the winter of 2017/2018, the average temperatures in the Arctic were 15°C higher than normal, reaching a high of +6.2°C [3].

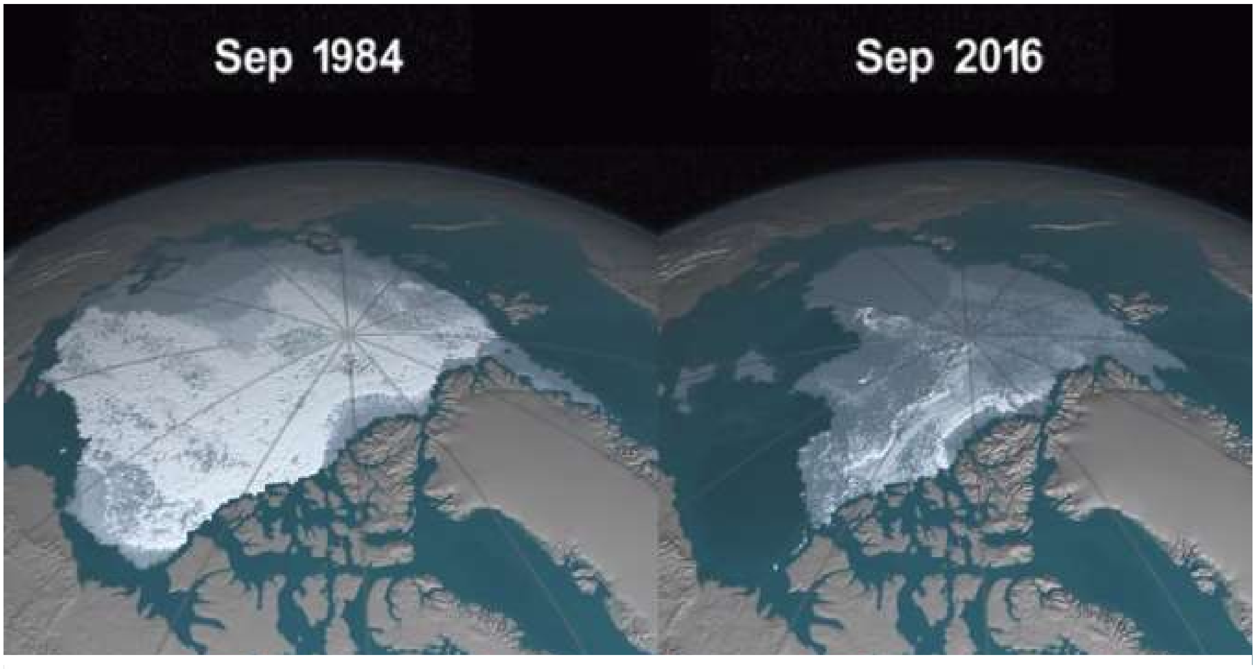

Figure 2.1: Arctic ice pack comparison between 1984 and 2016. The white ice image denotes 4+ year old ice and the darkest grey ice denotes 1st year ice. Image courtesy of the NASA Goddard Space Flight Center [1].

This overall trend is expected to continue and has opened the famed "Northwest Passage" to navigation, from as early as May and continuing until September or October, generating considerable commercial interest in this sea route. The number of complete transits of the Northwest Passage annually has steadily increased from 4 per year in the 1980s to 20-30 since 2009. In the past, the majority of the vessels operating in the Arctic were coast guard icebreakers and research vessels. In the 1980s and 1990s, the Arctic became an area of interest to the oil and gas and mining industries. However, today, the majority of vessel traffic is small pleasure crafts, passenger ships, and cargo and supply tugs [7]. In addition to these transits, there are hundreds of oil and gas exploration and supply ships conducting partial transits of the arctic. Interest is also being shown in the commercial shipping industry, particularly China, the world's largest exporter. The shipping route from Europe to East Asia through the Northwest Passage is just over 9,000 kilometres shorter than the route through the Suez Canal [8]. In 2017, there was a record high 33 full transits, including full transits by a cruise ship carrying 1500 passengers [9]. Interest in this sea route is only going to continue, such that the number of ships transiting the Northwest Passage by 2020-2025 is projected to be in the hundreds [10].

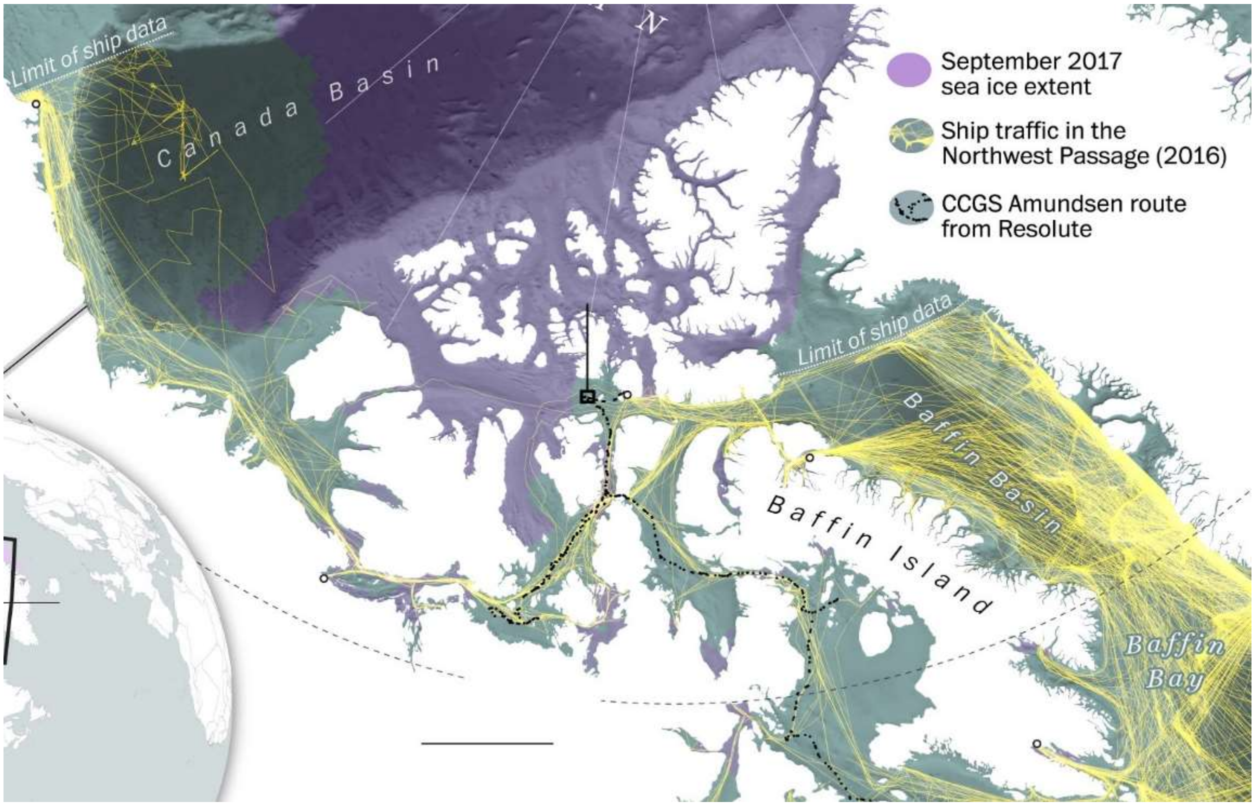

Figure 2.2: Northwest Passage traffic pattern map for 2016. Image courtesy of [9].

2.3 Ice Nomenclature

Before a discussion of the physical and electrical properties of ice and the ability of a radar to detect and classify the ice types of interest can take place, it is important to understand the nomenclature used in the study of ice.

There are six main types of ice found in the marine environment: new ice, nilas, young ice, first-year ice, multi-year ice and glacier ice. The first five are formed from salt water and are referred to collectively as "sea ice". The latter, glacier ice, is formed on land from decades of accumulation and compaction of fresh water precipitation and breaks off from a glacier and floats out to sea. It is called "ice from land origins" or glacier ice [11]. However, often in the literature, glacier ice floating at sea is included in the collective term "sea ice". In this thesis, the distinction between sea ice and glacier ice will be maintained, as the origins and physical differences have significant influence. The term "marine ice" will be used to include sea ice and glacier ice. Although new ice, nilas and young ice are mentioned in this discussion, the ice types of interest and the focus of the engineering models presented here are first-year ice, multi-year ice and glacier ice. Multi-year ice and glacier ice will be referred to as "hazardous ice" and are of primary concern in navigation and this work. Engineering models of first-year ice will also be presented and are necessary for comparison in order to classify or discern between the relatively "safe" first-year ice and hazardous ice. The reasoning for grouping first-year ice as safe ice and multi-year and glacier ice as hazardous ice will become apparent in discussion of Section 2.3 and Chapter 3.

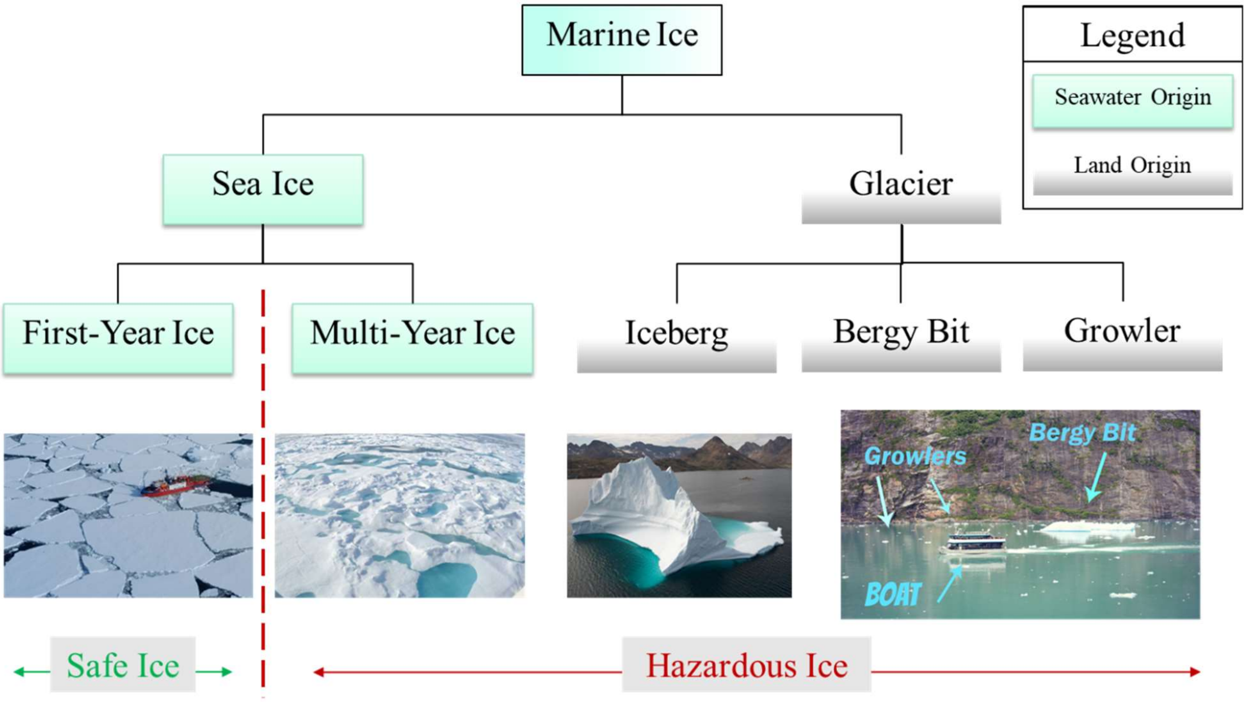

Figure 2.3 Classifications of Marine Ice types of interest to this work.

The following definitions are based on the World Meteorological Organization Sea Ice Nomenclature [12].

New ice and *nilas* are less than 10 cm thick. They are newly formed, high salinity sea ice, which can be easily broken or pushed aside by small vessels. *Young ice* is between 10-30 cm thick, similar to first-year ice in physical structure and easy to break by ice hardened vessels. When broken, this ice tends to raft or ridge. These three ice types are not of concern in this work because they are formed in the Fall/Winter months when the navigation season ends. By the start of the next navigation season, this ice has become first-year ice.

First-year ice (FYI) is sea ice that has formed over one winter's growth and developed from young ice. First-year ice is between 30 cm and 2 m thick. FYI is relatively soft due to brine and air inclusions within the ice, and generally would not damage an ice-strengthened vessel operating with due caution but could significantly impede a vessels progress by hours or even days [11]. FYI is sometimes referred to as "residual ice"[2].

Multi-year ice (MYI) is formed from FYI that has survived at least one summer melt. During the summer melt process, the brine and air pockets that characterize first-year ice are replaced with melt water that then freezes, leaving a clear, dense mass of ice. MYI is normally between 2-4 m

---

[2] This term is used in place of first-year ice in the southern hemisphere ice around Antarctica.

thick, can be as hard as, or harder than, concrete and is capable of damaging even ice-strengthened vessels. MYI is sometimes referred to as "old ice" in the literature or as "second-year ice" if it has only survived one summer melt.

A *floe* refers to any contiguous piece of sea ice ranging from tens of metres up to 10 km across and can be comprised of FYI, MYI ice or glacier ice. Floes larger than 10 km across are called "ice fields".

Glacier ice (GI) is ice from a glacier, whether it is land based or floating at sea. This ice is formed on land from decades of fresh water snow and ice accumulation. GI is very dense and very hard fresh water ice that can cause considerable damage to any vessel in a collision. In this work, we are interested in glacier ice that has broken off or "calved" from the glacier in the form of icebergs, bergy bits and growlers. When the term "glacier ice" is used, it will be referring only to the floating form.

Icebergs are formed when GI, which has extended into the ocean, calves off the glacier and floats away from shore. These icebergs can be 10s of metres (icebergs) to 100s of metres across (ice islands). They can be grounded and stationary or drifting and driven by the wind and currents. As an iceberg drifts into warmer environments (air and water), it begins to decay (melt) or crack and break into several smaller icebergs, bergy bits or growlers.

A *bergy bit* is a large piece of GI that protrudes between 1 m and 5 m above the surface and normally between 100 to 300 m^2 in area. They may be the remnants of a melting iceberg or may have broken off an iceberg.

A *growler* is a piece of glacier ice that protrudes no more than 1 m above the surface and normally occupies an area of about 20 m^2. They may be the remnants of a melting iceberg or bergy bit or may have broken off an iceberg.

Bergy bits and growlers are especially dangerous to ships because they are extremely difficult to detect [11] with an estimated apparent radar cross-section[3] in the range of 1/100th of their physical cross-sectional area.

Table 2.1: Classification of glacier ice types by size with approximate equivalent Radar Cross-Section (RCS). Reproduced from Tables 5.1 and 5.2 of [15].

Size	Height (m)		Length (m)		Radar Cross-Section (m^2)	Projected Area (m^2)
	Tabular	Other	Tabular	Other		
Growler		<1		<6	0.01-0.10	2
Bergy Bit		1-5		6-20	0.5-1.0	60
Small Iceberg	<6	5-15	<90	20-60	5-10	400
Medium Iceberg	6-15	15-45	90-120	60-120		
Large Iceberg	>15	45-75	>120	120-210		
Very Large Iceberg	>75		>210			

---

[3] The definition and applicability of apparent radar cross-section and radar cross-section will be discussed in Section 3.8.

2.4 Ice Navigation

The majority of the Northwest Passage is in perpetual daylight from April to September, but fog, snow and poor visibility are common during this period. Although the ice pack melts and recedes during the summer months, ice floes pushed by wind and current move in and out of the channels, making open channels quickly ice-filled. The greatest risk to navigation is not just navigating through first-year ice (FYI), multi-year ice (MYI) or glaicier ice (GI), but through relatively safe FYI with MYI or glacier ice inclusions. Even ice strengthened vessels such as icebreakers are at risk of hull damage due to collisions with hard, multi-year and glacier ice within relatively softer first-year ice floes. A bergy bit can weigh between 500 and 5,400 tonnes [13], and be as hard as concrete[4]. Reference [14] indicates that 75% of the reported ship damage in the Arctic was the result of contact with multi-year ice and that the ability to detect MYI is the major issue facing year-round shipping in Arctic. Finally, breaking even first-year ice is slow and costly in terms of fuel: it is more efficient to transit in open water, even if it adds hundreds of miles [6].

2.5 Ice Surveillance

To assist vessels operating in the Arctic and ice inhabited waters, ice surveillance systems have been developed by many countries, which integrate a variety of satellite, aerial and surface sensors to create ice charts. Each Arctic country is responsible for their territorial waters. In Canada, the Canadian Ice Services produces ice charts, updated weekly in the winter months and daily in the summer months[5]. These charts are updated from satellite-based systems (Synthetic Aperture Radar and Infrared) and airborne systems (Side-Looking Airborne Radar or Synthetic Aperture Radar). Satellite surveillance is currently offered by RadarSat 1 and 2. Each satellite has a 3 day revisit period in order to image the Canadian Arctic, but can provide daily imaging if necessary of a limited area. In 2018, the RadarSat Constellation, a constellation of 3 satellites, will be able to provide daily imaging of the entire Arctic region and 90% of the globe. However, post-processing and production of ice charts will cause up to a 1 week latency for higher resolution imaging. For tactical level route transits, airborne systems can be used to fly ahead and provide more timely updates. However, due to the limited number of SLAR systems and the vast area of the Canadian archipelago, airborne surveillance is subject to limited availability [15]. Due to the time latency of these charts, such charts are only useful for strategic level route planning. In the end, the marine radar must be used to identify ice features on the ice charts and confirm their validity. Both satellite and airborne systems can provide false positives or fail to detect low RCS glacier ice targets. Hence, the marine radar is the primary sensor, for 24/7 monitoring of the current ice conditions, to detect and avoid hazardous ice in the vicinity of vessels operating in the Arctic.

---

[4] Timco and Frederking [90] measured compressive strengths up to 17.3 MPa. Concrete is between 17 and 28 MPa.

[5] Determined by the author by reviewing the ice chart archives available from Canadian Ice Services at https://www.canada.ca/en/environment-climate-change/services/ice-forecasts-observations/latest-conditions/archive-overview.html

2.6Surface-based Radar

The first marine radar was brought into service in World War II, following the development of the cavity magnetron in Great Britain. This advancement allowed radar equipment and antennas to be made small enough to be installed on ships. The first recorded marine navigation radar was an X-band radar installed on the USS Semmes in 1941. By 1942, X-band navigation radars were being widely used by Allied warships escorting conveys across the Atlantic [16]. In 1943, the first recorded use of marine radar for ice navigation took place on the United States Coast Guard icebreaker “Storis”, which was escorting a military troop carrier through the ice fields off Greenland using an X-band navigation radar [17]. After World War II, thousands of surplus radars were installed on commercial ships. From 1943 to 1970, all commercial marine navigation radar research was focused on improving the ability to detect and track relatively large RCS targets, such as ships.

In the 1970s, research into using marine radar for iceberg detection was driven by the oil and gas industry. Typically, over 400 icebergs a year drift south of the 48th parallel along a path from Greenland to Newfoundland called “Iceberg Alley” [3, p. 12]. These icebergs endanger oil platforms and shipping operating in the North Atlantic. In the case of drilling platforms, such as oil rigs like Hibernia, icebergs can cause shut-downs as platforms are moved to avoid collisions with icebergs. As a result of the discovery of the Hibernia oil reserves, research intensified during the 1980s [15, pp. 100-102]. However, in 1987, Lewis et al [18] concluded that the surface-based ice detection radar system requirements are “being met, albeit poorly, with existing (or slightly modified) off-the-shelf marine radar systems”. It was not until the 1990s that significant advances were made in the ability to detect and image ice features, such as edges and ridges or lead (open water) in the ice, through the development of enhanced digital processing techniques and advanced computing. This research was funded by Canadian Department of Fisheries and Oceans, and included contracts with Sigma Engineering (now called Rutter) [19], Raytheon [20], Enfotech (now called FedNav) [21] and the Communications Research Laboratory at McMaster University [13]. Despite the research efforts and improvements made in the 1990s, the Canadian Coast Guard [6] in 2016, and the United States based National Petrolium Council [22] in 2015, both reported that “a major gap in the capability of current technology” still exists in the ability of surface-based radar to: (1) detect small ice contacts (growlers and bergy bits) within an ice floe and (2) automatically and reliably distinguish between first-year and hazardous multi-year ice or glacier ice.

To date, the research related to surface-based radar remote sensing of marine ice has centred on improving the ability of existing X-band or S-band marine radars to detect ice targets, with some studies expanded to the use of Ka or Ku-band marine radars [17]. This research has been limited to modifying these existing radars to use dual-polarization and advanced digital processing techniques to provide better imaging and display of the radar picture [15]. Two marine radars are currently available that are specifically designed and marketed as ice navigation radars: the Rutter sigma S6 Ice Navigator [23], and the Sea-Hawk line of polarimetric radars [24]. Both are based on existing X-band marine radars and are modified with advanced digital processing. The Rutter

Ice Navigator depends solely on advanced digital processing, whereas the Sea-Hawk uses dual polarization. These enhanced marine radars provide a higher definition image of the ice that allows an experienced operator to identify certain ice features, but do not reliably and automatically distinguish between safe ice (FYI) and hazardous ice (MYI or GI) [6].

2.7 Conclusions

The selection of X-band appears to be based on historical factors and standardization as opposed to performance against ice targets. Advanced digital processing has provided better fidelity of the radar image but has not improved the ability to classify ice. Although the use of dual-polarization to classify ice was first researched in the 1990s, it has not been fully explored or become widely used. It is postulated that constraining the research to experimentation with modified X-band radars has limited progress in developing a surface-based radar system that can reliably classify ice targets. This thesis will develop engineering models for the study of backscattering from marine ice using computational electromagnetic modelling (CEM). The motivation behind this work is to improve our knowledge of backscattering from marine ice and, hopefully, to identify the optimal frequency or frequency range to utilize the polarization of the backscattered field to definitively classify marine ice as safe ice (FYI) or hazardous ice (MYI and GI). And, in doing so, improve the safety of people and ships navigating the pristine waters of the Canadian Arctic.

3 SELECTION, ORGANIZATION & CLARIFICATION OF TECHNICAL BACKGROUND

3.1 Introduction

This chapter is organized into the following sections:

Section 3.2 – Environmental Conditions during the Arctic navigation season;
Section 3.3 – Physical Properties of Marine ice;
Section 3.4 – Permittivity;
Section 3.5 – Dielectric Mixing Theory;
Section 3.6 – Electrical Properties of Marine ice Constituents;
Section 3.7 – Method of Moments Integral Equation Solution;
Section 3.8 – Backscatter Intensity, Radar Cross Section and Apparent Radar Cross Section;
Section 3.9 – Scattering Phenomena;
Section 3.10 – Polarization;
Section 3.11 – Existing Experimental Knowledge on Scattering from Marine Ice; and
Section 3.12 – Conclusions.

Before an engineering model of marine ice for electromagnetic analysis can be developed and validated, it is necessary to understand the physical structure and electrical properties of the various types of marine ice. In Sections 3.2 through 3.6 this chapter pulls together the scientific literature on the properties of marine ice (and the surrounding sea) and on the so-called mixing theory for dielectrics. This will allow us to represent ice (with electrically small inclusions) as a homogeneous lossy dielectric. In Chapter 4, this will be applied to determine an effective complex permittivity for the three marine ice types of interest: namely First-Year Ice (FYI), Multi-Year Ice (MYI) and Glacier Ice (GI). This will enable the development of the engineering models[6] for electromagnetic scattering from marine ice in the presence of a flat sea.

The computational electromagnetics approach used to implement the engineering models code is briefly reviewed in Section 3.7. This at once allows, in Section 3.8, to clarify and connect otherwise seemingly disparate definitions of various radar cross section related concepts. This will in turn permit us, in Chapter 5, to use existing experimental data on scattering from marine ice, to validate

---

[6] We refer to them as “engineering models” because they will be setup to reliably determine only what we need for the problem at hand, namely far-zone scattering from marine ice, and not for other purposes “microscopic” purposes.

the scattering results obtained using the computational electromagnetics models. Section 3.9 describes how computational or measured scattering data are often interpreted in terms of various "scattering phenomena". Because the polarization of the scattered fields will be important in Chapters 4 and 5, Section 3.10 is included to remind us what is meant.

The measured data referred to above, taken from the most recent experimental research in surface-based radar remote sensing of marine ice, is summarized in Section 3.11 for later convenience.

Section 3.12 concludes the chapter and serves to delineate the contributions of the present chapter.

3.2 Environmental Conditions

As stated in Chapter 2, the Northwest Passage is navigable (relatively ice free) from as early as June until October. Timco and Johnston [25] recorded average surface air temperatures of -10°C in May, -5° to 0°C in June, and +2 to +5 in July. The surface air temperature during the summer melt period averages between -1°C to +4°C, and the sea surface temperature ranges between -2°C (the freezing point of seawater) to +4°C [26].

The salinity of the world's oceans is remarkably uniform in the concentration and composition of salts. There are localized and temporary fluctuations due to rain, outflows of rivers or run-off from land, but the average salinity of 34.48 ppt (parts per thousand) varies little from ocean to ocean [27, p. 11]. This is shown graphically in Figure 3.1.

In the littoral environment of the Canadian Arctic, the salinity of seawater at the surface can vary between 28 ppt, in proximity to the shore, to 33 ppt in the Canadian and Eurasian Basins as shown in Figure 3.2 [26].

In the models for this work, the air and seawater surrounding the marine ice, and the seawater at the surface which will interact with the incident and scattered fields, are of interest. These environmental conditions will be applied to the engineering models in Chapter 4 to determine the effective permittivity for those conditions.

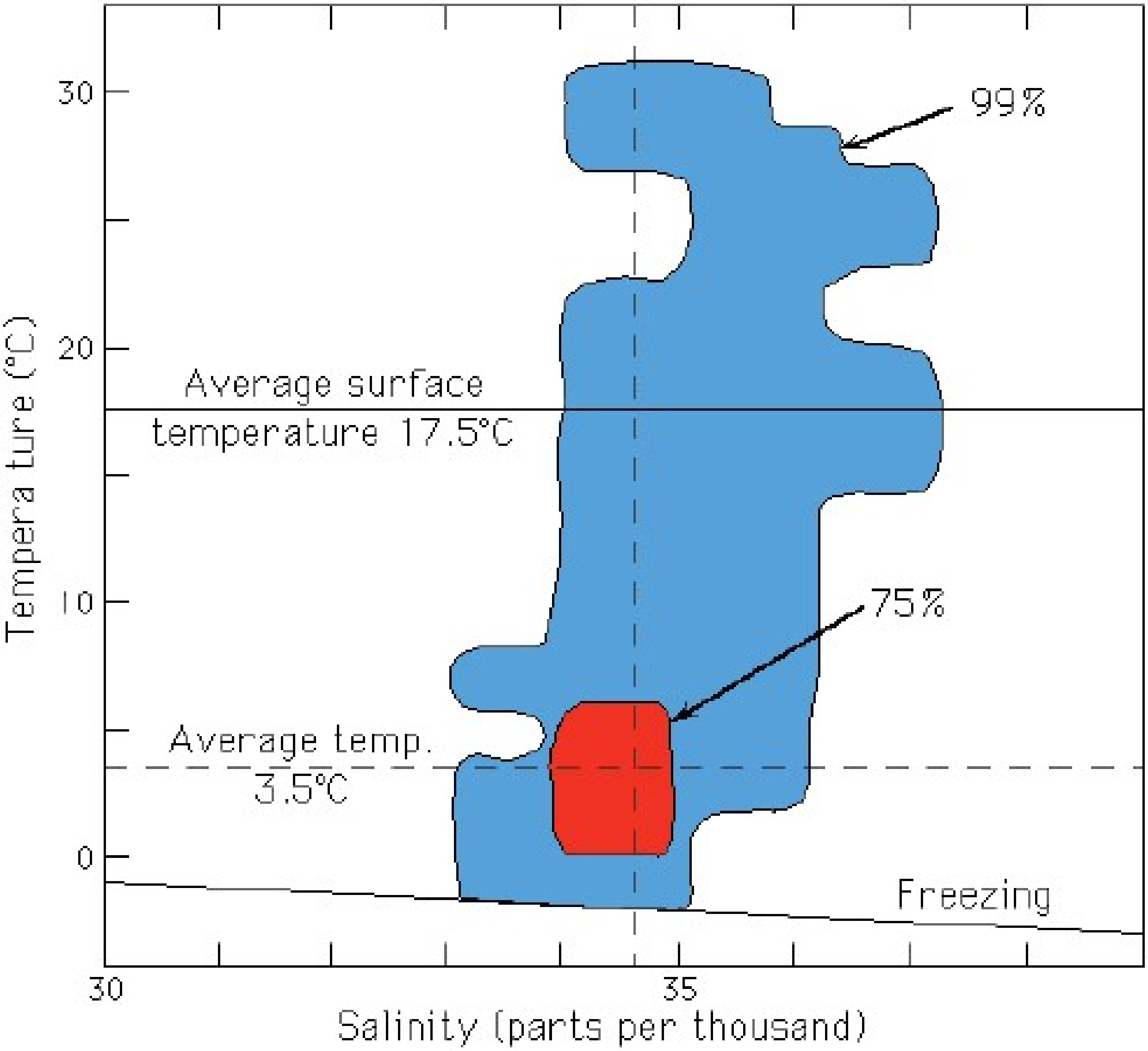

Figure 3.1: Average salinity and temperature variance of the world's oceans. The temperature and salinity of 99% of the world's oceans is represented in blue, with 75% of the world's oceans represented in red.

Courtesy of: https://www.soest.hawaii.edu/oceanography/courses/OCN623/Spring%202015/Salinity2015web.pdf (Accessed 14 September 2018)

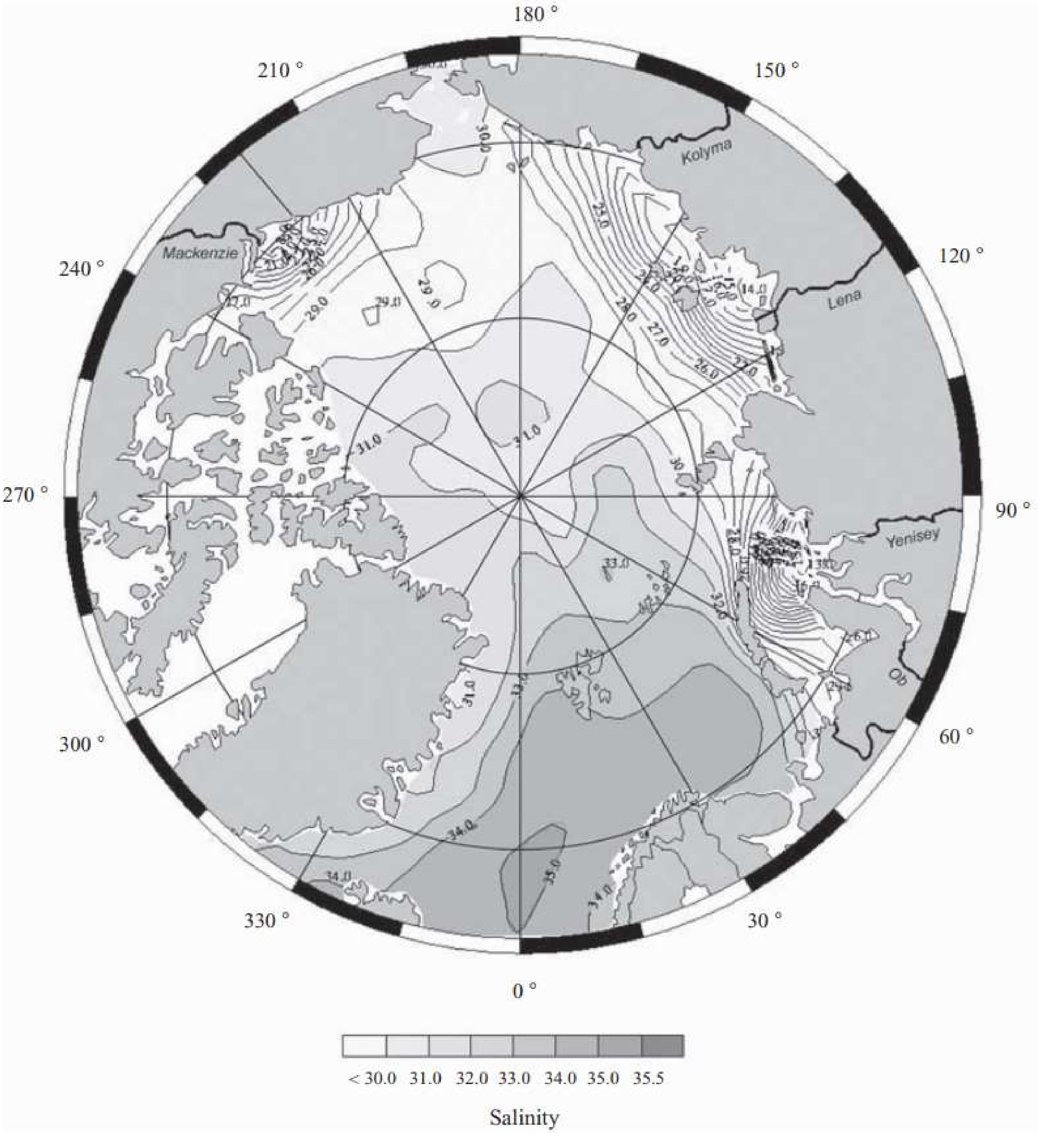

Figure 3.2: Map of the Arctic region showing average sea surface salinity in parts per thousand.

Courtesy of: Serreze, M., & Barry R. The Arctic Climate System. Cambridge University Press, New York, NY, 2005. Ch 2. (Accessed 29 July 2018).

3.3 Physical Properties of Ice

As stated earlier, a detailed understanding of the physical properties of marine ice are necessary to model and analyze microwave scattering from marine ice. This section will focus on describing the physical properties of marine ice on a macroscopic scale, including the formation of FYI and its transition to MYI as it pertains to their physical properties, as they relate to the models that will be developed in Chapter 4. The formation of glacier ice will not be discussed to the same level of detail, but the physical differences, compared to MYI, will be discussed.

The growth, structure and physical properties have been an area of significant research since about the 1950s, with much of the definitive work coming from the U.S. Army Cold Regions Research and Engineering Laboratory (CRREL) by the likes of Frankenstein and Garner [28], Weeks and Ackley [29], Cox and Weeks [30], and Arcone, Gow and McGrew [31] [32], or the National Research Council of Canada by the likes of Vant, Gray, Ramseier & Makios [33] [34], Nakawo and Sinha [35], and Johnston and Timco [14]. Weeks and Ackley [29] provide an excellent review of the key works and their findings up to 1982, along with in depth descriptions of the growth, structure, physical properties and electrical properties of marine ice. These works, based on experimental observation, are the main references for the physical model on which the mixing theories were applied to determine the effective permittivity of various ice types. The measurement data collected by Vant, Ramseier and Makios [34] will be used in Chapter 4 to validate the effective permittivities calculated using mixing theory.

3.3.1 First-year Ice

The specific gravity of seawater is 1.026 g/cm^3 at the freezing temperature. As seawater cools, its specific gravity increases slightly to a maximum at approximately 2°C then begins to decrease slightly as the temperature decreases from 2°C to the freezing point of approximately -1.8°C [35]. Due to this property, the warm water at the surface will float above the cooler water below until it is cooled to 2°C. The surface water then descends into the "mixing layer" and is replaced with warm water from below through a convection process. Once the mixing layer reaches a uniform temperature of 2°C, the convection process ceases, and the water at the surface again becomes more buoyant and begins to cool below 2°C. At the freezing point of -1.8°C, water transitions from the liquid state to the solid state of ice, and the specific gravity decreases significantly (approximately 9%) to approximately 0.92 g/cm^3. This unusual, but not unique, characteristic allows ice to float [29] [13, pp. 22-26], and influences the formation and growth of sea ice.

Ice is a very selective crystalline structure that forms a lattice of oxygen and hydrogen ions (ie. pure water) and rejects impurities[7], such as biological materials and salts. Initially, the ice crystals form in a randomly oriented lattice but as the ice congeals into a sheet, the crystals lose a degree

---

[7] There are ions from the components of salts found in seawater which could replace oxygen atoms in the lattice, but these do not exist naturally in significant quantities in seawater to displace oxygen atoms in sea ice [29].

of freedom and begin to grow vertically downward into the water column [13, p. 23]. The impurities are trapped in small spherical inclusions called pockets as the ice congeals. As the water in the brine freezes and rejects the salt back into the remaining liquid, the salinity of the brine in suspension becomes concentrated and can be as high as 225 ppt [36] [27, pp. 11-13]. The salinity of these "brine pockets" is a function of temperature, such that the freezing point of the brine is in equilibrium with the temperature of the surrounding ice [37].

The overall bulk ice salinity[8] of the ice is a factor of the air temperature, growth rate and age of the ice, and initially ranges between 10 to 25 ppt [29], but can reach as high as 50 ppt [35]. As the ice ages, it experiences desalination due to two processes: gravity drainage and brine pocket migration[9]. This desalination is initially very rapid, dropping to 8 to 10 ppt in the first week, then slows to about 0.5 ppt per month, eventually stabilizing at between 4 to 8 ppt [35]. As the ice thickens, the portion of ice above sea level will experience drainage, as the brine pockets migrate to cracks in the ice and drain downward due to gravity, leaving air inclusions in the ice. Any brine pockets trapped in the bulk ice will also migrate downward due to gravity and a melting process caused by the temperature gradient in the ice. During the growth season, the temperature gradient has been shown to be a linear function between the surface temperature and the water temperature [35]. The ice at the surface is equal to or slightly warmer than the air temperature (as cold as -30° to -40°C in the Arctic during the winter freeze up season) and the ice at the bottom of the ice sheet is always at the freezing temperature of -1.8°C [38]. If the temperature of the ice at the top of a brine pocket is below the freezing point of the brine, the water in the brine will freeze, rejecting the salt and increase the concentration of salts in the brine pocket. Due to the slight temperature gradient, the ice temperature at the bottom of the brine pocket will be above the freezing temperature of the brine and the ice will melt, causing the brine pocket to migrate downward [27, pp. 26-27]. As stated earlier, the concentration of salt in the brine pockets is directly related to the ice temperature surrounding the brine and is equal to the concentration at which the freezing point is equal to the surrounding ice temperature. It is the brine and air inclusions that cause FYI to be relatively soft and easy to break by ice-strengthened vessels, such as icebreakers.

During the summer melt period, the temperature gradient in the marine ice exhibits a "C-shape", with the upper layer of ice (the air/ice interface) equal to or slightly higher than the air temperature (at or above freezing), the bulk ice below freezing and the bottom of the ice sheet (the ice/seawater interface) at the freezing point of -1.8°C. Further desalination takes places during this period through a process called flushing. Flushing is a form of gravity drainage but is considered separate and occurs when freshwater melt from the top of the ice floe drains into the cracks, diluting and displacing the brine. Since freshwater is less dense than the brine, it will float on top. The head pressure of the freshwater will force the brine downward, flushing it out of the upper layers of the

---

[8] Note that bulk ice salinity refers to the percentage of salt with respect to the overall volume of the ice, as opposed to the salinity of the brine in the brine inclusions mentioned previously (percentage of salt with respect to the volume of the brine).

[9] The mechanism of brine pocket migration was first published by W.G. Whitman in 1926. Arctic explorers had noticed that newly formed sea ice was too salty for cooking or drinking purposes but that later in the season first-year ice contained less salt. Furthermore, multi-year ice contained so little salt that it could be melted and used as drinking water [40].

ice [29]. As a result, the bulk ice salinity of FYI during the summer months is between 0.5 to 4 ppt [38] [39].

At the beginning of the navigation season, FYI is between 1 and 2 metres thick, floating about 0.1-0.2 m above sea level. It can have a thin snow layer with a smooth surface in May. The edges of the FYI floe normally have a sharp, angular appearance. Any pressure cracks will also have an angular appearance [12] [41]. By June, FYI may have thinned and developed a regular pattern of numerous melt ponds interspersed with low mounds. There are normally no defined drainage channels connecting the melt ponds. In July, the freshwater ponds begin draining through cracks in the ice floe and by August, the ice floe begins to break-up [25].

The density of FYI has been found to be between 0.91-0.96 grams/centimeter^3 [13] [29]. Upon initial formation, the density is likely to be at the upper limit. As the ice ages and desalinization takes place, the higher specific density brine is replaced by lower density pure ice and air, such that the density of FYI will be near the lower limit.

In mixing theory, as will be shown in Section 3.5, the internal structure of the ice, including the size, shape, orientation and density of the inclusions is important. Internally, as stated above, the FYI consists of pure ice as the host medium with inclusions of brine and air pockets. The air pockets are spherical. The brine pockets in the top layer are slightly flattened spheres with an axial ratio of 1:1:0.5 upon initial formation of FYI [29]. As the ice ages and the brine pockets migrate, they elongate and become long needle-like vertically aligned ellipsoids. However, there does not seem to be complete consensus on the exact size of the brine pockets. Vant et al. [34] report that the brine pockets are approximately 3-5mm long with a diameter of 0.05 mm, whereas Weeks and Ackley [29] quote Addison [42] as finding the brine pockets to be between 2-3cm long (approximately 10x longer) with a diameter of 0.05mm. These values equate to an axial ratio for the brine pockets of 1:1:60 or greater. Weeks and Ackley [29] also report their findings that the axial ratio is 1:5:30, and Sihvola [43] shows good correlation between the measured permittivity of FYI and the effective permittivity using mixing theory for an axial ratio of 1:1:60. With respect to orientation, Vant et al. [34] found that modelling the orientation of the brine inclusions at 45° from vertical provided the best correlation with their experimental results. However, this may be because the top 5-10cm of the FYI tends to have randomly oriented brine inclusions, whereas the lower layers of columnar ice have vertically oriented brine inclusions [38]. The results for 45° angled inclusions are very similarly to randomly oriented elliptical inclusions and spherical inclusions. In mid-winter, the fractional volume of the air to the total volume of the FYI is approximately 1.5% and the fractional volume of the brine is approximately 11% [34]. As desalination occurs, the fractional volume of air will increase, and the fraction volume of brine will decrease to more resemble MYI ice.

In Sections 4.4 and 4.5, the understanding of how FYI decays during the summer melting period will be applied to make informed decisions on the selection of the geophysical properties of FYI: specifically, the temperature profile, density and salinity. Finally, the knowledge of the structure and orientation of the inclusions will inform the decision on the appropriate mixing theory to calculate a suitable effective permittivity to homogenize FYI.

3.3.2 Multi-Year Ice

Multi-year ice is formed from FYI that has experienced one or more melt-refreeze cycles. During the summer melt period, the FYI experiences preferential melting under the melt ponds, deepening the depression in the ice. Near the end of the melt season, cracks in the ice expand into drainage holes and the freshwater melt will flush out most of the remaining brine. Since ice is more buoyant than water and fresh water is more buoyant than seawater, a layer of freshwater melt will form below the ice floe.

In the winter ice growth period, the freshwater melt (on top of the ice, in the cracks and below the ice floe) will recrystallize, leaving essentially pure ice with small air inclusions. The recrystallized ice consists of a randomly oriented crystalline structure. The bulk salinity of MYI is greatly reduced by this flushing mechanism, such that the bulk ice salinity above sea level is normally <1 ppt and 2 to 6.3 ppt below areas of depression or within the ice bulk below sea level [44]. As with FYI, the air inclusions are spherical, and the brine inclusions are elliptical.

MYI is typically between 3-5m thick with deep, well defined depressions and hummocks 1-2 m (sometimes as high as 4m) above sea level [27, pp. 28-29]. In early summer, MYI often has a thick snow cover and a "hill and dale" appearance. The hummocks are normally rounded, with gradually sloping sides, due to previous melt cycles, snow drifting and weathering. In late summer, due to the thicker snow cover from the winter, it may retain a snow cover on the hummocks. MYI will have large, irregularly shaped and spaced, melt ponds interconnected by well-established drainage channels [14]. MYI floes will normally have rounded edges and surface features, and may have a turquoise blue appearance, but this is not a definitive feature of MYI [41].

Figure 3.3 Examples of multi-year ice. Left: A large multi-year ice floe, approximately 200m in diameter, with an 8m thick hummock with a well-defined peak and steep slopes, and large irregularly shaped and spaced ponding joined by drainage channels. Image courtesy of Johnston & Timco 2008. Right: Small multi-year ice floe, approximately 5-6m in diameter, with a low freeboard, making it very difficult to detect by surface-based radar.

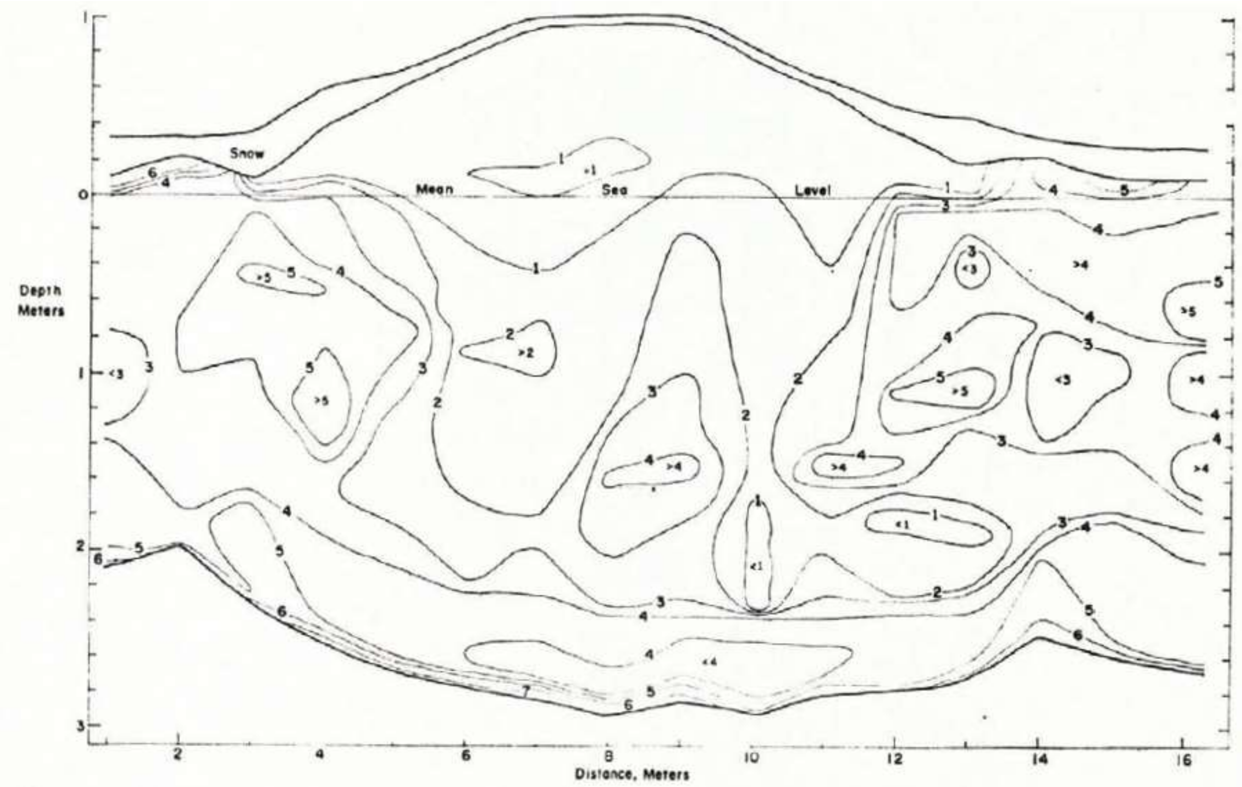

Figure 3.4 Cross-section of multi-year ice (MYI) illustrating the variation of salinity with topography. The iso-salinity lines are drawn at 1 ppt intervals. Courtesy of Cox & Weeks 1974 [44].

The specific density of MYI is slightly lower than FYI. In the upper layer of recrystallized ice has a density of 0.7 g/cm^3, whereas in the ice bulk it is typically between 0.800 and 0.900 g/cm^3 [34]. Because MYI is thicker and has a lower specific density than FYI, it floats higher out of the water than FYI. The bulk salinity of MYI above sea level is <1 ppt and 2-3 ppt below sea level in the bulk “clear” ice [34] [38]. This is illustrated in the Figure 3.4 taken from [44]. The fractional volume of air to the total volume of the MYI is typically 5-20% [29]. As discussed in Section 2.3, MYI is thicker and harder than FYI, and as such is hazardous to marine vessels.

As with FYI, the knowlege of the temperature profile, density and salinity of MYI during the summer melt period, as well as the structure and orientation of the inclusions will inform the decisions made in Sections 4.4 and 4.5 in the application of mixing theory to calculate a suitable effective permittivity to homogenize MYI.

3.3.3 Glacier Ice

Glacial ice is formed on land from compacted snow, rain and recrystallized melt waters. It is formed entirely of freshwater and therefore heterogenous mixture of pure ice with air inclusions. GI is slightly denser than MYI, with a specific density around 0.900 g/cm^3 and a fractional volume of air between 4-9% [13]. As such, GI is very hard and hazardous to marine vessels.

In the case of GI, the temperature profile, density and fraction volume of air will be applied to the appropriate mixing theory formula in Sections 4.4 and 4.5 to calculate a suitable effective permittivity to homogenize GI.

3.4 Permittivity

No discussion of electromagnetics is complete without a mention of Maxwell's equations. Maxwell's equations in differential form are:

$$\nabla \times \overline{\boldsymbol{H}}(\bar{r}) = \overline{\boldsymbol{J}}(\bar{r}) + j\omega\overline{\boldsymbol{D}}(\bar{r}) \tag{3.1}$$

$$\nabla \times \overline{\boldsymbol{E}}(\bar{r}) = -\overline{\boldsymbol{M}}(\bar{r}) - j\omega\overline{\boldsymbol{B}}(\bar{r}) \tag{3.2}$$

$$\nabla \cdot \overline{\boldsymbol{D}}(\bar{r}) = \rho_e(\bar{r}) \tag{3.3}$$

$$\nabla \cdot \overline{\boldsymbol{B}}(\bar{r}) = \rho_m(\bar{r}) \tag{3.4}$$

where

$\overline{\boldsymbol{E}}(\bar{r})$	is the electric field vector in V/m;
$\overline{\boldsymbol{H}}(\bar{r})$	is the magnetic field vector in A/m;
$\overline{\boldsymbol{D}}(\bar{r})$	is the electric flux density vector in As/m^2 or C/m^2 ;
$\overline{\boldsymbol{B}}(\bar{r})$	is the magnetic flux density vector in Vs/m^2;
$\overline{\boldsymbol{J}}(\bar{r})$	is the volume electric current density vector in A/m^2;
$\overline{\boldsymbol{M}}(\bar{r})$	is the volume magnetic current density vector in V/m^2;[10]
ω	is the angular frequency of the wave in Hz; and
$\rho_e(\bar{r})$	is the electric volume charge density scalar in As/ m^2; and
$\rho_m(\bar{r})$	is the magnetic volume charge density in Vs/ m^2.

In electromagnetics, three macroscropic material properties, which define the effects of a material on the electromagnetic fields, are of interest: the permittivity (ε), permeability (μ) and conductivity (σ). Permittivity relates the electric flux density, $\overline{\boldsymbol{D}}$, to the electric field intensity, $\overline{\boldsymbol{E}}$, in the material. Permeability relates the magnetic flux density, $\overline{\boldsymbol{B}}$, to the magnetic field intensity, $\overline{\boldsymbol{H}}$, in the material. And conductivity relates the conduction current density, $\overline{\boldsymbol{J}}$, to the electric field intensity, $\overline{\boldsymbol{E}}$, in the material.

---

[10] $\overline{\boldsymbol{M}}$ and ρ_m are not observable in practice. Their inclusion in Maxwell's equations enable the derivation (and subsequent use) of the surface equivalent theorem, which describes electromagnetic scattering in terms of fictitious equivalent electric and magnetic current densities. This is used in the derivation of the PMCHWT integral equation mentioned in Section 3.10.

These are referred to as the constitutive relationships and are written as:

$$\bar{\boldsymbol{D}}(\bar{r}) = \varepsilon\bar{\boldsymbol{E}}(\bar{r}) \tag{3.5}$$

$$\bar{\boldsymbol{B}}(\bar{r}) = \mu\bar{\boldsymbol{H}}(\bar{r}) \tag{3.6}$$

$$\bar{\boldsymbol{J}}(\bar{r}) = \sigma\bar{\boldsymbol{E}}(\bar{r}) \tag{3.7}$$

where

ε is the permittivity in F/m;

μ is the permeability in H/m;

σ is the conductivity in S/m;

Ice is a dielectric material, but has a non-zero conductivity and is not an insulator. Therefore, the permittivity and conductance are the electrical properties of interest here.

3.4.1 Electric Polarization

When a material is exposed to an electric field, the negatively charged electrons in the molecules of the material will try to separate from the positively charged nuclei of the molecules. The extent of this separation determines whether the material is a conductor (ie. the electrons become unbound and flow) or a dielectric (ie. the electrons are bound and displace). In a dielectric material, the degree of displacement between the positive and negative charges of the molecules, as shown in Figure 3.5, is referred to as the electric dipole moment or "electric polarization"[11].

The average electric polarization vector, $\bar{\boldsymbol{P}}(\bar{r})$, is given by the product of the free space permittivity, the susceptibility of the material to being polarized and the total electric field inside the material as result of the applied electric field from the external source(s) and the induced electric field from the internal (dipole) sources.

$$\bar{\boldsymbol{P}}(\bar{r}) = \varepsilon_o\chi_e\bar{\boldsymbol{E}}(\bar{r}) \tag{3.8}$$

where

χ_e is the electric susceptibility of the material;

ε_o is the free space permittivity in Farads, which is a constant value of:

$$\varepsilon_o = \frac{1}{c^2\mu_o} \approx 8.854 \times 10^{-12} \qquad [F]$$

---

[11] This is referring to the polarization of the molecule and should not be confused with the polarization of the electromagnetic wave. In this work, polarization will refer to the polarization of the electromagnetic field and, to avoid confusion, electrical polarization will be referred to as, the less succinct, electric dipole moment or electric dipole moment density.

μ_o is the free space permeability in Henries, which is a constant value of:

$$\mu_o = 4\pi \times 10^{-7} \qquad [H]$$

c is the speed of light in a vacuum, which is a constant value of:

$$c = 299\,792\,458 \qquad \left[\frac{m}{s}\right]$$

3.4.2 Relative Permittivity

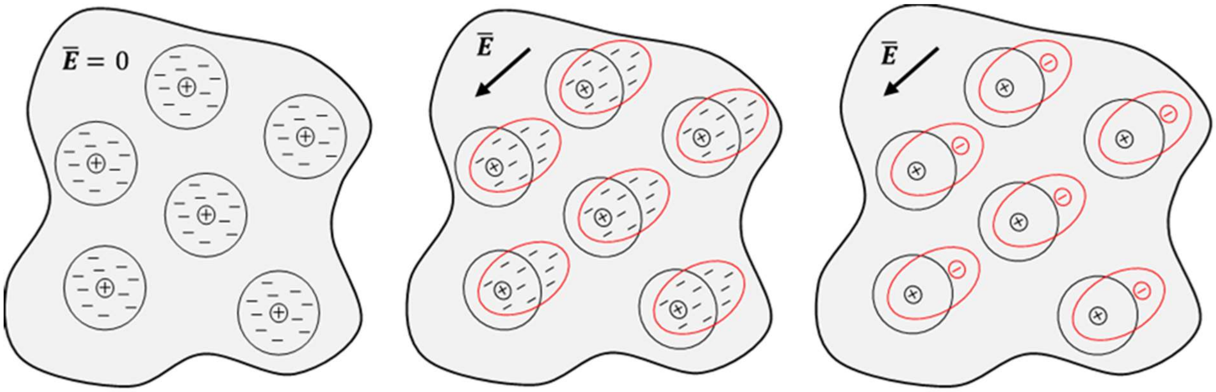

(a) (b) (c)

Figure 3.5 The effect of an applied (ie. incident) electric field on the molecules of a dielectric material. In the absence of an electric field (a), the molecules are "balanced" with the equal positive and negative charge densities around the nuclei. When an electric field is applied (b), the bound electrons are pulled or displaced in the opposite direction to the electric field vector. This creates a dipole moment (c), where the positive and negative electric charge densities are off centre, forming a dipole moment. Each molecule now has its own localized electric field which interacts with and perturbs the applied electric field.

By expanding equations (3.5) to include average electric polarization vector in equation (3.8), the constitutive relationship becomes:

$$\overline{\boldsymbol{D}}(\bar{r}) = \varepsilon_o \overline{\boldsymbol{E}}(\bar{r}) + \overline{\boldsymbol{P}}(\bar{r}) \tag{3.9}$$

$$\overline{\boldsymbol{D}}(\bar{r}) = \varepsilon_o \overline{\boldsymbol{E}}(\bar{r}) + \varepsilon_o \chi_e(\bar{r}) \overline{\boldsymbol{E}}(\bar{r}) \tag{3.10}$$

$$\overline{\boldsymbol{D}}(\bar{r}) = \varepsilon_o (1 + \chi_e(\bar{r})) \overline{\boldsymbol{E}}(\bar{r}) \tag{3.11}$$

The quantity $\big(1 + \chi_e(\bar{r})\big) = \varepsilon_r$ is referred to as the relative permittivity of the material. The relative permittivity was defined in the Clausius-Mossotti relation as the ratio of the permittivity of the material to the permittivity of free space, such that:

$$\varepsilon_r = \frac{\varepsilon}{\varepsilon_o} \tag{3.13}$$

and ε is the absolute permittivity, which is often referred to simple as the "permittivity", and $\bar{\boldsymbol{D}}(\bar{r}) = \varepsilon\bar{\boldsymbol{E}}(\bar{r})$

The above derivation and definitions assumed that the material is lossless. However, all natural earth materials are lossy and the permittivity then is a complex number where the dielectric constant[12], ε', describes the electric dipole moment effect of the material on the electric field, and the dielectric loss factor, ε", describes the attenuation or absorption of the electric field by the material, such that:

$$\varepsilon = \varepsilon' - j\varepsilon'' \tag{3.14}$$

3.4.3 Complex Permittivity

The term "complex permittivity" is often used. This has a different meaning than the statement above that permittivity of a lossy material is complex. Recalling Mawell's curl equation for the magnetic field relation, equation (3.1):

$$\nabla \times \bar{\boldsymbol{H}}(\bar{r}) = \bar{\boldsymbol{J}}(\bar{r}) + j\omega\bar{\boldsymbol{D}}(\bar{r}) \tag{3.1}$$

Substituting into this the current density given by the generalized Ohm's law (equation 3.7) gives:

$$\bar{\boldsymbol{J}}(\bar{r}) = \sigma\bar{\boldsymbol{E}}(\bar{r}) \tag{3.7}$$

and equation (3.5):

$$\bar{\boldsymbol{D}}(\bar{r}) = \varepsilon\bar{\boldsymbol{E}}(\bar{r}) \tag{3.5}$$

gives:

$$\nabla \times \bar{\boldsymbol{H}}(\bar{r}) = \sigma\bar{\boldsymbol{E}}(\bar{r}) + j\omega\varepsilon\bar{\boldsymbol{E}}(\bar{r})$$

$$\nabla \times \bar{\boldsymbol{H}}(\bar{r}) = j\omega\left\{\varepsilon - j\frac{\sigma}{\omega}\right\}\bar{\boldsymbol{E}}(\bar{r})$$

---

[12] Dielectric constant is a misnomer. In fact, the dielectric constant is rarely constant and affected by other external factors, such as frequency and, in the case of ice, temperature. The dielectric constant is always a real number and is often expressed relative to free space

Recognizing the material may be lossy, the terms in parenthesis expand to:

$$\left\{\varepsilon - j\frac{\sigma}{\omega}\right\} = \left\{\varepsilon' - j\varepsilon'' - j\frac{\sigma}{\omega\varepsilon_o}\right\}$$

$$\varepsilon_c = \varepsilon' - j\left\{\varepsilon'' + \frac{\sigma}{\omega}\right\} \tag{3.14}$$

where

ε_c is the complex permittivity and accounts for the dielectric loss of the material and the non-zero conductivity of the material; and

ε' is the dielectric constant, which is often expressed relative to free space and is equivalent to ε_r.

To define the loss component of the complex permittivity of a material, commercial vendors use the "loss tangent" of the material, which is defined as:

$$\tan\delta = \frac{Im\{\varepsilon_c\}}{Re\{\varepsilon_c\}} \tag{3.15}$$

such that:

$$\tan\delta = \frac{\varepsilon'' + \frac{\sigma}{\omega}}{\varepsilon'} = \frac{\varepsilon'' + \frac{\sigma}{\omega}}{\varepsilon_o\varepsilon_r} \tag{3.16}$$

Therefore, commercial vendors will usually characterize the dielectric material by the (relative) dielectric constant, ε_r, and the loss tangent, $\tan\delta$ [45].

3.4.4 Isotropic and Anisotropic Dielectric Materials

The discussion, up to this point, has been for isotropic dielectric materials. This is to say that the permittivity of the material is the same regardless of the orientation of the electric field. This allowed the permittivity, ε, to be written as a scalar quantity, with:

$$\overline{\boldsymbol{D}}(\bar{r}) = \varepsilon\overline{\boldsymbol{E}}(\bar{r})$$

showing that the electric flux density and electric field vectors are aligned.

If the material is anisotropic, the permittivity depends on the orientation of the electric field and incident angle of the electromagnetic wave. In this case, the permittivity is a dyadic (a 3x3 matrix) such that:

$$\bar{\bar{\boldsymbol{\varepsilon}}} = \begin{bmatrix} \varepsilon_{xx} & \varepsilon_{xy} & \varepsilon_{xz} \\ \varepsilon_{yx} & \varepsilon_{yy} & \varepsilon_{yz} \\ \varepsilon_{zx} & \varepsilon_{zy} & \varepsilon_{zz} \end{bmatrix}$$

Crystal structures contain symmetries and therefore an orientation can often be found that simplifies the dyadic, such that the permittivity can be written as a biaxial dyadic where:

$$\bar{\bar{\boldsymbol{\varepsilon}}} = \begin{bmatrix} \varepsilon_{xx} & 0 & 0 \\ 0 & \varepsilon_{yy} & 0 \\ 0 & 0 & \varepsilon_{zz} \end{bmatrix}$$

In this case, the material is said to have biaxial anisotropy.

Some crystal structures exhibit uniaxial anisotropy, such that the permittivity is the same for two of the dimensions and different in the third dimension. The permittivity is a uniaxial dyadic:

$$\bar{\bar{\boldsymbol{\varepsilon}}} = \begin{bmatrix} \varepsilon & 0 & 0 \\ 0 & \varepsilon & 0 \\ 0 & 0 & \varepsilon_{zz} \end{bmatrix}$$

It should be noted that with anisotropic materials, the electric flux density and the electric field are no longer aligned.

In Chapter 4, the ice types will be shown to be either isotropic (ie. MYI and Glacier Ice) or uniaxially isotropic (ie. FYI).

3.5 Dielectric Mixing Theory

In this section, the mixing theory developed and validated by Stogryn and Desargent [36], and improved by Sivhola and Kong [43] will be presented. Using the physical properties described in Section 3.3, the mixing theory presented below will be applied in Chapter 4 to determine an effective permittivity for the three marine ice types of interest, under the conditions of interest for this work.

The targets of interest in this thesis are electrically large (ie. much greater than a wavelength), heterogeneous materials containing thousands to millions of small inclusions. This would require an extremely fine mesh and a very large number of elements to mesh the entire volume, requiring massive amounts of computational resources. To reduce the computational burden, the target must be modelled as a homogeneous material. Sihvola [46] described homogenization of a material as "a process leading to its macroscopic characterization with fewer parameters than those needed for a full description of the original object". In the engineering models of marine ice presented in Chapter 4, the constituent property of interest to reduce the computational resources is the dielectric variation of the material.

The dielectric variation of the resulting homogeneous material is described by an effective permittivity. The effective (sometimes referred to as an apparent) permittivity is a theoretical permittivity for an equivalent homogeneous material which would produce the same scattered field as the desired heterogeneous material. Whereas the heterogeneous material would need to be modelled as a volumetric mesh, the homogeneous material can be modelled in terms of surface quantities (and hence a surface mesh), greatly reducing the computational resources[13].

Dielectric mixing formulas are algebraic formulas that calculate an effective permittivity of the mixture as a function of the constituent permittivities, their fractional volumes, and the shape of the inclusions. The mixing formulas use canonical shapes to approximate the inclusions in the material and simplify the analysis: most are based on spherical or elliptical inclusions. These shapes closely match the actual inclusions in ice. Modern dielectric mixing theory can be traced back to the turn of the century. Many dielectric mixing formulas for the calculation of an effective permittivity have been developed by the likes of Clausius and Mossotti (1850) [47], Lorenz and Lorentz (1880) [48], and Garnett (1904) [49]. The following sections will present a two phase and a three phase mixing formula: phase referring to the number of constituent materials involved.

3.5.1 Two Phase Dielectric Materials

One of the most common, due to it's simplicity and wide applicability [50], is the Maxwell Garnett[14] mixing formula given by:

$$\varepsilon_{eff} = \varepsilon_h + 3f\varepsilon_h \frac{\varepsilon_i - \varepsilon_h}{\varepsilon_i + 2\varepsilon_h - f(\varepsilon_i - \varepsilon_h)} \tag{3.17}$$

where

ε_h is the permittivity of the host medium;

ε_i is the permittivity of the inclusion medium; and

f is the volume faction of the inclusion medium with respect to the overall volume of the material[15].

A detailed derivation and analysis of the Maxwell Garnett formula is provided by Sihvola [46] [50], from which the equations that follow are taken. The Maxwell Garnett formula is valid for an isotropic host material with isotropic inclusions where the inclusion can be modelled as a sphere and the volume fraction of the inclusions is much less than the overall volume of the material (ie. f<<0.1).

The above equation assumes the inclusions are spherical and the resulting material is isotropic. This is not always the case. In fact, one of the materials of interest in this work, FYI, contains elliptical brine inclusions. Although, any shape may be calculated, general shapes require the use of numerical methods, whereas analytical solutions can be found for spherical and elliptical inclusions. In fact, it will be shown that a sphere is a simple form of an ellipse. An ellipse may

---

[13] As indicated in Section 3.7.

[14] Note that this is the Maxwell Garnett formula and not the Maxwell-Garnett formula because it is attributed to (James Clerk) Maxwell Garnett, known as Maxwell Garnett. Garnett's father was physicist William Garnett, who named him after his close friend, physicist James Clerk Maxwell [93]. It could simply be called the Garnett formula.

[15] In Section 4.5, it will be shown that the fractional volume can be calculated from the bulk salinity of ice.

also be used to describe a disc or a needle, making the mixing formulas, given below, applicable to a wide range of real world materials.

Elliptical inclusions are incorporated into the mixing formula using the depolarization factor of the ellipsoid [43] [46]. For an ellipsoid of semi-axes dimensions of a_x, a_y, and a_z, the depolarization factors are given by:

$$N_x = \frac{a_x a_y a_z}{2} \int_0^\infty \frac{ds}{(s + a_x^2)\sqrt{(s + a_x^2)(s + a_y^2)(s + a_z^2)}} \tag{3.18}$$

$$N_y = \frac{a_x a_y a_z}{2} \int_0^\infty \frac{ds}{(s + a_y^2)\sqrt{(s + a_x^2)(s + a_y^2)(s + a_z^2)}} \tag{3.19}$$

$$N_z = \frac{a_x a_y a_z}{2} \int_0^\infty \frac{ds}{(s + a_z^2)\sqrt{(s + a_x^2)(s + a_y^2)(s + a_z^2)}} \tag{3.20}$$

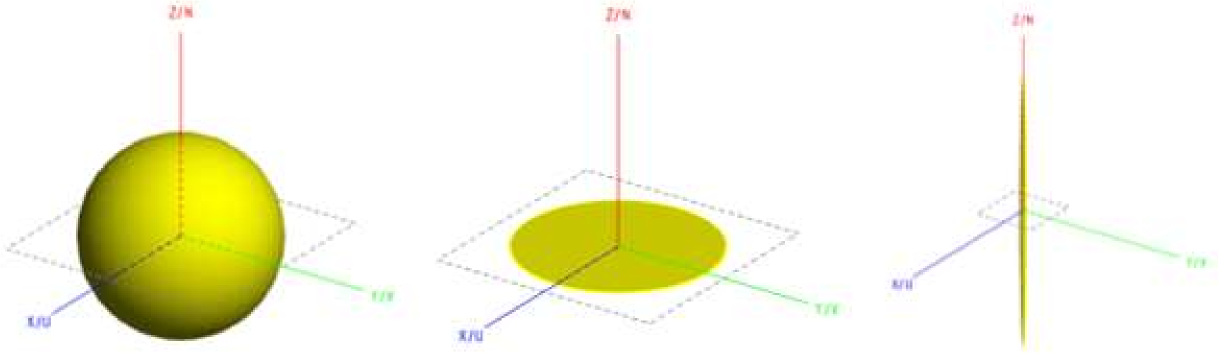

Figure 3.6 Diagram of the dimensions of a sphere, disc and needle for the calculation of the depolarization factors for the three special cases of an ellipsoid inclusion: a sphere, a disc and a needle.

The three depolarization factors for any ellipsoid must satisfy,

$$N_x + N_y + N_z = 1$$

For a sphere ($a_x = 1$, $a_y = 1$, $a_z = 1$), due to the symmetry, and so the depolarization factors must be:

$$(N_x, N_y, N_z) = \left(\frac{1}{3}, \frac{1}{3}, \frac{1}{3}\right)$$

For a disc ($a_x = 1$, $a_y = 1$, $a_z = 0$), the depolarization factors are:

$$\left(N_x, N_y, N_z\right) = (0, 0, 1)$$

For a needle, the depolarization factors are:

$$\left(N_x, N_y, N_z\right) = \left(\frac{1}{2}, \frac{1}{2}, 0\right)$$

If the axis of the elliptical inclusions are aligned, the effective permittivity is given by:

$$\varepsilon_{eff,x} = \varepsilon_h + 3f\varepsilon_h \frac{\varepsilon_i - \varepsilon_h}{\varepsilon_h + (1-f)N_x(\varepsilon_i - \varepsilon_h)} \tag{3.21}$$

$$\varepsilon_{eff,y} = \varepsilon_h + 3f\varepsilon_h \frac{\varepsilon_i - \varepsilon_h}{\varepsilon_h + (1-f)N_y(\varepsilon_i - \varepsilon_h)} \tag{3.22}$$

$$\varepsilon_{eff,z} = \varepsilon_h + 3f\varepsilon_h \frac{\varepsilon_i - \varepsilon_h}{\varepsilon_h + (1-f)N_z(\varepsilon_i - \varepsilon_h)} \tag{3.23}$$

If the elliptical inclusions are randomly oriented, the material becomes isotropic and the permittivity is a scalar given by:

$$\varepsilon_{eff} = \varepsilon_h + \varepsilon_h \frac{\frac{f}{3}\sum_{j=x,y,z} \frac{\varepsilon_i - \varepsilon_h}{\varepsilon_h + N_j(\varepsilon_i - \varepsilon_h)}}{1 - \frac{f}{3}\sum_{j=x,y,z} \frac{N_j(\varepsilon_i - \varepsilon_h)}{\varepsilon_h + N_j(\varepsilon_i - \varepsilon_h)}} \tag{3.24}$$

All of the equations above are based on the Maxwell Garnett mixing theory. Other commonly used mixing theories in electromagnetics and remote sensing are the Polder-van Santen formula [51] (also called the Bruggeman formula), and the Coherent Potential Approximation [50]. Sihvola [52] developed a "Generalized Mixing Formula" containing a dimensionless parameter (v) which reduces to Maxwell Garnett when $v = 0$, to Polder-van Santen when $v = 2$, and the Coherent Potential Approximation when $v = 3$. When the volume fraction is much less than one ($f \ll 1$), all three of these formulas produce the same numerical results. This is the case with sea ice and glacier ice, where the volume fraction of the inclusions is often expressed in tens of parts per thousand. Therefore, the Maxwell Garnett formula will be used in this work.

The equations above are for two phase dielectric materials and will be used to calculate the effective permittivity of Glacier Ice in the Chapter 4.

3.5.2 Three Phase Dielectric Materials

In the case of three phase dielectric materials, the equations presented above remain valid, but must be applied in sequence with the higher fractional volume inclusion included in the first pass, then using the result as the host medium and the lower fractional volume inclusion in the second pass. However, the Maxwell Garnett formula can be expanded to multi-phase materials in the form:

$$\varepsilon_{eff} = \varepsilon_h + 3\varepsilon_h \frac{\sum_{k=1}^{K} f_k \dfrac{\varepsilon_{i,k} - \varepsilon_h}{\varepsilon_{i,k} + 2\varepsilon_h}}{1 - \sum_{k=1}^{K} f_k \dfrac{\varepsilon_{i,k} - \varepsilon_h}{\varepsilon_{i,k} + 2\varepsilon_h}} \tag{3.25}$$

This formula assumes the inclusions are spherical and the material isotropic. Sivhola and Kong [43] have developed a multi-phase, multi-shaped inclusion formula for the calculation of anisotropic dielectric materials, but this equation will not be required in this work and so has not been included here.

In Chapter 4, equation 3.25 will be used to calculate the effective permittivity of FYI and MYI.

3.5.2 Application of Effective Permittivity

As stated earlier, the concept of homogenization of an inhomogeneous material, using mixing theory, is to determine an effective permittivity for which the electromagnetic scattering from the homogeneous object is the same as the scattering from the inhomogeneous object. There is a limitation on the frequency of the electromagnetic wave and the application of mixing theory. The effective permittivity is only valid up to a certain frequency, above which the scattering from the individual inclusions significantly influences the overall scattered field. A very conservative, general rule of thumb arises from the Rayleigh scattering based result that the characteristic length of the inclusion should be less than 1/10 of a wavelength:

$$L < \frac{\lambda}{10}$$

However, as Sihvola [50] pointed out, it is not easy to determine an exact upper frequency limit for the validity because the exact response of a randomly heterogeneous material is computational hard. This cut-off frequency is not only dependent on the relative size compared to the wavelength (the driving factor in the Rayleigh approximation above), but also on the shape, physical properties, and density of the inclusions, as well as the physical properties and loss (penetration depth) of the host material.

The penetration depth is important in our consideration of the applicability of the effective relative permittivities calculated using mixing theory for the three marine ice types, and so also in the building of the engineering models of the marine ice. Ulaby et al. 1982 [4] provide a derivation of the penetration depth, based on the Beer-Lambert Law, and show that:

$$\delta_p = \frac{1}{2\alpha} \tag{3.26}$$

where α is the attenuation constant given by:

$$\alpha = \frac{2\pi}{\lambda_o}\left|Im\sqrt{\varepsilon}\right| \tag{3.27}$$

3.6 Electrical Properties of Marine Ice Constituents

The electrical properties of marine ice have been well studied [34] [38] [53] [54]. The following section will discuss and summarize the effect of frequency, temperature, and, in the case of sea ice, brine salinity, on the permittivity of the constituent materials of marine ice. The constituent materials are pure ice, air and salt water brine. Pure ice will be treated as the host material. Air and brine will then be inclusion materials. The permittivity of seawater, separate from the brine, will also be presented here. All values are relative permittivity values.

3.6.1 Permittivity of Pure (Fresh Water) Ice

The real part of the permittivity of pure ice has been shown to be frequency independent and slightly temperature dependent between 2 – 200 GHz [55], such that the real part of the permittivity can be expressed as:

$$\varepsilon'_{ice} = 3.1884 + 0.00091T \tag{3.28}$$

where T is the temperature of the ice in Celcius (°C).

The imaginary part of the permittivity (dielectric loss factor) of pure ice is both frequency and temperature dependent, and can be expressed using the fitness equation:

$$\varepsilon''_{ice} = \left(\frac{A}{f}\right) + Bf^{C} \tag{3.29}$$

where coefficients A, B and C are temperature dependent and given in Figures 3.7 through 3.9. The curves in Figures 3.7 through 3.9 were extracted from data provided by [55] [54] [56]. For the engineering models presented in Chapter 4 and the pure ice sensitivity below, the values of A, B and C were selected as the median between the Debye and the Matzler & Wegmuller curves at 271 K (-2°C) in Figures 3.7 through 3.9.

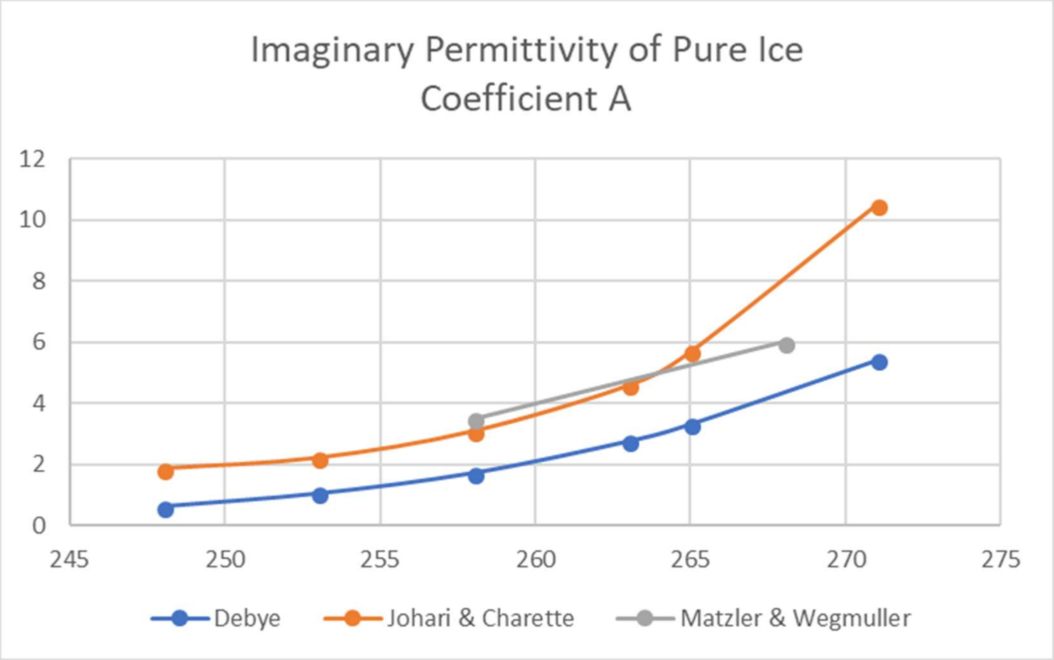

Figure 3.7 Plots of Coefficient A for the Imaginary Part of the Permittivity of Pure Ice. The curves were reproduced from the values presented in [54] for the Debye, Johari & Charette and Matzler & Wegmuller coefficient values.

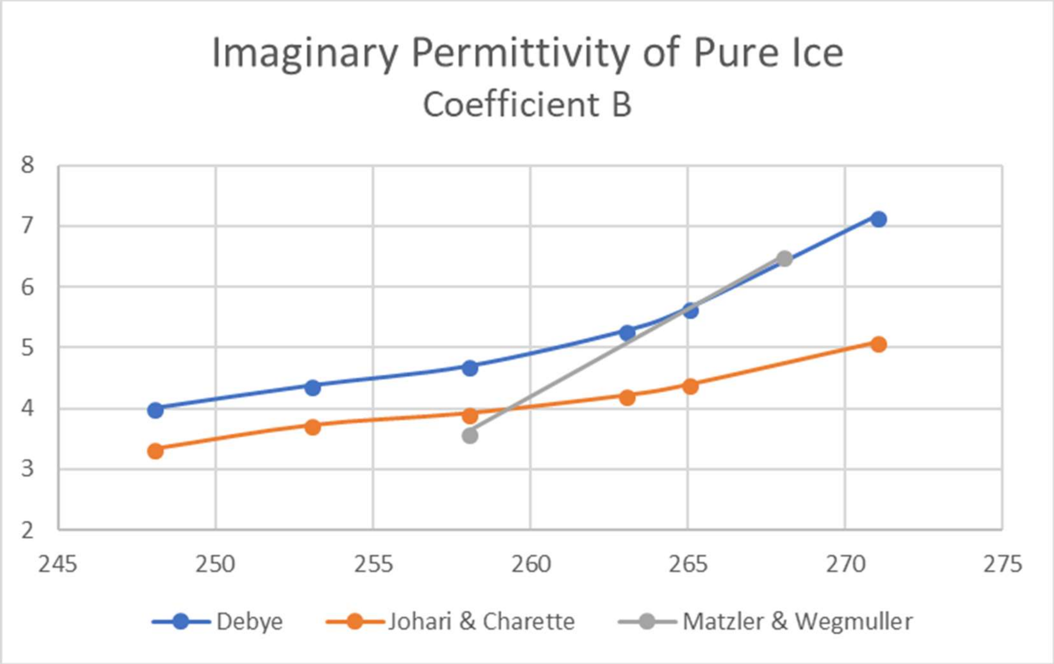

Figure 3.8 Plots of Coefficient B for the Imaginary Part of the Permittivity of Pure Ice. The curves were reproduced from the values presented in [54] for the Debye, Johari & Charette and Matzler & Wegmuller coefficient values.

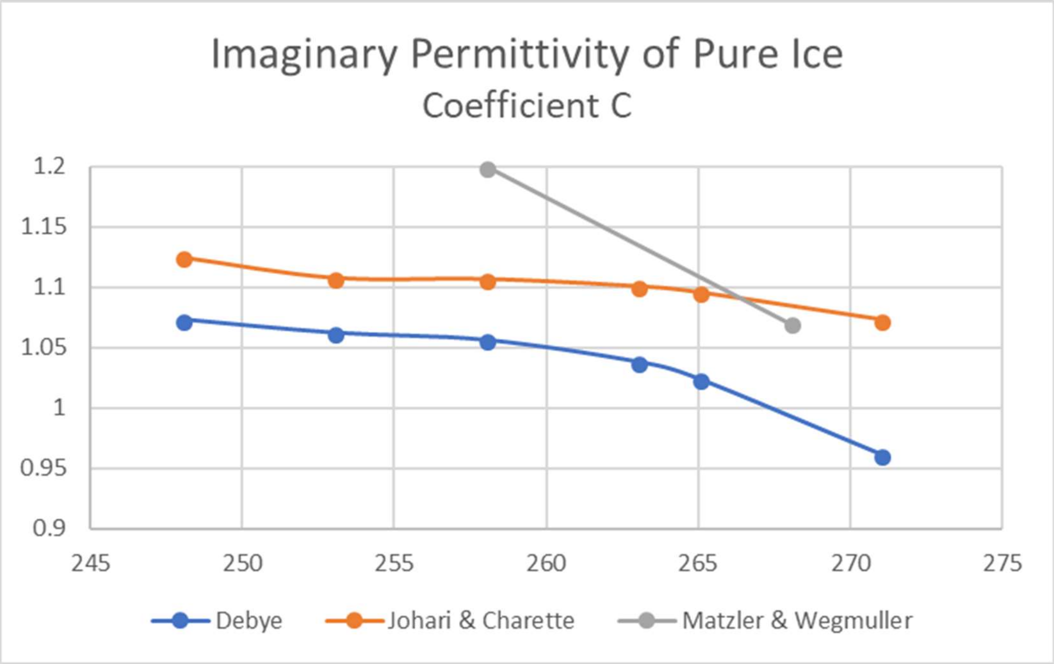

Figure 3.9 Plots of Coefficient C for the Imaginary Part of the Permittivity of Pure Ice. The curves were reproduced from the values presented in [54] for the Debye, Johari & Charette and Matzler & Wegmuller coefficient values.

Pure ice is the host medium in the heterogeneous mixture that constitutes marine ice and knowing the sensitivity of pure ice to temperature changes is important in understanding the sensitivity of marine ice to temperature change. Therefore, the sensitivity of pure ice between -5°C and -15°C was explored and is presented in Figure 3.10. The results show that the real part of the permittivity is essentially constant and the imaginary part of the permittivity changes minimally (±0.0005) over the frequency range of interest (6 to 10 GHz).

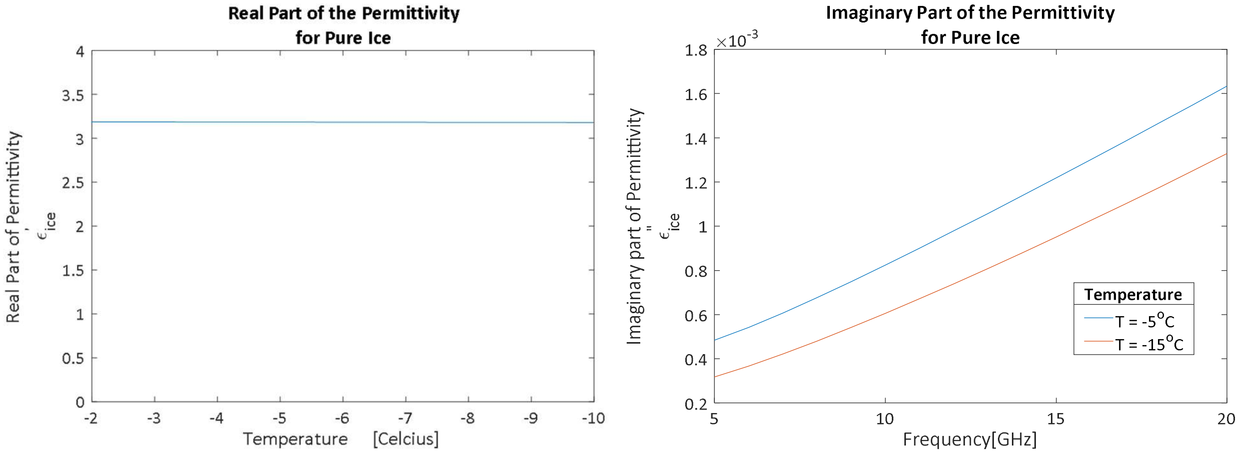

Figure 3.10 Plots of the real and imaginary parts of the permittivity of pure ice with respect to their temperature and frequency dependence. The plots were reproduced from [55] for the temperature and frequency range of interest for this thesis.

3.6.2 Permittivity of Air

The permittivity of air is normally assumed to be 1. However, the actual value is given by [57] as:

$$\varepsilon'_{air} = 1.0006$$

The loss factor of the permittivity of air is negligible.

3.6.3 Permittivity of Brine

The permittivity of seawater brine is much more complicated. The salinity of the brine increases as a function of temperature. As the temperature of the ice decreases, the temperature of the brine drops below the freezing point and the water in the brine freezes into pure ice crystals while rejecting the salt. The freezing of the water in the brine and salt rejection continues until the salinity of the brine reaches an equilibrium point with the freezing point of the brine. The salinity of the brine is a function of temperature. The permittivity of the brine is a function of the salinity and temperature of the brine, and the frequency of the incident electric field. The permittivity can be determined using the Debye relaxation formula [58], such that:

$$\varepsilon_{br} = \varepsilon'_{br} - j\varepsilon''_{br} = \varepsilon_{\infty br} + \frac{\varepsilon_{sbr} - \varepsilon_{\infty br}}{1 + j\omega\tau_b} - j\frac{\sigma_{DCbr}}{\omega\varepsilon_o} \tag{3.30}$$

where

ε'_{br} is the real part of the permittivity of the brine;

ε''_{br} is the imaginary part of the permittivity of the brine;

$\varepsilon_{\infty br}$ is the relative microwave dielectric constant of the brine:

ε_{sbr} is the relative static permittivity of brine, which is temperature and salinity dependent;

σ_{DCbr} is the dc conductivity of the brine;

τ_b is the relaxation time of the brine, which is temperature and salinity dependent; and

ω is the angular frequency of the electromagnetic wave.

The microwave permittivity of seawater as given by [37] was determined by King and Smith 1981 [59] to be:

$$\varepsilon_{\infty br} = 5.5$$

Reference [37] summarizing the works by [58] and [53] gives the static permittivity, ε_{sbr}, and relaxation time, τ_b, of the brine to be as follows:

$$\varepsilon_{sbr}(T,N) = \varepsilon_{sbr}(T,0)\begin{bmatrix} 1.000 - 0.2551N + 5.151 \times 10^{-2}N^2 \\ -6.889 \times 10^{-3}N^3 \end{bmatrix} \tag{3.31}$$

where

$$\varepsilon_{sbr}(T,0) = 88.22 - 0.4105T + 0.0008T^2 + 1.0879 \times 10^{-6}T^3 \tag{3.32}$$

with

$$\tau_b(T,N) = \tau_b(T,0)\begin{bmatrix} 0.1463 \times 10^{-2}NT + 1.000 - 0.04896N \\ -0.02967N^2 + 5.644 \times 10^{-3}N^3 \end{bmatrix} \tag{3.33}$$

and

$$\tau_b(T,0) = \begin{bmatrix} 17.80 \times 10^{-12} - 0.6032 \times 10^{-12}T \\ +0.0109 \times 10^{-12}T^2 - 0.0001 \times 10^{-12}T^3 \end{bmatrix} \tag{3.34}$$

The “normality” of the brine, N, is given by:

$$N = S_{br}\left[1.707 \times 10^{-2} + 1.205 \times 10^{-5}S_{br} + 4.058 \times 10^{-9}{S_{br}}^2\right] \tag{3.35}$$

where S_{br} is the salinity of the brine.

The salinity of the brine, S_{br}, between -22.9°C and -2°C is a function of the temperature of the surrounding ice and is given by [37] as:

$$S_{br} = -3.99 - 22.700T - 1.0015T^2 - 0.019956T^3 \tag{3.36}$$

This was determined from a best-fit evaluation of experimental data.

The conductivity of the brine is given by:

$$\sigma_{DCbr}(T,N) = \sigma_{DCbr}(25,N)\begin{bmatrix} 1.000 - 1.962 \times 10^{-2}\Delta + 8.08 \times 10^{-5}\Delta^2 \\ -\Delta N\begin{Bmatrix} 3.02 \times 10^{-5} + 3.922 \times 10^{-5}\Delta \\ +N(1.721 \times 10^{-5} - 6.584 \times 10^{-6}\Delta) \end{Bmatrix} \end{bmatrix} \tag{3.37}$$

where

$$\Delta = 25 - T \qquad (T = temperature\ in\ {}^\circ C) \tag{3.38}$$

and

$$\sigma_{DCbr}(25,N) = N\begin{bmatrix} 10.394 - 2.3776N + 0.68258N^2 \\ -0.13538N^3 + 1.0086 \times 10^{-2}N^4 \end{bmatrix} \tag{3.39}$$

3.6.4 Permittivity of Seawater

The model for seawater used in this work was defined by Meissner & Wentz [60], and is valid for temperatures between -2°C and +29°C, salinity between 0 and 40 parts per thousand, and frequencies up to 90 GHz. This model uses measurement data from satellite remote sensing to determine curve-fitting equations for the parameters of the Debye double relaxation frequency model:

$$\varepsilon(T,S) = \varepsilon_\infty(T,S) + \frac{\varepsilon_s(T,S) - \varepsilon_1(T,S)}{1 + jv/v_1(T,S)} + \frac{\varepsilon_1(T,S) - \varepsilon_\infty(T,S)}{1 + \dfrac{jv}{v_2(T,S)}} - j\frac{\sigma(T,S)}{2\pi v \varepsilon_o} \tag{3.40}$$

where

$\varepsilon_\infty(T,S)$ is the relative microwave dielectric constant of seawater:

$\varepsilon_s(T,S)$ is the relative static permittivity of seawater;

σ is the DC conductivity of the seawater;

τ_b is the relaxation time of the seawater;

$v_1(T,S)$ is the first Debye relaxation frequency;

$v_2(T,S)$ is the second Debye relaxation frequency; and

v is the angular frequency of the electromagnetic wave in free space.

T is the temperature in degrees Celcius, S is the salinity in parts per thousand (ppt).

The conductivity of seawater used by [60] stems from the regression fits developed by [61] and is repeated here for ease of reference:

$$\sigma(T,S) = \sigma(T,S=35)R_{15}(S)\frac{R_T(S)}{R_{15}(S)} \tag{3.40}$$

where

$$\sigma(T,S=35) = \begin{bmatrix} 2.903602 + 8.607\times10^{-2}T + 4.738817\times10^{-4}T^2 \\ -2.991\times10^{-6}T^3 + 4.3047\times10^{-9}T^4 \end{bmatrix} \tag{3.41}$$

$$R_{15}(S) = S\frac{(37.5109 + 5.45216S + 1.4409\times10^{-2}S^2)}{(1004.75 + 182.283S + S^2)} \tag{3.42}$$

$$\frac{R_T(S)}{R_{15}(S)} = 1 + \frac{\alpha_0(T-15)}{(\alpha_1 + T)} \tag{3.43}$$

and

$$\alpha_0 = \frac{(6.9431 + 3.2841\,S - 9.9486 \times 10^{-2} S^2)}{(84.850 + 69.024\,S + S^2)} \tag{3.44}$$

$$\alpha_1 = 6.9431 + 3.2841\,S - 9.9486 \times 10^{-2} S^2 \tag{3.45}$$

The Debye parameters for the permittivity of seawater developed by [60] are represented by the following polynomial curve-fit equations and the fit parameters in Tables 3.1:

$$\varepsilon_s(T,S) = \varepsilon_s(T,S=0)e^{b_0 S + b_1 S^2 + b_2 ST} \tag{3.46}$$

$$v_1(T,S) = v_1(T,S=0)[1 + S(b_3 + b_4 T + b_5 T^2)] \tag{3.47}$$

$$\varepsilon_1(T,S) = \varepsilon_1(T,S=0)e^{b_6 S + b_7 S^2 + b_8 ST} \tag{3.48}$$

$$v_2(T,S) = v_2(T,S=0)[1 + S(b_9 + b_{10} T)] \tag{3.49}$$

$$\varepsilon_\infty(T,S) = \varepsilon_\infty(T,S=0)[1 + S(b_{11} + b_{12} T)] \tag{3.50}$$

where

$$\varepsilon_s(T,S=0) = \frac{3.70886 \times 10^4 - 82.168T}{4.21854 \times 10^2 + T} \tag{3.51}$$

$$\varepsilon_1(T,S=0) = a_0 + a_1 T + a_2 T^2 \tag{3.52}$$

$$v_1(T,S=0) = \frac{45 - T}{a_3 + a_4 T + a_5 T^2} \tag{3.53}$$

$$\varepsilon_\infty(T,S=0) = a_6 + a_7 T \tag{3.54}$$

$$v_2(T,S=0) = \frac{45 - T}{a_8 + a_9 T + a_{10} T^2} \tag{3.55}$$

Table 3.1 Values for fit parameters a_i and b_i for the calculation of the Permittivity of Seawater.

i	a_i
0	5.7230
1	0.022379
2	-0.00071237
3	5.0478
4	-0.070315
5	0.00060059
6	3.6143
7	0.028841
8	0.13652
9	0.0014825
10	0.00024199

i	b_i
0	-3.56417E-03
1	4.74868E-06
2	1.15574E-05
3	2.39357E-03
4	-3.13530E-05
5	2.52477E-07
6	-6.28908E-03
7	1.76032E-04
8	-9.22144E-05
9	-1.99723E-02
10	1.81176E-04
11	-2.04265E-03
12	1.57883E-04

All coefficients in Table 3.1 were used in the calculation of equations 3.46 through 3.54. It is possible to assess the sensitivity of the Debye parameters and reduce the coefficients in the equations. However, this would require significant analysis and result in a negligible reduction in computational resources.

3.7 Method of Moments Integral Equation Solutions

The scattered field from ice objects (treated as lossy homogenous dielectrics) will be computed using a full-wave analysis, as implemented in the commercial computational electromagnetics (CEM) software FEKO by Altair [48]. It uses the method of moments to obtain numerical solutions to the so-called PMCHWT combined field integral equation formulation. This integral equation has, through use of the surface equivalence principle used in its derivation, equivalent electric ($\bar{J}_s$) and magnetic ($\bar{M}_s$) current densities on the surface of the ice object as its unknowns. The presence of the sea surface is accounted for though use of a modified Green's function (eg. PEC half-space Green's function; approximate material half-space Green's function that has the half-space effects accounted for approximately using Fresnel reflection coefficients; exact Green's function with the presence of the material half-space effects accounted for rigorously using Sommerfeld theory) in the integral equation, and hence in all steps related to its numerical solution by the method of moments. The PMCHWT is free from so-called internal resonance problems [49] and so its solution is valid at all frequencies. The PMCHWT is a surface integral equation formulation and not a volume integral equation formulation. However, being a full-wave method, it accounts for all scattering effects, interpreted as surface or volume scattering phenomena (see Section 3.9) from the object, provided the correct effective permittivity (see Section 3.5) is used as the permittivity of the object.

In integral equation formulations, the total field is considered to consist of an incident field and a scattered field. The incident field is that which exists with the scattering object present. Thus, in the present case, the incident field is that extant with the ice object absent, but with the material half-space present. We will for the most part specify the incoming wave to be a plane wave. It should be remembered, however, that this on its own will not be the "incident field" used by the integral-equation/method-of-moments computation. The incident field will be the incoming plane wave plus the field reflected by the half-space, and will be determined using the modified Green's function mentioned above (with the ice object absent). Thus the incident field "seen" by the CEM computation will include what we have referred to in Section 3.8 as the influence of propagation effects on incoming wave. Once the complete CEM computation has been executed, and the unknown current densities on the ice object are known, these current densities are used (along with the modified Green's function) to find the scattered field; thus the scattered field we observe from the ice object also incorporates the propagation effects.

The manner in which this scattered field is used to measure and compare the backscattered field properties of the ice objects in Chapters 4 and 5 will be described next in Section 3.8.

3.8 Backscatter Intensity, Backscatter Signature, Radar Cross-Section and Apparent Radar Cross-Section

Up to this point, the term radar cross-section (RCS) has intentionally been avoided and the term backscatter signature has been used in its place. This has been done to make a distinction between the quantity that is being measured when discussing ships, or in this case ice targets, on a sea surface, and the quantity being measured when discussing air targets in free space. The sea surface has a significant effect on the incident and scattered fields for a surface target, which will be discussed in this section, and cannot be ignored.

3.8.1 Backscatter Intensity & Backscatter Signature

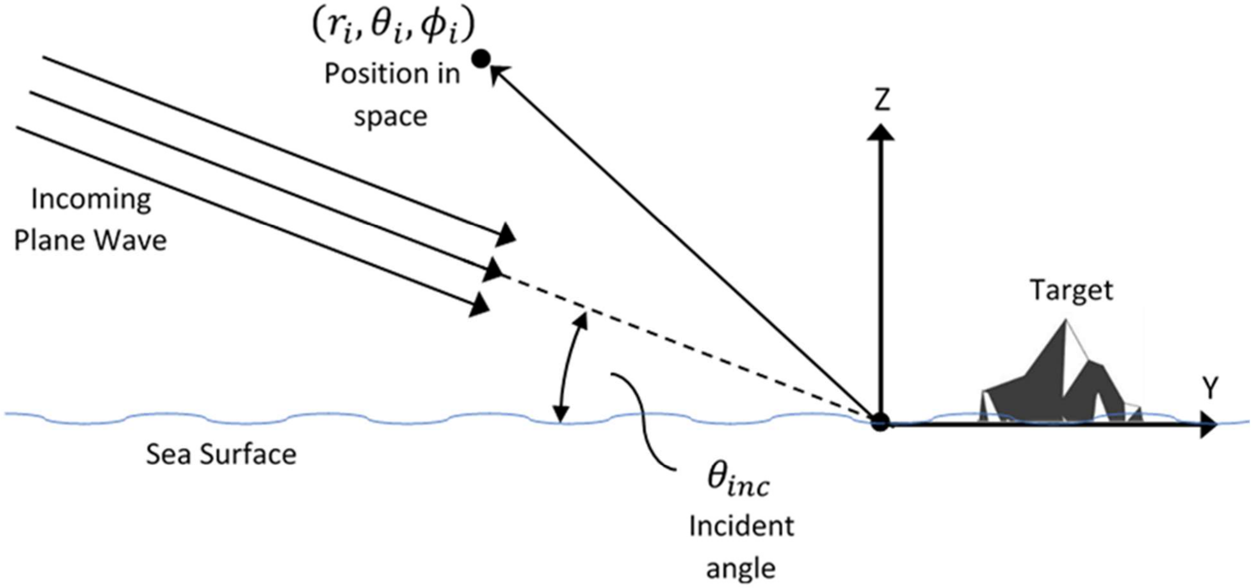

Figure 3.11 Diagram of the backscatter scenario for a dielectric object (iceberg) on dielectric halfspace (seawater surface). Iceberg graphic courtesy of [95].

After the ice object has been illuminated by a unit-amplitude plane wave that is incoming from direction, $\hat{r}_{inc} = (\theta_{inc}, \phi_{inc})$, it scatters electromagnetic waves in all directions. At points distant from (in the far zone of) the ice object, the scattered electric field can be written as

$$\bar{E}_{scat}(r_i,\theta_i,\phi_i) = \bar{F}_{scat}(\theta_i,\phi_i)\frac{e^{-jk}}{r}$$

with units of V/m. The quantity, $|\bar{E}_{scat}(r_i,\theta_i,\phi_i)|$, is called the electric field intensity at the point in space, (r_i,θ_i,ϕ_i). The distance from the target to the observation point is not necessarily the distance, or range, from the radar to the target. If the origin of the coordinate system is in the vicinity of the target, and the observation point is in the far-zone of the target, then the range would be an acceptable interpretation. The quantity, $\bar{F}_{scat}(\theta_i,\phi_i)$, provides the angular distribution of the scattered electric field. Its actual numerical values (as opposed to how its values change with observation angles, or with the incoming incident angle of the plane wave) are of no importance: only its relative value in observation angle compared to another is of interest. In this work, the quantity, $|\bar{F}_{scat}(\theta_i, \phi_i)|$, measured in the direction directly opposite to that of the incoming plane wave will be referred to as the "backscatter intensity". The backscatter intensity will normally be presented in dBV, such that:

$$|\bar{F}_{scat}(\theta_i, \phi_i)|_{dB} = 20\, log|\bar{F}_{scat}(\theta_i, \phi_i)|$$

The normalized backscatter intensity defined as:

$$|\bar{F}_{scat}(\theta_i, \phi_i)|_{norm} = \frac{|\bar{F}_{scat}(\theta_i, \phi_i)|}{|\bar{F}_{scat}(\theta_{max}, \phi_{max})|}$$

where $|\bar{F}_{scat}(\theta_{max}, \phi_{max})|$, is the magnitude of $\bar{F}_{scat}(\theta_i, \phi_i)$ in the direction of $(\theta_{max}, \phi_{max})$, in which the backscatter intensity is a maximum.

The term backscatter signature will be used in this work to refer to the co- and cross polarized backscatter intensity and depolarization response of a surface target or the co- and cross polarized apparent radar cross-section[16].

3.8.2 Radar Cross-Section

The IEEE [62] definition of radar cross section is a measure of the reflective strength of a target. This is often referred to as the mono-static radar cross-section (RCS), the differential backscattering coefficient, or simply the backscattering coefficient. The radar cross-section, σ_t, is defined as the ratio of the incident field power density and the scattered field power density as the range, R, approaches infinity. It is usually written as [63] [64]:

$$\sigma_t = \lim_{R\to\infty} 4\pi R^2 \frac{|\bar{E}_{scat}|^2}{|\bar{E}_{inc}|^2} \qquad [m^2]$$

where $|\bar{E}_{scat}|$ is the electric field magnitude at the receiver location and $|\bar{E}_{inc}|$ is the incident field magnitude at the target location. The quantity, R, is the distance between the observation point and the target. This definition only makes sense when the target is in free space[17] and, as indicated, the distance $R \to \infty$. In such cases, the fields $\bar{E}_{inc}$ and $\bar{E}_{scat}$ are locally plane wave fields at their respective observation points, and the power densities are then easily related to $|\bar{E}_{inc}|^2$ and $|\bar{E}_{scat}|^2$ through the intrinsic impedance of free space, η_0. The unit of measure of σ_t is square metres. It is often conceptualized as the cross-sectional area of an isotropic scatterer that reflects the same amount of power in the direction of the radar as the actual target. Knott et al. [64] point out that this definition characterizes the target and removes the effects of the

---

[16] The apparent radar cross-section will be defined in Section 3.8.3 and will be used in this work to when discussing surface targets.

[17] For this reason, the term radar cross-section will not be used by this author when referring to surface targets.

transmitter power, receiver sensitivity, and position of the transmitter or receiver distance. Using the above definition, countless textbooks [63] [65] derive the well-known radar equation:

$$P_{rx} = \frac{P_{tx} G^2 \lambda^2}{(4\pi)^3 R^4} \sigma_t$$

where

P_{rx} is the power received by the radar receiver in Watts [W];

P_{tx} is the transmitted power of the receiver in Watts [W];

G is the gain of the antenna [unitless];

λ is the wavelength of the operating frequency in metres [m];

σ_t is the radar cross-section of the target in square metres [m^2]; and

R is the distance (or range) from the radar to the target in metres [m].

3.8.3 Apparent Radar Cross-Section

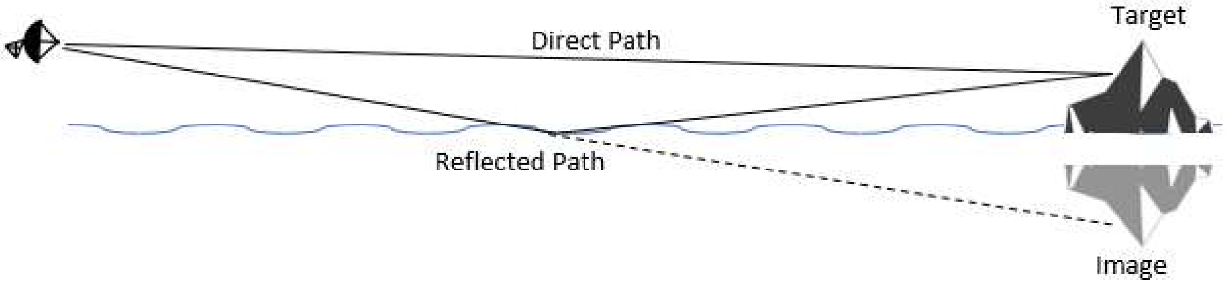

Figure 3.12 Low angle grazing over a sea surface showing the direct and surface reflected paths of the incident and scattered electromagnetic waves, and the target's image below the surface. Iceberg graphic courtesy of [95].

Next, consider the case of a target located on or near a ground plane such as a sea surface, ice floe or land. It is widely known [63] [64] [66] that the surface significantly affects the power density of the incident and scattered fields. In the case of surface targets, the low grazing angle means that the radar beam will illuminate the ground, creating multi-path illumination of the target with two distinct incident wave paths and two distinct scattered wave paths: a direct path and a reflected path. This is illustrated in Figure 3.12. The incident field at the target will be a result of the two incident unit amplitude waves and dependent on the relative amplitudes and phases of the wave incident from the direct and reflected paths. The same holds for the scattered field apparent at the radar receiver, which will be the result of the scattered wave from the direct and reflected paths. The actual effect of the sea is difficult to calculate analytically, since it is often rough and, in the case of observation of the natural environment, comprised of a complex dielectric material (ie. seawater, rock or soil). Thus, the return will consist of contributions from the target itself and clutter due to the sea surface roughness.

In such situations, the "apparent radar cross-section" (ARCS) is then defined as[18]:

$$\sigma_{app} = (\sigma_t \cup \sigma_c)V^4$$

where V^4 is a propagation factor[19] that cannot, in general, be found analytically. The symbol $(\sigma_t \cup \sigma_c)$ is meant to indicate that the RCS is a combination of the RCS from the actual target and the clutter from the ground plane in the radar resolution cell, which will not be a simple addition[20].

If it is assumed that the sea is perfectly flat (that is, not rough) then there is no clutter return, and we can write the ARCS as[21]:

$$\sigma_{app} = \sigma_t V^4$$

The received power at the radar is then:

$$P_{rx} = \frac{P_{tx}G^2\lambda^2}{(4\pi)^3R^4}\sigma_{app}$$

If it is further assumed that the sea surface is a perfectly flat perfect conductor (so that the plane wave reflection coefficient magnitude is equal to 1), and the grazing angle is small, Skolnik [63] shows that the propagation can be analytically expressed as:

$$V^4 = 16\,sin^4\left(\frac{2\pi h_a h_t}{\lambda R}\right)$$

where

h_a is the height of the radar antenna in metres [m];

h_t is the height of the target in metres [m];

λ is the wavelength of the operating frequency in metres [m]; and

R is the direct path distance from the radar to the target in metres [m].

Given that sin^4 is a value between 0 and 1, the propagation factor must be a value between 0 and 16. If the surface is rough or comprised of a complex dielectric material (whose reflection coefficient magnitude is less than 1), a more complicated expression to calculate an approximation of V^4 exists [66] [67] which results in a maximum value less than 16. These closed-form solutions are approximations of the affects of multi-path propagation over a smooth or rough surface. An

---

[18] It is noted that there is a lack of immediate clarity, in many papers and texts, on the definition and meaning of non-free-space radar cross section. The treatment given here is the result of some effort on the part of the author to explain and define these concepts in a way that makes it consistent with the various treatments found in all such references encountered. Some of the symbols used here are by necessity not the same as those used in the above references.

[19] The propagation factor is denoted V^4 in keeping with the common nomenclature used by Barton [65], Skolnik [63] and Shtager [66].

[20] This definition is based on J.Claverie and Y.Hurtaud, "Variation of the apparent RCS of maritime targets due to ducting effects", European Conf. Antennas & Propagation, Davos, Switzerland, April 2000.

[21] Note that we are not implying that the propagation factor remains the same.

exact solution of the scattering from a surface target on a rough dielectric halfspace can only be found numerically using CEMs.

In other words, the ARCS is not a property of the target alone, but of the properties of the surface and the location of the radar (the sensor) with respect to the surface and the target. However, this does not mean that the radar and the target will not be in each other's far zone.

3.8.4 Normalized Radar Cross-Section

If clutter is to be included then we need to know not only the height of the radar antenna, but also the beamwidth and the pulse width of the radar. This allows us to determine an areal field of view, A_{FOV}, that consists of the portion of the surface seen by the radar in which the target lies, given by:

$$A_{FOV} = \frac{c\tau_0 R\beta_h}{2}$$

where

c is the speed of light in metres/second [m/s];

τ_0 is the pulse width in seconds [s];

R is the range from the radar to the target in metres [m]; and

β_h is the horizontal beamwidth in radians.

The term normalized radar cross-section (NRCS) is often used in the case of surface targets. It has also been called the (back)scattering coefficient, differential scattering cross-section and, more accurately, the clutter cross-section per unit area. It is a measure of the clutter return that is independent of the illuminated area, such that:

$$\sigma^0 = \frac{\sigma_c}{A_{FOV}}$$

The received power at the radar is then:

$$P_{rx} = \frac{P_{tx}G^2\lambda^2}{(4\pi)^3R^4}V^4A_{FOV}\sigma^0$$

This is equation (8-9) from Haykin et al. [13, p. 348].

The apparent radar cross-section, σ_{app}, can therefore be connected to the so-called normalized radar cross-section, σ^0, as:

$$\sigma^0 = \frac{\sigma_{app}}{A_{FOV}V^4}$$

3.9 Scattering Phenomena

In a radar system, the quantity being measured is the backscattered electric field power density at the antenna: the scattered field from the target due to the incident field transmitted from the radar. From this measurement, the backscatter coefficient or apparent radar cross-section can be calculated as discussed in Section 3.8. The scattered fields computed using computational electromagnetics provide complete results including all the scattering phenomena present in the target, as well as all the propagation effects. Because marine ice is an irregularly shaped, heterogeneous mixture of materials with different permittivities, there are many scattering phenomena in terms of which the overall results can be interpreted. The incoming wave is not simply reflected and refracted. A portion of the incident field is scattered by the air-surface boundary, and a portion of the incident field passes into the volume of the dielectric material where it is dissipated, refracted and scattered by the internal inhomogeneities (which will be treated as an equivalent homogeneous material in the engineering models). The extent of such surface- versus volume-scattering phenomena present depends on the frequency, the polarization and incident angle of the incident wave, as well as the density of the inhomogeneities and their physical properties, and the penetration depth (attenuation) of the dielectric material, to name a few. The resulting scattered field is a complicated superposition of both surface- and volume-scattering phenomena taking place to varying degrees. Figure 3.13 provides an illustration of surface- versus volume-scattering effects.

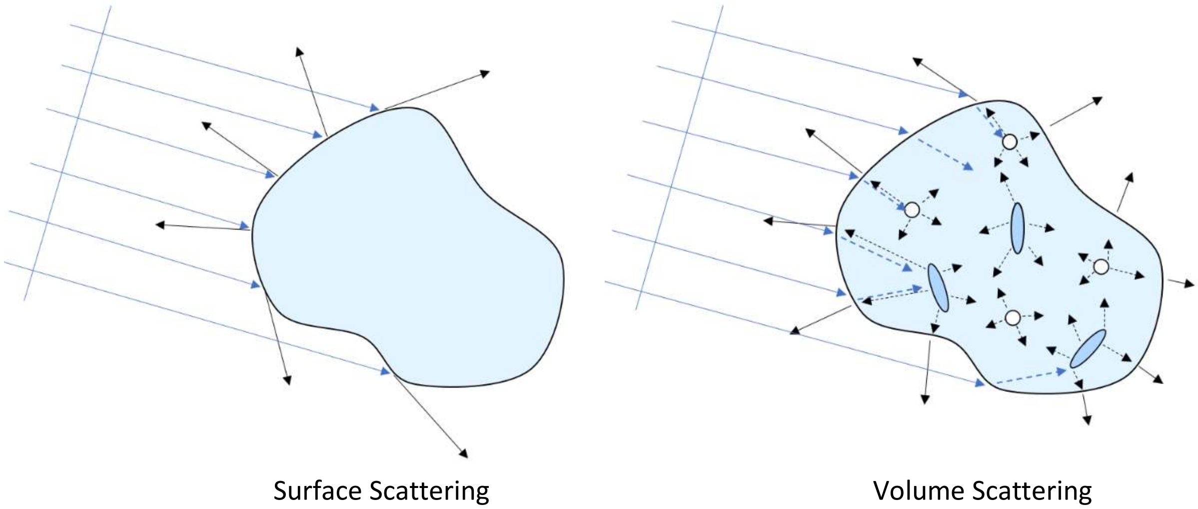

Figure 3.13 Illustration of surface- versus volume-scattering phenomena. The resulting scattered field would be a combination of surface and volume scattering.

3.10 Polarization

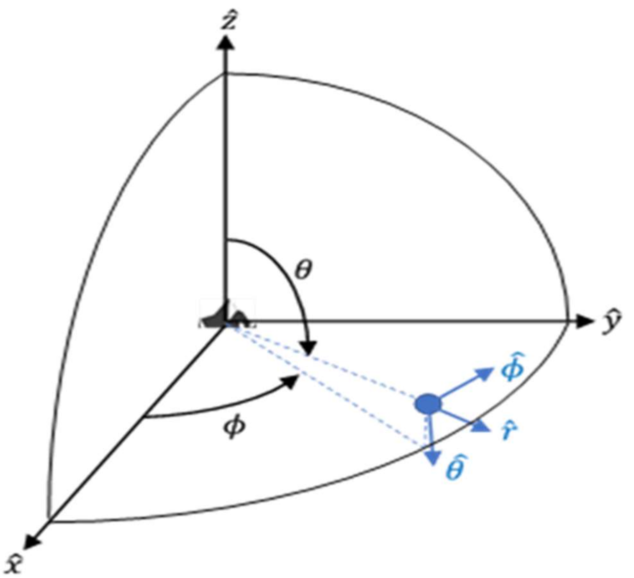

Figure 3.14 Cartesian coordinate system showing the orientation of the phi and theta vectors used as co- and cross-polarization respectively.

Polarization describes the orientation of the electric field vector of the radar wave in space, with horizontal polarization referring to an electric field vector that is parallel to the horizontal plane (earth's surface) and vertical polarization referring to an electric field vector that is perpendicular to the horizontal plane. In this work, the transmitted wave will always be horizontally polarized, as this is the convention for all surface-based, marine navigation and search radars. This was chosen for its superior performance in target detection in the presence of sea clutter [63].

When a radar transmits one polarization and receives two polarizations, the received signals are referred to as like-polarized or co-polarized, denoted by HH or VV, and as cross-polarized, denoted by HV or VH. The first letter indicates the orientation of the electric field of the transmitted wave [13]. The ratio of the cross-polarization over the co-polarization of the scattered field is often called depolarization:

$$\left.\frac{\bar{E}_{scat}^{cross}(\theta_i, \phi_i)}{\bar{E}_{scat}^{co}(\theta_i, \phi_i)}\right|_{linear}$$

or

$$\bar{E}_{scat}^{cross}(\theta_i, \phi_i)|_{dB} - \bar{E}_{scat}^{co}(\theta_i, \phi_i)|_{dB}$$

The results for radar signature presented in Chapter 5 will be discussed in terms of co- and cross-polarized backscatter intensity. In FEKO [68], the computational electromagnetic software used in this study, the phi and theta vectors of the backscatter intensity will be used for co- and cross-polarization respectively, as shown in Figure 3.14.

The link and relative importance between surface and volume scattering, and the degree of depolarization of the backscattered field is an area of debate within the ice signature modelling community [69].

3.11 Surface-Base Remote Sensing of Marine Ice

Satellite-based research into the microwave signature of marine ice has shown that marine ice can be reliably classified using frequency and polarization diversity [70] [71]. However, due to the anisotropic nature of marine ice and the difference between the incident angle for satellite-remote sensing (0-70° incident angle) and surface-based remote sensing (1° grazing angle = 89° incident angle), the radar signature for the same marine ice target will be different for satellite and surface-based remote sensing by radar. Although significant research has been conducted in the area of satellite-based remote sensing of marine ice, much of the data cannot be used for surface-based remote sensing because the data sets do not include high incident angles (ie. >60°). However, although the conclusions from satellite-based studies may not be directly relevant for the surface-based radar, the techniques such as the use of frequency comparison and polarization of the return signal, for target classification are relevant.

Complicating the validation of this work is the fact that much less research has been conducted in the area of surface-based remote sensing of marine ice. This research was conducted in the late 1980s and early 1990s, and was primarily focused on improving ice detection and tracking capabilities through:

a. Increasing the sampling rate by increasing the Pulse Repetition Frequency (PRF) or scan rate;
b. Increasing the dwell time and thus improving the signal to noise ratio;
c. Increasing the transmit power and gain of the radar;
d. Decreasing beam width which decrease angular tracking noise;
e. Using multiple polarizations;
f. Using longer wavelength radar bands than X-band, typically S-band; and
g. Using advanced signal processing [72].

However, data on the radar signature and depolarization from the three marine ice types of interest were collected and presented in the work by Haykin et al. in [13]. This data is summarized in the following sub-section and will be used to validate the results in Chapter 5.

3.11.1 Current Ice Navigation Radar Capabilities

The first experimental dual-polarized marine navigation radar appears to have been developed in 1984 by McMaster University and funded by the Canadian Coast Guard through the National Research Council of Canada. The radar was called the IPIX radar: ***I***ntelligent ***Pix***el-processing radar. This radar underwent a major revision in 1991-1992 [13]. The results of this research have been published in [13] [15] [73] [74], but portions of this research will be presented here for use in the validation of the engineering models presented in Chapter 4.

From 1992 to the present, there is a gap in the research into surface-based remote sensing of marine ice. With the exception of two papers from the Canadian Coast Guard, a scoping study done in 2005 into the requirements for an ice navigation radar and a report in 2016 in which the Canadian

Coast Guard is encouraging the development of a dual-polarization radar for ice classification [6], there does not appear to be any publicly available research in this area.

A report in 2015 by the National Petroleum Council [72] on Arctic marine navigation capabilities indicated that there were currently only two marine navigation radar systems in development or operation using dual-polarization: the Selesmar Selux in Sweden and the Rutter Sigma 6 in Canada. The Selesmar Selux is now owned by Consilium and named the Selux ST. It could not be confirmed that the Selux ST radar currently available is capable of dual-polarization or ice detection, as the information online does not indicate it is dual-polarized. The Rutter Sigma 6 is a processing system that is integrated to any radar through an RS-422 connection. Rutter does not produce their own radar system. Reviewing their online documentation, they appear to be using a vertically polarized Sperry marine navigation radar (exact model was not specified) and a horizontally polarized Consilium marine navigation radar for their testing [75]. In 2012, Rutter conducted a trial onboard the Canadian Coast Guard Ship (CCGS) Henry Larsen, using a dual-polarized X-band radar system to determine marine ice age (classification) [76]. The report does not specify the radars used, but they appear to be the same Consilium radars used in the previously mentioned trials.

Based on this, it appears that the Rutter Sigma 6 is capable of dual-polarization processing but that there currently is no dual-polarization marine radar system in production for ice classification.

3.11.2 McMaster University 1981 and 1983 Experimental Data

The McMaster University experiments were conducted using modified S, X, Ku and Ka-band dual-polarization radars. The radar was stationary and observing a land-fast shelf of FYI with MYI and GI inclusions. This experiment examined the scattering phenomena of ice due to changes in frequency and polarization. The key findings relevant to this work are summarized in this section.

Frequency: From the analysis of the normalized radar signature shown in Figures 3.15 and 3.16, reference [13] found the following:

a. S-band returns were strongly correlated to the target's significant vertical extent;
b. X and Ku-band returns detected surface features with much lower vertical extent, but presented a cluttered response that did not clearly display FYI pressure ridges, or icebergs (GI) trapped in the FYI;
c. Ka-band returns correlated well with hazardous ice features, such as icebergs, MYI floes and some FYI pressure ridges. It is important to note that the radar under test suffered from weak signal returns due to low transmitter power and may show performance improvement with a higher power transmitter.

The McMaster experiments also showed that frequency diversity could be used to classify marine ice types. In Table 3.2, the change in radar signature between S and Ka-band radar frequencies is significant and unique for FYI, MYI and GI. The differences between the X and Ka-band radar signatures for FYI and GI, and Ku and Ka-band radar signatures for FYI and MYI are too small (only 2dB difference) for classification. Small fluctuations in the radar signature due to the shape, orientation or composition of the ice target could cause a mis-classification between safe FYI and hazardous MYI or GI.

Table 3.2 Change in the co-polarized normalized RCS of ice as a function of change in frequency.

Feature	Change in σ_s (dBm^2)		
	From S to Ka	From X to Ka	From Ku to Ka
First-year ice	35	14	16
Multi-year ice	14	22	12
Glacier ice	20	12	4
Note: This table was adapted from Table 8.7 of [13].			

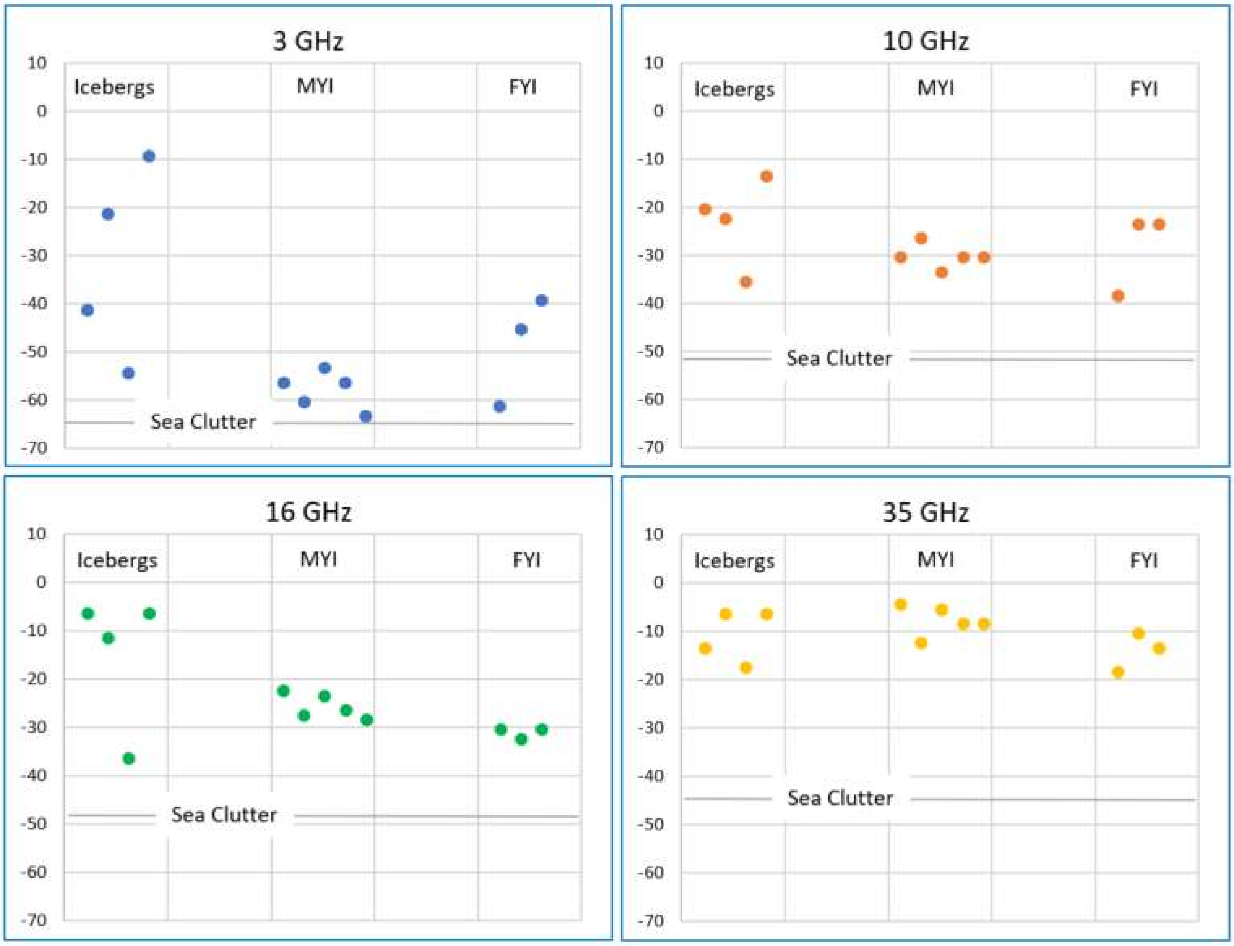

Figure 3.15 Plots of the normalized, co-polarized radar signature for marine ice at S, X, Ku and Ka-band (3, 10, 16 and 35 GHz respectively), adapted from Table 8.6 of [13]. The clutter level indicated is for Sea State 1 and a grazing angle of 1 degree, as found in [92].

Polarization: The experiments in 1981 showed distinct differences between the co- and cross-polarized radar signatures for the three marine ice types of interest at 9 GHz. The analysis was expanded in 1983 to include Ku- and Ka-band. However, due to the limitations of the X-band and

Ka-band radars which resulted in poor data collection, Haykin et al. [13] did not conduct a full analysis and comparison of the cross-polarization advantage of X- and Ka- bands against Ku-band. In particular, the Ka-band radar suffered from low transmit power, which resulted in weak co-polarized radar signature returns and even weaker cross-polarized returns, and was not included in their analysis. Despite this limitation, they were able to show that the use of co- and cross-polarized radar signatures can be used to assist in the classification of the marine ice types of interest.

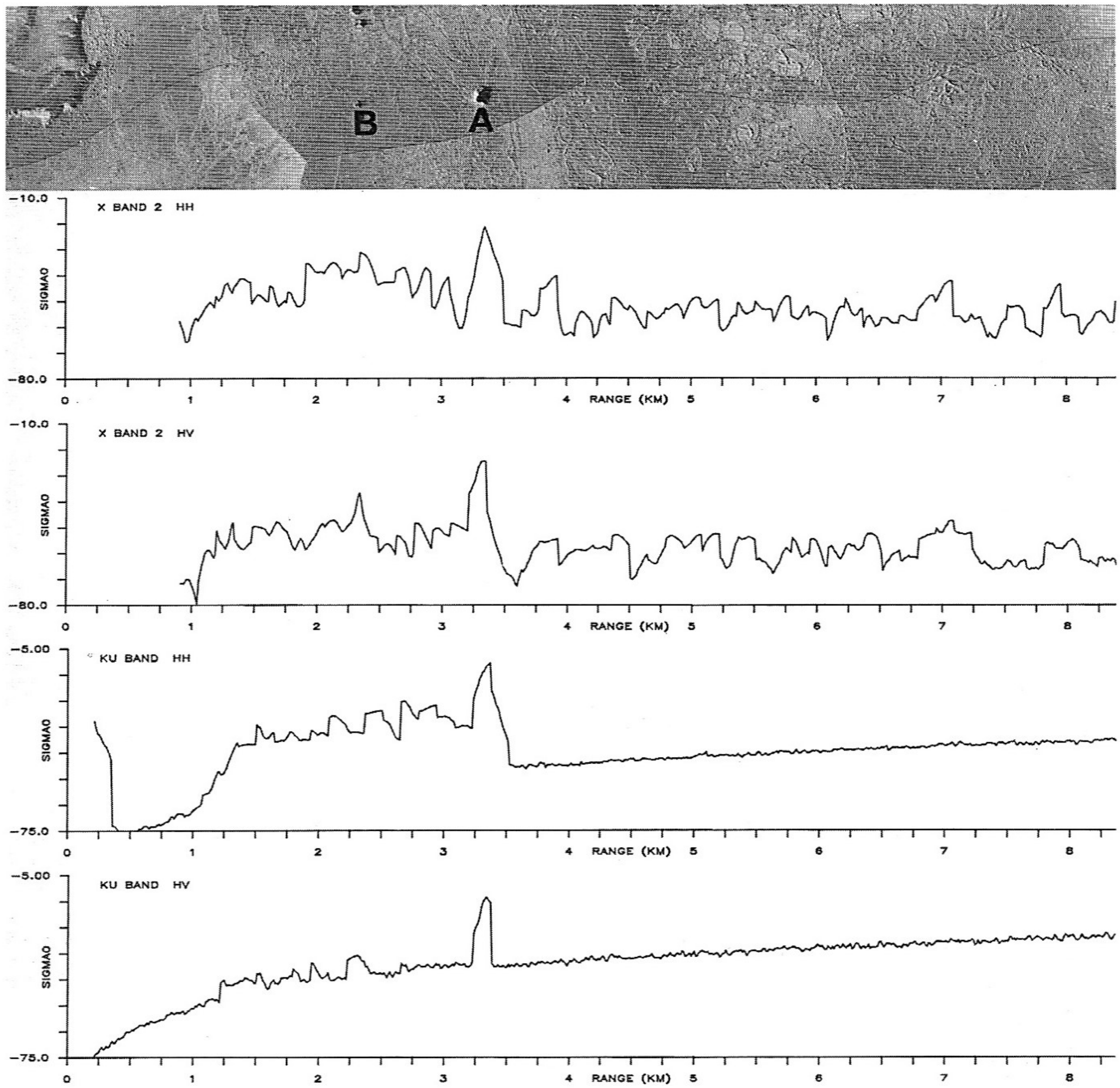

Figure 3.16 Photomosaic with co- and cross-polarized radar signature traces for X- and Ku-band. Target A is a large iceberg, approximately 45m high by 75m wide with a physical cross-section of 3400m^2. Target B is a small iceberg, approximately 300 m^2. Courtesy of Haykin et al [13, p. 379].

In Figure 3.16, it is clearly evident that the X- and Ku-band cross-polarized radar signatures provided an advantage over the co-polarized radar signature for the detection of the GI targets (targets A & B) trapped in the FYI floe. In the X-band co-polarized radar signature trace, target B would not be detected in the surrounding clutter caused by the FYI. However, in the cross-polarized radar signature trace, target B is 10dB greater than the surrounding clutter. The same effect is even more pronounced in the Ku-band co- and cross-polarized radar signature traces. This detection advantage was also observed for MYI targets trapped in the FYI floe. In fact, all known hazardous ice (ie. MYI and GI) in the radar traces were detected in the cross-polarized radar signature traces. An analysis of a large number of targets demonstrated a 10 to 17 dB target-to-clutter advantage for the detection of GI and a 7 to 10 dB advantage for MYI, using Ku-band radar. A limited analysis of X-band showed a similar advantage (6 to 7 dB) for the detection of GI.

Haykin et al. [13] indicated that the data that was collected for the Ka-band radar suggests that the cross-polarized radar signature would also provide a detection advantage for MYI and GI.

Furthermore, comparison of the co-polarized and cross-polarized radar signatures for a given target demonstrated that the degree of depolarization (the difference between the co- and cross-polarized signatures) directly correlated to the hazard level of the marine ice types. Figures 3.17 shows that the cross-polarized signature is low for FYI (-40 dB), higher for MYI and strongest for GI (-10 dB). Comparing the cross-polarized signature against the corresponding co-polarized signature for a given target also provides a method of classification, as shown in Figure 3.18.

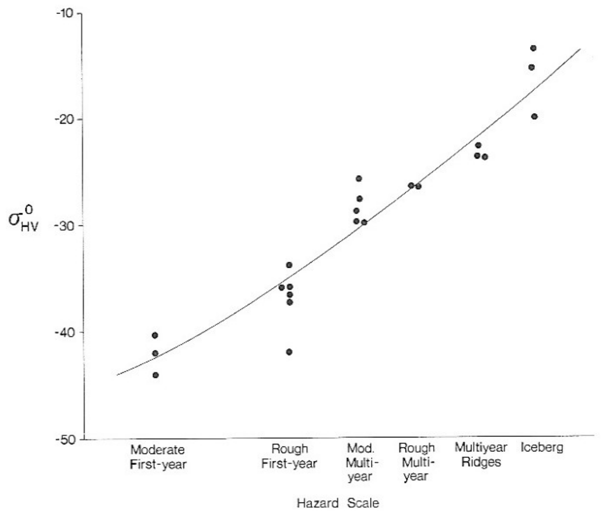

Figure 3.17 Plot of Ku-band cross-polarized radar signature (σ^o_{HV}) versus hazardous ice.

Figure courtesy of Haykin et al [13] Figure 8.22.

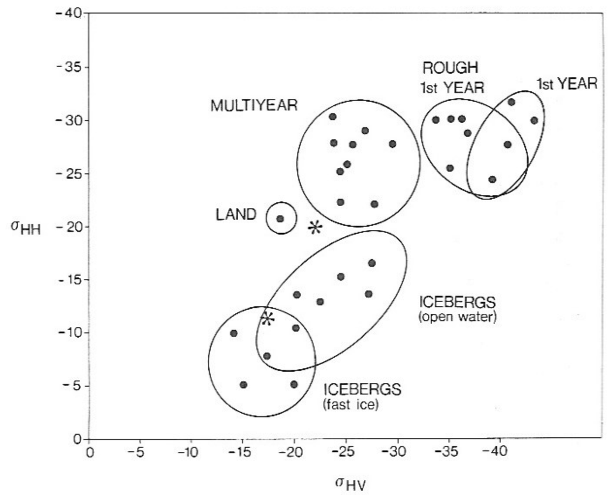

Figure 3.18 Plot of the co-polarized radar signature (σ^o_{HH}) versus cross-polarized radar signature (σ^o_{HV}). Dots represent Ku-band data and astrix (*) represents X-band data.

Figure courtesy of Haykin et al [13] Figure 8.23.

In summary, the McMaster experiments found:

a. S and Ka-band co-polarized radar signatures (3 and 35 GHz) provided better detection of ice targets than the X and Ku-band co-polarized radar signatures (9 and 16 GHz);
b. The difference between the co-polarized radar signature for the same target detected by S and Ka-band could be used to help classify the marine ice type;
c. The use of the cross-polarized radar signatures at Ku-band provided a target-to-clutter advantage for the detection of hazardous ice (MYI and GI), and may exist at all frequencies;
d. The comparison of the co- and cross-polarized radar signatures for a target could be used to help classify the marine ice type.

3.11.3 McMaster 1990 Experimental Data

In 1990, Orlando et al. [73] developed and tested the ability of their dual-polarized radar coupled with various post-processing classifiers to classify the three marine ice types of interest. The study was conducted using a Ku-band (16.5 GHz) dual-polarized radar. They found that MYI and GI targets depolarized the backscattered radar wave to higher degree than FYI, confirming the results shown in Figure 3.17 and theorized that this was due to deeper penetration and internal reflections in MYI and GI. Using the backscatter intensity, which translates to pixel intensities on the plan position indicator, the classifier used the co- and cross-polarized returns in combination, and separately, to attempt to classify the type of ice. At Ku-band, they found that the co-polarized return was enough for the one-dimensional Gaussian classifier to differentiate FYI from MYI or GI, but could not differentiate MYI from GI. Using cross-polarization, the classifier could further differentiate between MYI and GI. However, as can be seen in Figures 3.19 and 3.20, there is still significant overlap (~20% for co-polarization and ~50% for cross-polarization) in the pixel intensity from FYI, MYI and GI that can lead to mis-classification at this frequency.

The end goal of this work is to explore scattering from the three marine ice types (FYI, MYI and GI) and hopefully identify a frequency or range of frequencies at which safe ice (FYI) can be differentiated from hazardous ice (MYI and GI), by minimizing any overlap in the intensity of the co-polarized or cross-polarized backscatter intensity (pixel intensity), or by using the degree of depolarization to classify marine ice with a high degree of confidence (eg. >95%).

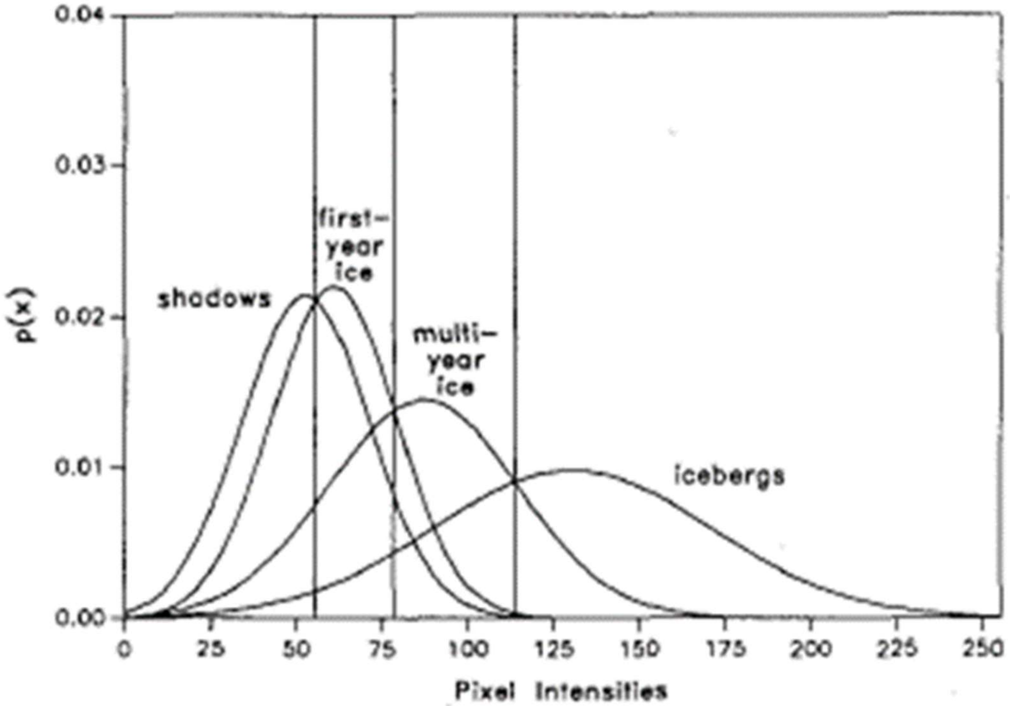

Figure 3.19 Gaussian approximation plots of the observed co-polarized pixel intensity distribution for FYI, MYI and GI (icebergs) using a Ku-band radar. Note the overlap (~50%) between in hazardous ice (MYI and GI) and safe ice (FYI). Figure courtesy of [73].

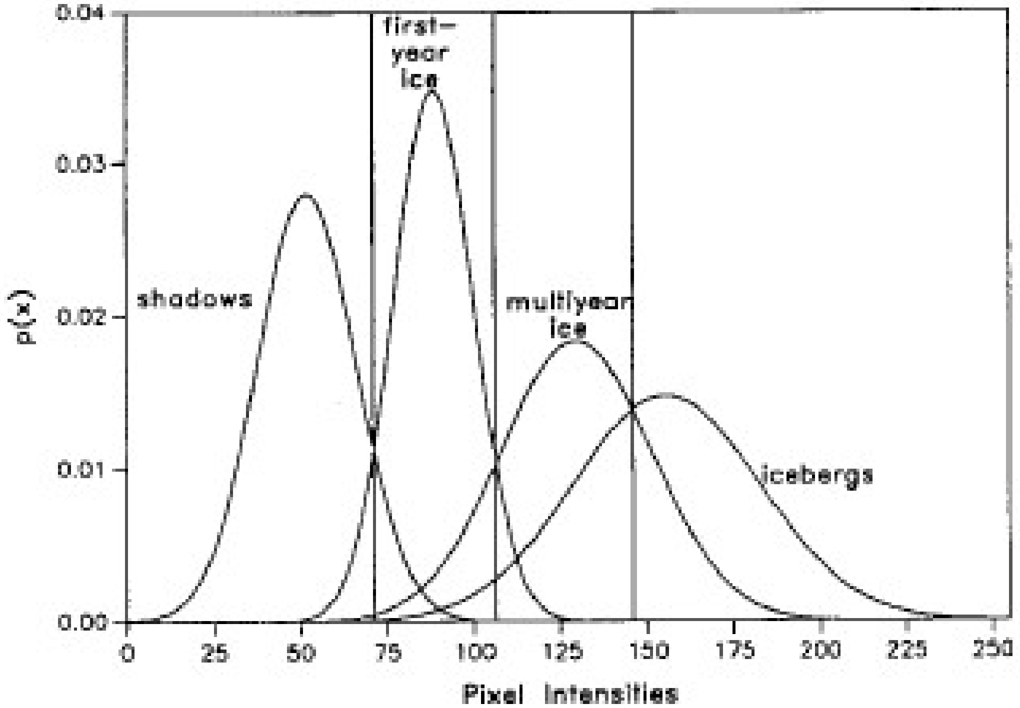

Figure 3.20 Gaussian approximation plots of the observed cross-polarized pixel intensity distribution for FYI, MYI and GI (icebergs) using a Ku-band radar. Note the overlap (~20%) between in hazardous ice (MYI and GI) and safe ice (FYI). Figure courtesy of [73].

3.12 Conclusions

A number of things have been achieved in this chapter. Firstly, we have successfully extracted the essence of the electromagnetic properties of marine ice from the scientific literature, and then coupled this to the so-called mixing theory for dielectrics. This is important because it now allows us to represent ice (with electrically small inclusions) as a homogeneous lossy dielectric. This will in turn be used be used in Chapter 4 to determine an effective complex permittivity for the three marine ice types of interest, namely First-Year Ice (FYI), Multi-Year Ice (MYI) and Glacier Ice (GI). Using this effective complex permittivity, engineering models for the far-zone scattering from marine ice on a sea surface can be developed. Secondly, we have clarified and connected otherwise seemingly disparate definitions of various radar cross section related concepts. This will permit us, in Chapter 5, to use existing experimental data on scattering from marine ice, to validate the scattering results obtained using the computational electromagnetics models (that is, engineering models) in Chapter 4.

A summary of some of the findings described in this chapter are in order. The physical and electrical properties of marine ice change over time. The period of interest to this study is the Canadian Arctic marine navigation season, from approximately June to October, when the three ice types are present. At this time, the air temperature averages between -1°C to +4°C, and the average sea surface temperature is between -2°C to +4°C. The salinity of the seawater in the Northwest Passage is between 29 to 34 ppts. FYI forms in tabular plates, floating 0.1 to 0.2m above the surface with sharp edges and a relatively smooth upper surface. The top layer of FYI is an isotropic, heterogenous mixture of pure ice, brine and air. MYI is formed from FYI that has undergone one or more melt-freeze cycles. It floats 0.2 to 0.4m above the surface and has smoother edges, a rougher surface marked with hummocks and angular pressure ridges. MYI is an isotropic mixture of pure ice, air and to a lesser extent brine. GI is formed from glaciers and shows great variation in size and shape, from tabular to domed to pinnacles of ice. GI tends to float significantly higher out of the water than FYI and MYI. GI is an isotropic, heterogeneous mixture of pure ice and air. Extensive research has been conducted with respect to satellite-based radar remote sensing of marine ice in the past 50 years and is ongoing. However, there has been limited open source research conducted in the area of surface-based radar remote sensing of marine ice. The research that occurred was funded by the Canadian Coast Guard through the National Research Council in the 1980s and 1990s. The research was conducted by Haykin et al. through McMaster University and involved commercial industry leaders such as Rutter, Raytheon and InfoTech (now FedNav). This experimental research was conducted at four discrete frequencies and focused on modifying existing marine navigation radars to receive dual-polarization, and using advanced digital signal processing to improve the ice detection and imaging capabilities of the radar. These experiments showed that the concepts used in satellite-remote sensing of marine ice, namely dual-frequencies and dual-polarization, are applicable to surface-based radar remote sensing of marine ice. However, despite this promising research, funding and interest seems to have waned in the 2000s. As a result, there are currently no commercially available, dual-polarization marine navigation radars capable of classifying marine ice.

4. Model Construction & Methodology

4.1 Introduction

This chapter is organized into the following sections:

Section 4.2 – Geophysical Parameters;

Section 4.3 – Size and Shape of the Marine Ice Targets;

Section 4.4 – Permittivity of the Constituent Materials;

Section 4.5 – Permittivity of Marine Ice (divided into FYI, MYI and GI);

Section 4.6 – Permittivity of Seawater;

Section 4.7 – Antenna Models;

Section 4.8 – Construction of Reliable Computational Electromagnetic Scattering Models;

Section 4.9 – Conclusions.

This study uses the computational electromagnetic (CEM) software FEKO™ by Altair [77] to solve for the co- and cross-polarized monostatic backscatter intensity of marine ice targets. As indicated in Section 3.7, this study uses the full wave electromagnetic analysis obtained from the method of moments solution of the PMCHWT integral equation formulation obtained from Maxwell's equations. The presence of the sea surface is accounted for using a modified Green's function (eg. PEC surface, dielectric halfspace effects approximated by Fresnel reflection coefficients, or dielectric halfspace effects rigorously accounted for using the Sommerfeld theory) in the integral equation.

To build the CEM engineering models of marine ice, it is necessary to know the size, shape and the permittivity of the ice targets, the permittivity of the seawater, and the angle of the incident wave. The engineering decisions and calculations required to build the models are detailed in Sections 4.2 through 4.6.

Section 4.7 describes a contribution to the modelling of the radiation patterns of actual antennas from spherical near-field measurements, to find their patterns when they are mounted on a platform. It was originally envisioned to use an actual navigation radar radiation pattern to calculate the scattered field from the ice object in the presence of the platform. However, it turned out this was not needed for the backscatter computations of interest in this work but has been retained here for completeness.

Finally, in Section 4.8, three aspects of electromagnetic modelling are studied:

a. the minimum mesh size required, at 10GHz, for accurate (far-zone) backscatter intensity computations;
b. whether, again to obtain accurate backscatter intensity results, the flat sea can be modelled as a PEC halfspace, or whether the Fresnel reflection coefficient or the more rigorous Sommerfeld half-planes must be used; and
c. given the typical ice-object sizes identified in Table 2.1 of Section 2.2 and Section 4.3, can scaled down ice objects provide information about the overall backscatter intensity patterns of the full-sized object.

The chapter is rounded off with some concluding remarks in Section 4.9.

4.2 Geophysical Parameters

The natural world is highly variable. This work involves modelling marine ice and seawater, which are naturally occurring geophysical materials whose properties are dependent on a number of environmental factors. In the Canadian Arctic, temperatures can drop below -50°C in the winter and rise as high as 30°C in the summer. It can rain or snow. The ocean can be flat and calm, have waves several metres high or somewhere in between. Modelling the effect of each of these factors would take years and is not the primary focus of this study. It is therefore necessary to limit the scope through some assumptions about the environmental conditions and the marine ice; these are outlined and discussed in Sections 4.2.1 and 4.2.2. The assumptions must, of course, ensure that the CEM models still emulate the real world.

4.2.1 Environmental Conditions

The period of interest is this study is the summer navigation season from about June to October. During this period, the weather is relatively stable and storm free. The specific area of interest is the Northwest Passage. From historical weather data, discussed in Section 3.2, the following environmental conditions were assumed in the permittivity calculations:

a. Average air temperature = +2°C;
b. Average sea surface temperature = 0°C;
c. Average seawater salinity = 30 parts per thousand (ppt);
d. Average ice temperature = -2°C; and
e. Sea state 1, waves < 0.2 metres.

As discussed in Section 3.6, the permittivity of seawater is a function of temperature and salinity. A salinity of 30 ppt will be used in the models: the average of the surface water salinity, as discussed in Section 3.2. However, as will be shown in Section 4.6, the dominant factor, in the ranges of temperature and salinity expected in the Canadian Arctic, is temperature. The sea surface temperature can range from -2°C to +4°C. During the melt season, the sea surface temperature would be above the freezing point of seawater at -1.8°C, so an average sea surface temperature of 0°C will be used.

In reality, the ice temperature is not uniform throughout the bulk of the ice. At the air-ice interface and the seawater-ice interface, the ice will be in equilibrium or near equilibrium with the surrounding air or seawater temperature. If the air or seawater temperature is above freezing, the outer surface of the ice will be at the freezing point of ice (otherwise it has turned to liquid water). Internally, the temperature of the ice will have cooled to well below the freezing point by the cold winter temperatures, such that the temperature profile is C-shaped, as described in Section 3.3.1. This would cause the permittivity of the marine ice to change with depth. However, this can be ignored, and the engineering model can be assumed to be of uniform temperature and permittivity because this study is only interested in the portion of the marine ice above the waterline where, as will be discussed in Section 4.5.4, the range of temperature change expected will have minimal effect on the permittivity. Thus, a homogeneous object whose properties are those of the actual object near the air-ice interface is satisfactory.

Finally, the models will assume a perfectly flat sea due to the limitations of the CEM software and out of necessity to reduce the computational resources required. In reality, the sea surface during the period of interest could be near flat to swells up to 0.2 m. The effects of which cannot be easily accounted for analytically in these models and would drastically increase the computational resources required to solve the models. This will need to be an area for future study.

4.2.2 Marine Ice

All three types of marine ice in this study will be assumed to have following properties:

a. The upper layer, which interacts with the electromagnetic wave, is isotropic;
b. There is no snow or water layer present on the upper surface of the ice; and
c. Impurities in the ice can be ignored in the calculation of the effective permittivity;

As discussed in Section 3.3, the upper layers of FYI and MYI tend to consist of randomly distributed and oriented near-spherical or spherical inclusions, and GI consists of randomly distributed spherical inclusions. This material would have an isotropic permittivity. Even if the non-spherical inclusions (brine pockets) where aligned, the alignment results in an axially anisotropic material whose x- and y-directed permittivities are equal and the z-directed permittivity is a different value. Therefore, in the calculation of the effective permittivity below, the Maxwell Garnett mixing formula for an isotropic material will be used for the three marine ice types. In reality, the temperature in the ice would not be uniform and the permittivity of the marine ice is a function of temperature. As will be shown in Section 4.5.4, the permittivity of the marine ice does not change significantly over the range of temperatures expected in the upper layer of the ice influenced by the electromagnetic wave. Therefore, the temperature and permittivity can be assumed to be uniform in the upper layers.

Livingstone et al. [70] noted that under the conditions found in spring, summer and fall, the backscatter signature of marine ice is dynamic and changes with the environmental conditions. This is because marine ice and snow are comprised of water, whose permittivity changes significantly depending on whether it is in the form of ice, snow or liquid. Even small amounts of liquid water in snow or on the surface of the ice can drastically alter the microwave signature [69]. However, it will be assumed that there is no snow or water layer present in this study. This will need to be an area for future study.

Cox and Weeks [30] found that near the freezing point of the seawater, solid salt precipitates do not exist in sufficient quantities to affect the permittivity of marine ice. Therefore, only the pure ice host medium, and air or brine inclusions, will be considered in the calculations of the effective permittivities of FYI, MYI and GI in Section 4.5.

4.3 Size and Shape

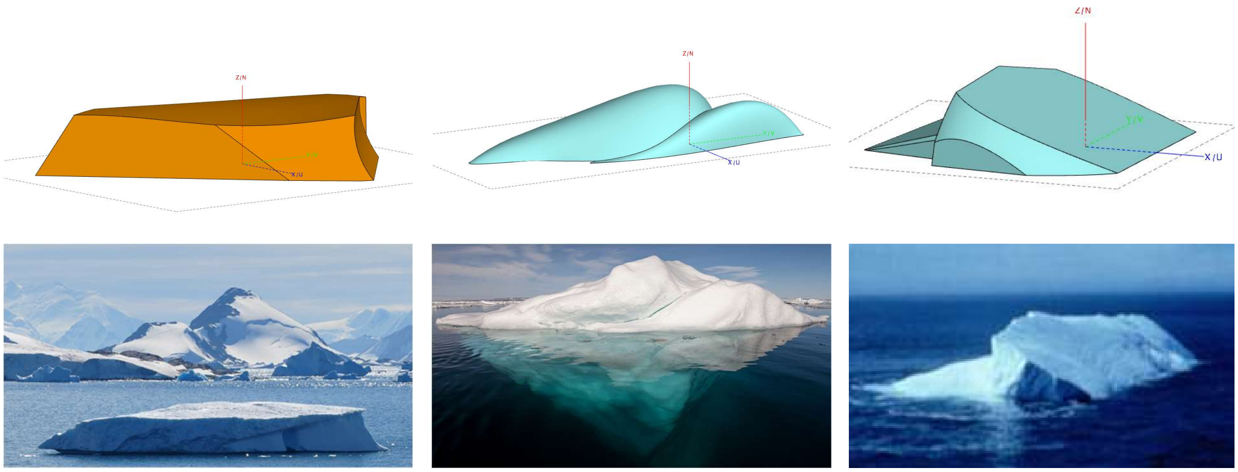

Figure 4.1 Real world marine icebergs (bottom) and the associated CAD model (top) for use in the study of backscattering from marine ice. It is possible for FYI, MYI and GI to have very similar tabular forms.

Marine ice is a naturally occurring, highly variable material. This is true of both the material composition and the shape of the ice. However, as discussed in Chapter 3, one shape is common to the three ice types of interest: a tabular ice floe. FYI targets exist primarily as tabular plates of ice that float approximate 0.1 to 0.2m above sea level. MYI targets also exist primarily as tabular plates of ice, but are normally thicker, and float at approximately 0.2 to 0.4m above sea level. GI targets comes in a variety of sizes and shapes, such as pinnacle, domed, wedge and tabular icebergs. GI targets normally float 1m or more above sea level.

In this study, first the scattering from the common tabular shape will be investigated to gain an understanding of the degree to which surface and volume scattering affect the backscatter signature, then the size and shape of MYI and GI will be modified within their size and shape parameters for comparison against the FYI. Figure 4.1 provides examples of real world marine ice targets and the respective model.

4.4 Permittivity of the Constituent Materials

As discussed in Chapter 3, marine ice is a complex, heterogeneous mixture of pure ice, air and (in the case of FYI and MYI) brine. This could be modelled using a volume integral equation formulation to account for the inhomogeneity caused by the inclusions. However, modelling the physical structure alone would be time-consuming and solving the volume integral equation formulation using the method of moments would not be computationally feasible (at this time)[22]. Fortunately, when the goal is to compute the far-field scattered field only, this is not necessary, and it will be shown in Chapter 5 that the surface integral formulation will suffice.

To model this material in a computationally efficient manner, it is necessary to idealize the geometric representation, such that the scattering from the idealized model approximates the actual material. This is achieved by calculating an effective permittivity using mixing theory, as discussed in Section 3.5, and homogenizing the material. To calculate an effective permittivity, it is necessary to know the permittivity and fractional volume of the constituent materials: pure ice, air and brine. The following sections will calculate the permittivity of the constituent materials using the equations in Section 3.6. These will be applied in Section 4.5 to calculate the effective permittivity of the three marine ice types of interest.

4.4.1 Pure Ice (Host Medium)

The real part of the permittivity of pure ice is frequency independent and a function of temperature. Using equation 3.28 and assuming an average ice temperature of -2°C, the real part of the permittivity of pure ice is:

$$\varepsilon_h' = 3.1866$$

The imaginary part of the permittivity of pure ice is a function of frequency and temperature. Using equation 3.29, the imaginary part of the permittivity of pure ice can be written as a function of frequency at a temperature of -2°C as:

$$\varepsilon_h'' = \left(\frac{7.75 \times 10^{-4}}{f}\right) + (6.00 \times 10^{-5})\, f^{(1.07)} \qquad (3.29)$$

---

[22] Although the computational resources exist on the Compute Canada High Performance Computing network, access to sufficient resources are not available to the author at this time.

The midway point between the Johari and Charette, and the Auty and Cole coefficient values, derived through experimentation [55] [54] [56] [73]and presented in Tables 3.1 through 3.3 in Section 3.6.1, were used in the curve fitting equation above.

4.4.2 Air (Inclusions 1)

The permittivity of air is normally assumed to be 1. However, the actual value is given by [57] as:

$$\varepsilon'_{air} = 1.0006$$

The loss factor (imaginary part) of the permittivity of air is negligible.

4.4.3 Brine (Inclusion 2)

The permittivity of the brine inclusions is more complex to calculate because it is a function of frequency, temperature and salinity. The permittivity of the brine is a function of frequency and temperature and can be represented using the Debye single relaxation frequency model given by equation 3.30. Substituting the values calculated in equations 3.31 to 3.39, into equation 3.30 gives the permittivity of the brine at -2°C as a function of frequency as:

$$\varepsilon_{br} = 5.50 + \frac{70.3859}{1 + j\omega(1.8186 \times 10^{-11})} - j\frac{3.0617}{\omega(8.8542 \times 10^{-1}\ )}$$

4.5 Permittivity of Marine Ice

Applying the permittivities of the constituent materials calculated in Section 4.4, the effective permittivity of the three marine ice types of interest were calculated using the mixing theory discussed in Section 3.5. The permittivities of sea ice (FYI and MYI) were calculated using equation 3.25 for a randomly oriented, three phase mixture taken from Sivhola [43]:

$$\varepsilon_{eff} = \varepsilon_h + 3\varepsilon_h \frac{\sum_{k=1}^{K} f_k \frac{\varepsilon_{i,k} - \varepsilon_h}{\varepsilon_{i,k} + 2\varepsilon_h}}{1 - \sum_{k=1}^{K} f_k \frac{\varepsilon_{i,k} - \varepsilon_h}{\varepsilon_{i,k} + 2\varepsilon_h}} \tag{3.25}$$

The permittivity of GI was calculated using equation 3.17 for a randomly oriented, two phase mixture:

$$\varepsilon_{eff} = \varepsilon_h + 3f\varepsilon_h \frac{\varepsilon_i - \varepsilon_h}{\varepsilon_i + 2\varepsilon_h - f(\varepsilon_i - \varepsilon_h)} \tag{3.17}$$

where

ε_h is the permittivity of the host medium;

ε_i is the permittivity of the inclusion medium; and

f_k is the volume faction of the inclusion medium with respect to the overall volume of the material.

The fractional volume was calculated using the equations developed by Cox and Weeks [30]. These equations calculate the fractional volume based on the density of the ice for a two phase mixture of pure ice and air (ie. GI) or the density of the ice, the bulk ice salinity and the salinity of the brine for a three phase mixture of pure ice, air and brine (ie. FYI and MYI). For FYI and MYI, the fractional volume of air, f_{v_air}, is given by:

$$f_{v\_air} = \left(1 - \frac{\rho_{total}}{\rho_{pure\ ice}}\right) + \left(\rho_{total} \frac{S_{total}}{S_{br}}\right)\left(\frac{1}{\rho_{pure\ ice}} + \frac{1}{\rho_{br}}\right) \tag{4.1}$$

and the fraction volume of the brine, f_{v_br}, is given by:

$$f_{v\_br} = \frac{\rho_{total}\, S_{total}}{\rho_{br}\, S_{br}} \tag{4.2}$$

For GI, equation 4.1 simplifies to give the fractional volume of the air, f_{v_air}, as:

$$f_{v\_air} = \left(1 - \frac{\rho_{total}}{\rho_{pure\ ice}}\right) \tag{4.3}$$

where

ρ_{total} is the bulk ice density;

S_{total} is the bulk ice salinity;

$\rho_{pure\ ice}$ is the theoretical density of pure ice (without air or brine inclusions) and is given by:

$$\rho_{pure\ ice} = 0.917 - 1.403 \times 10^{-4} T(°C) \qquad [g/cm^3] \tag{4.4}$$

ρ_{br} is the density of the brine and is given by:

$$\rho_{br} = 1 + 0.0008\, S_{br} \qquad [g/cm^3] \tag{4.5}$$

4.5.1 First-Year Ice

Recall in Section 3.3.1 that by the time the summer melting period begins, FYI has reached a thickness of approximately 1 to 2 metres thick, with a density of 0.920 to 0.960 grams/centimeter^3. As a result, 9/10th of the ice bulk is below the surface with approximately 0.1-0.2 metres of ice floating above the surface.

In the engineering model of FYI, it is assumed that only the portion of the ice floating above sea level influences the backscatter signature. The bulk ice salinity of FYI during summer is between 0.5 to 4 ppt in the top 50 cm (see Section 3.3.1). The bulk salinity of the FYI in the models will be assumed to be in the upper range at 4.0 ppt, as would be expected in the early part of the melt season, when it is more difficult to visually determine FYI from MYI.

Since brine has a higher density (>1.026 g/cm^3) than pure ice (0.9167 g/cm^3): ice with a higher bulk salinity (greater fractional volume of brine) will have a higher density. By the mid-summer, FYI has undergone significant desalination. Therefore, the density of FYI during the period of interest will be in the lower end of the range and will be assumed to be 0.920 g/ cm^3.

A summary of all values used in the calculations is provided at Table 4.1.

Table 4.1 Summary of the parameters and references used to calculate the fractional volume of first-year ice.

Variable	Value	Validity	Reference
Bulk ice salinity	4-8 ppt 0-4 ppt $S_{FYI} = 4.0\,ppt$	From 2 weeks after freeze-up to start of melt season Upper 0-50 cm of depth in June/July (start of melt season)	Weeks & Ackley 82 Nakawo 83 Holt et al 85
Bulk ice density	0.92-0.96 g/cm^3 $\rho_{FYI} = 0.920\,g/cm^3$	From freeze-up to melt season	Vant et al 1978 Haykin et al 1994

The salinity of the brine is a function of the temperature and given by equation 3.36 in Section 4.4.3 as:

$$S_{br} = 37.5636\,ppt$$

Recalling equation 4.5, the density of the brine therefore becomes:

$$\rho_{br} = 1.0301 \quad g/cm^3$$

Substituting the density and salinity values above into equations 4.1 and 4.2 give the fractional volume of air, f_{v_air} , as:

$$f_{v\_air} = \left(1 - \frac{0.920}{0.9173}\right) + \left(0.920\frac{4}{37.5636}\right)\left(\frac{1}{0.9173} + \frac{1}{1.0301}\right)$$

$$f_{v\_air} = 0.1989$$

and the fractional volume of the brine, f_{v_br}, as:

$$f_{v\_br} = \frac{(0.920)(4)}{(1.0301)(37.5636)} = 0.0951$$

The effective permittivity of FYI can now be calculated by substituting the fractional volumes and permittivities of the constituent materials into equation 3.25. The resulting effective permittivity of FYI in the frequency range of interest is given in Table 4.3.

4.5.2 Multi-Year Ice

As discussed in Section 3.3.2, by the time the summer melting period begins, MYI has reached a thickness of approximately 2 to 4 metres thick, with a density of 0.800 to 0.900 grams/centimeter^3. As a result, 8/10th to 9/10th of the ice bulk is below the surface with approximately 0.2-0.4 metres of ice floating above the surface.

In the engineering model of MYI, there is significant penetration of the electromagnetic field into the ice target (penetration depth of approximately 1.15 m 6 GHz). Multi-year ice is normally rougher on the top surface than FYI and is characterized by hummocks and depressions, and large melt ponds with defined drainage channels during the late melt season. The hummocks can reach up to 4 m above sea level. The salinity of MYI is normally < 1 ppt below hummocks and above sea level, increasing from 2 ppt at sea level to 4 ppt at the ice-seawater interface (see Section 3.3.2). The bulk salinity of the MYI in the models will be assumed to be at the mid-point of 0.5 ppt for the portion of the ice above sea level.

Since the bulk ice salinity is so low in MYI it is often considered negligible and can be left out of the mixing formula calculation of the permittivity. However, it was included in the calculations in this work. The mid-point for the bulk ice density of MYI is 0.850 g/cm^3 and was used in the calculation of the permittivity. A summary of the values used in the calculations is provided at Table 4.2.

The salinity of the brine is a function of the temperature and is the same as for the brine in the FYI. Therefore, the salinity and density of the brine in MYI is the same as for FYI above.

Therefore, substituting the density and salinity values above into equations 4.1 and 4.2 give the fractional volume of air, f_{v_air} , as:

$$f_{v\_air} = \left(1 - \frac{0.850}{0.9173}\right) + \left(0.850 \frac{0.5}{37.5636}\right)\left(\frac{1}{0.9173} + \frac{1}{1.0301}\right)$$

$$f_{v\_air} = 0.0967$$

and the fractional volume of the brine, f_{v_br}, as:

$$f_{v\_br} = \frac{(0.850)(0.5)}{(1.0301)(37.5636)} = 0.0110$$

The effective permittivity of MYI can now be calculated by substituting the fractional volumes and permittivities of the constituent materials into equation 3.25. The resulting effective permittivity of FYI in the frequency range of interest is given in Table 4.3.

Table 4.2 Summary of the parameters and references used to calculate the fractional volume of multi-year ice.

Variable	Value	Validity	Reference
Bulk ice salinity	<1 ppt	Above sea level in March/April	Vant et al 1978 Cox & Weeks 1974 Timco & Weeks 2010
	2-4 ppt	Below sea level increasing to 4 ppt at ice-seawater interface in March/April	Cox & Weeks 1974 Holt et al 85
	$S_{FYI} = 0.5\,ppt$		
Bulk ice density	0.800 – 0.900 g/cm^3 $\rho_{FYI} = 0.850\,g/cm^3$		Vant et al 1978 Haykin et al 1994
Fractional volume of air	Typically 0.05 to 0.2		Meeks et al 1974 from Weeks & Ackley 1982

4.5.3 Glacier Ice

As discussed in Section 3.3.3, GI is formed on land from fresh water. As such, it is devoid of brine inclusions. GI is also tends to be denser than MYI with a density around 0.900 g/cm^3, with a fractional volume of air between 4% to 9%. GI is normally fairly uniform in the density and has a random distribution of air inclusions.

In the engineering model of GI, the density was selected to be 0.860 g/cm^3, so that the density was slightly higher than the MYI model and to achieve a fractional volume approximately at the mid-point of the expected fractional volume. This density resulted in a fractional volume of air of 6.24%.

The fractional volume of the air, f_{v_air}, is given by equation 4.3 such that:

$$f_{v\_air} = \left(1 - \frac{0.860}{0.9173}\right) = 0.0624$$

The effective permittivity of GI can now be calculated by substituting the fractional volumes and permittivities of the constituent materials into equation 3.17. The resulting effective permittivity of FYI in the frequency range of interest is given in Table 4.3.

Table 4.3 Complex permittivity values for the engineering models of marine ice. These values are valid for the above ice portion of marine ice at an ice temperature of -2°C during the onset of the summer melt season.

Frequency [GHz]	Permittivity		
	FYI	MYI	GI
6	3.4424 – j 0.0726	3.0113 – j 0.0081	3.0113 – j 0.0004
8	3.4372 – j 0.0902	3.0108 – j 0.0100	3.0113 – j 0.0005
10	3.4310 – j 0.1083	3.0102 – j 0.0120	3.0113 – j 0.0006
12	3.4238 – j 0.1263	3.0094 – j 0.0140	3.0113 – j 0.0007
14	3.4155 – j 0.1439	3.0086 – j 0.0160	3.0113 – j 0.0009
16	3.4063 – j 0.1608	3.0077 – j 0.0179	3.0113 – j 0.0010
18	3.3962 – j 0.1770	3.0066 – j 0.0198	3.0113 – j 0.0011
20	3.3853 – j 0.1924	3.0055 – j 0.0216	3.0113 – j 0.0012

4.5.4 Effects of Temperature Variations on the Permittivity of Marine Ice

As mentioned in the assumptions, the upper layers of the marine ice which interact with the electromagnetic wave will be assumed to be uniform in temperature and permittivity. Using mixing theory and adjusting the temperature in the range expected in the upper layers, Figure 4.2 shows the temperature dependence of the permittivity of marine ice. The real permittivity is unaffected. The imaginary part of the permittivity for FYI and MYI decreases directly proportionally with temperature. However, the order of magnitude difference between FYI and MYI, and MYI and GI is maintained. This is important as it will be shown that this property allows for the determination (or classification) between FYI, MYI and to a lesser extent GI. The imaginary part of the permittivity of GI is unaffected. Since the changes to the permittivity over this temperature range are minimal (less than an order of magnitude) or negligible, the permittivity of the upper layers of the marine ice can be assumed to be uniform.

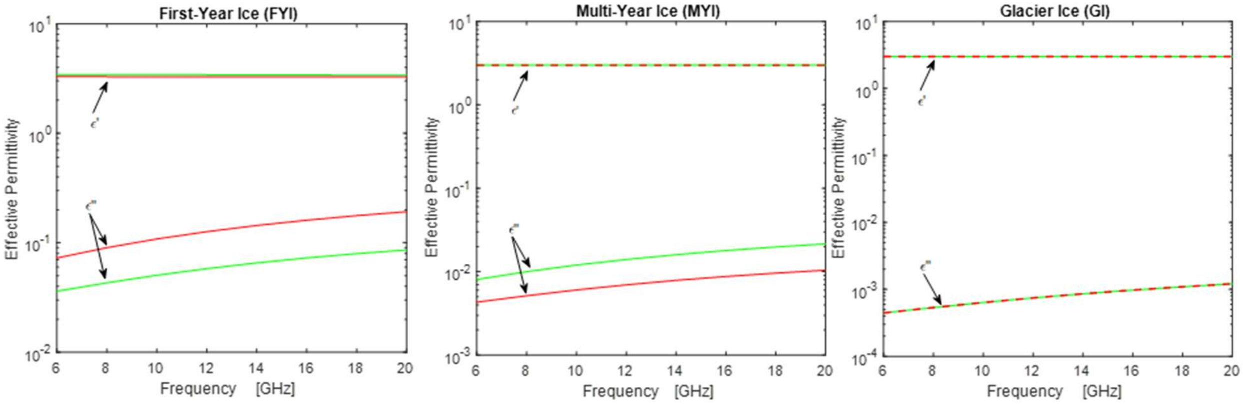

Figure 4.2 Graphs of the permittivity of marine ice as a function of temperature. The green lines (-) represent the permittivity at a temperature of -2°C and the red lines (-) represent the permittivity at a temperature of -5°C. The dashed lines are to show that the green and red traces overlap.

4.6 Permittivity of Seawater

The permittivity of seawater is dependent on the salinity, S, and the temperature, T, of the seawater, as well as the frequency. The salinity is assumed to be 30 ppt and the temperature during the period of interest is assumed to be 0°C (See Section 4.2.1). The permitivity of the seawater is calculated by substituting the parameter values in equations 3.41 through 3.55 into the Debye double relaxation frequency model given in equation 3.40. The resulting permittivity of seawater is a function of frequency with the values in the range of 6 to 20 GHz presented in Table 4.4.

Table 4.4 Permittivity of seawater in the Canadian Arctic between 6 and 20 GHz for a salinity of 30 ppt and a sea surface temperature of 0°C.

Frequency [GHz]	Permittivity	Real Permittivity	Loss Tangent, $\tan\delta$
6	58.4688 -j 40.4589	58.4688	0.6920
8	48.9237 -j 41.7972	48.9237	0.8543
10	40.7558 -j 41.2962	40.7558	1.0133
12	34.1652 -j 39.7161	34.1652	1.1625
14	28.9769 -j 37.6386	28.9769	1.2989
16	24.9186 -j 35.4127	24.9186	1.4211
18	21.7344 -j 33.2237	21.7344	1.5286
20	19.2161 -j 31.1597	19.2161	1.6215

4.6.1 Effects of Temperature and Salinity Variations on the Permittivity of Seawater

In the real world, the temperature and salinity of the seawater would rarely be uniform with depth or in a region. Figure 4.3 illustrate that the permittivity of seawater is fairly sensitive to changes in the temperature but not to salinity in the expected ranges of salinity and temperature discussed in Section 3.2. However, the penetration depth of seawater is 8.7 cm at 6 GHz and decreases as the frequency increase, such that the penetration depth is 6.5 mm at 20 GHz (see equations 3.26 and 3.27). Therefore, in this thin layer, the surface temperature of the seawater can be assumed to be constant and hence the permittivity is a constant.

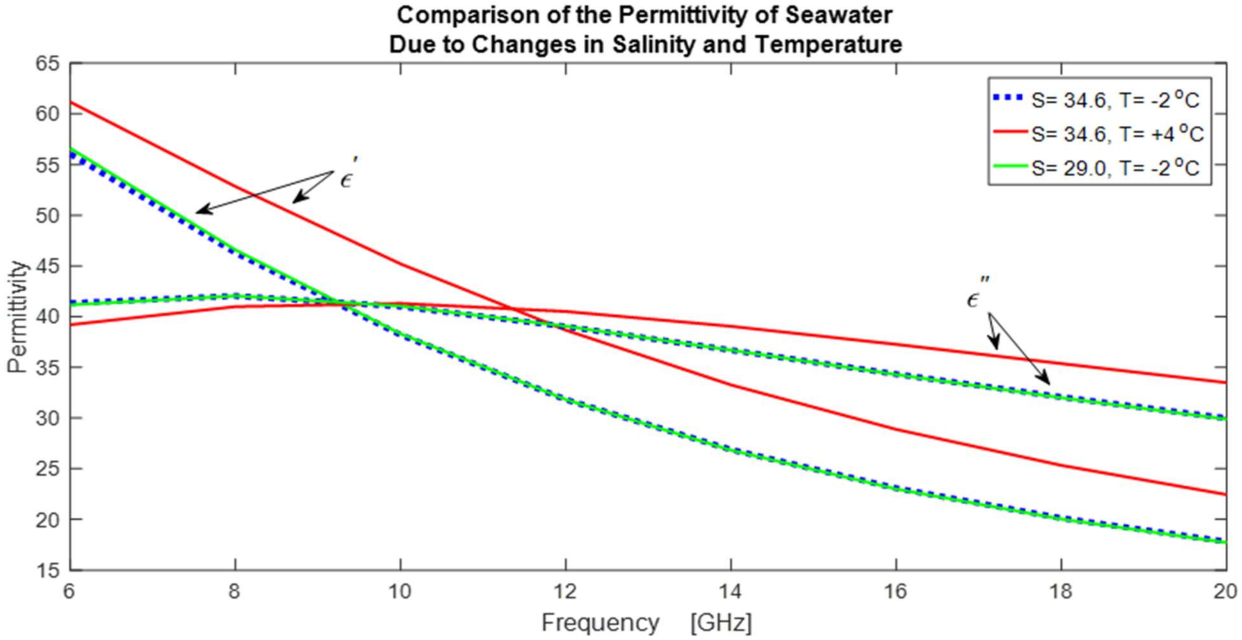

Figure 4.3 Comparison of the permittivity of seawater due to changes in the salinity and temperature of the seawater. The figure illustrates that temperature is the dominate factor in the permittivity of seawater and that changes in the expected range of salinity have negligible effect.

4.7 Antenna Modelling

It is well-known that when an antenna is mounted on a complex platform (eg. ship; aircraft; land-vehicle) its radiation pattern is altered by the presence of the platform. Much effort may be needed to model the effect of the platform to determine a suitable location for the antenna, to ensure the pattern performance will not be so distorted as to render it inadequate for its intended system function. The availability of commercial computational electromagnetic modelling (CEM) software and modern computing power has, over the past 30 years, made theoretical trade-off studies of platform-based antennas possible and (almost) routine. In most instances, the modelling of the platform itself is computationally taxing. Fortunately, detailed modelling of the actual antenna is not needed, if only pattern effects are of interest (as opposed to input/output port return loss, and coupling to other antennas [78]). Thus, equivalent source distributions have been successfully used to emulate actual antenna patterns in such placement modelling applications for many years, starting with those for quite simple antennas [79]. Since the late 1990’s commercial CEM software suites, such as FEKO (Altair) [77], CST (Dassault) [80], and HFSS (Ansys) [81], have become widely available. Initially, software suites were developed around a single CEM approach but have evolved to allow the user to select the approach (eg. method of moments, finite element method, asymptotic and hybrid methods) that is best suited to the particular problem.

As with many things in engineering, once a new tool becomes established the demands on the technique are steadily tightened in attempts to answer increasingly difficult technical questions.

In the case of on-platform antenna placement studies (assuming platform details are being properly modelled), this has resulted in queries as to how precise the equivalent-source modelling of the target antenna radiation patterns can be or needs to be. Any response to the latter questions must consider not only the theoretical advances that have occurred, but also the significant improvement in the information available from modern antenna measurement techniques and systems. Many antennas are now being tested in spherical near-field (SNF) measurement facilities. However, this information does not appear to be commonly used in antenna placements studies, yet. It is the use of this detailed data to represent the antenna in CEM simulations that is being proposed and demonstrated here.

Once SNF measurements have been performed on an antenna, this information may be used in the following hierarchy of (decreasing fidelity) formats:

a. Spherical wave coefficients computed from the measured near-fields;

b. Tabulated near-zone data (amplitude and phase) over a chosen surface close to the antenna (defined by cartesian, cylindrical or spherical coordinates); or

c. Tabulated far-zone data (amplitude and phase) in selected pattern cuts.

The spherical wave coefficients (SWC) can be directly imported into the CEM model of the platform in most CEM software suites and provides the most accurate representation of the actual antenna. Consider the example of a naval E/F-band search radar that was tested on a SNF range. Figure 4.4 is a graphical reconstruction of the exact 3-dimensional radiation pattern (in free-space) created by importing the SWC into FEKO, for use in the platform studies. The advantage of using the most detailed available model of an antenna's pattern obtained directly from measurements (preferably the full set of spherical wave coefficients) is that one knows the antenna patterns used are accurate. This removes one of the many uncertainties that exist when trying to model complicated real-world situations.

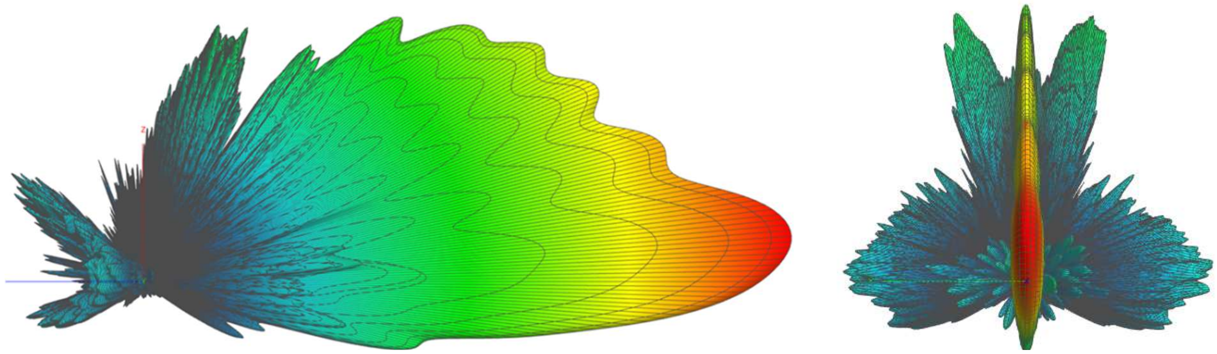

Figure 4.4 Cosecant radiation pattern reconstituted in FEKO from measured SNF data (for a naval E/F-band search radar) acquired on an NSI-MI Technologies spherical near-field range.

However, in some cases, this detailed measurement information may not be available or withheld by the equipment manufacturer. If a given antenna has some specially shaped radiation pattern, an equivalent planar source model can be provided through backprojection [82] [83] of SNF data onto a surface over which the equivalent-source is assumed to exist, even if the spherical wave coefficients are not made available. Figure 4.5(a) shows a reflector antenna under test in a SNF range, with the fictitious projected aperture. Figure 4.5(b) shows the backprojected electric field magnitude over the projected aperture.

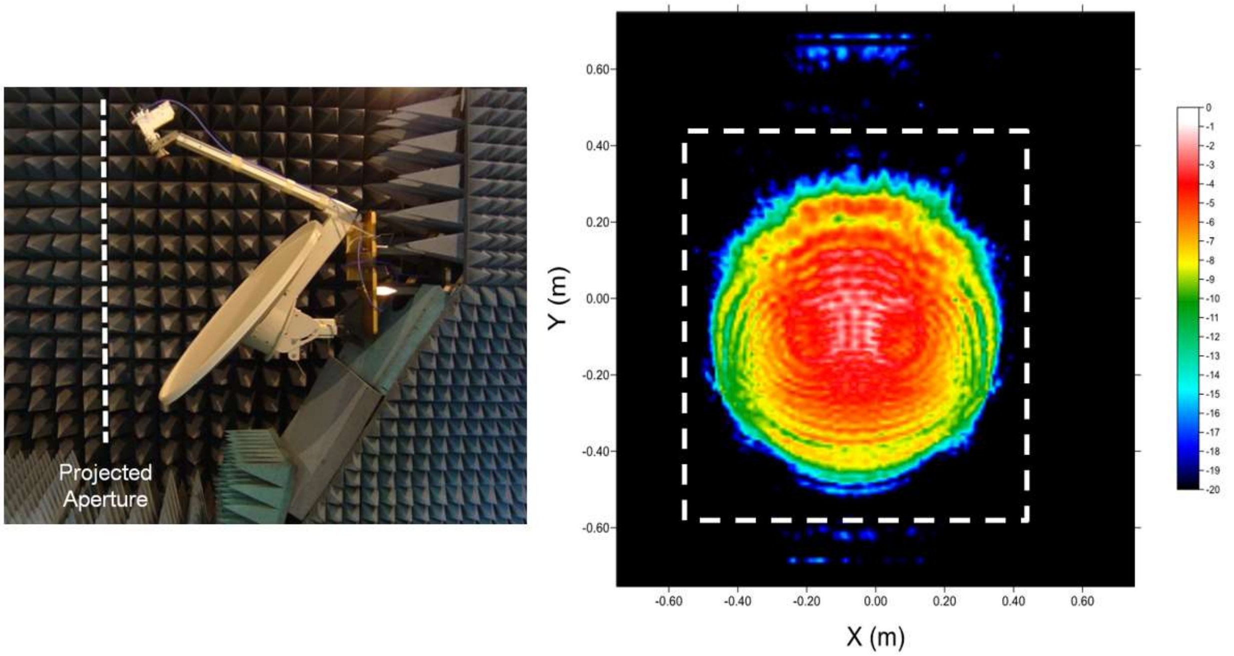

(a) (b)

Figure 4.5 (a) Offset-fed reflector showing the location of a projected aperture, and (b) the back-projected field magnitude distribution (from measured SNF data) over the projected aperture in (a).

Figure 4.6 is the radiation pattern, in the cut indicated, reconstructed by FEKO from the measured spherical wave coefficients (in blue), and from an equivalent planar source obtained by simply sampling the back-projected complex field data (in red). The equivalent planar source can provide the patterns in the field of view forward of the aperture only; it cannot supply this in the region of the back lobe, which the spherical wave coefficients could provide. The situation of a high directivity antenna being used in the detection of marine ice is illustrated in Figure 4.7, with the main lobe directed toward the ice object. Because the antenna and target are in each other's far zone, it turns out that backscatter intensities of the ice objects can be found just as well by assuming plane wave incidence instead of the detailed patterns of the antenna. Thus, although the above contribution to the on-platform-antenna modelling field was completed as part of this thesis, it was not actually required for the present work.

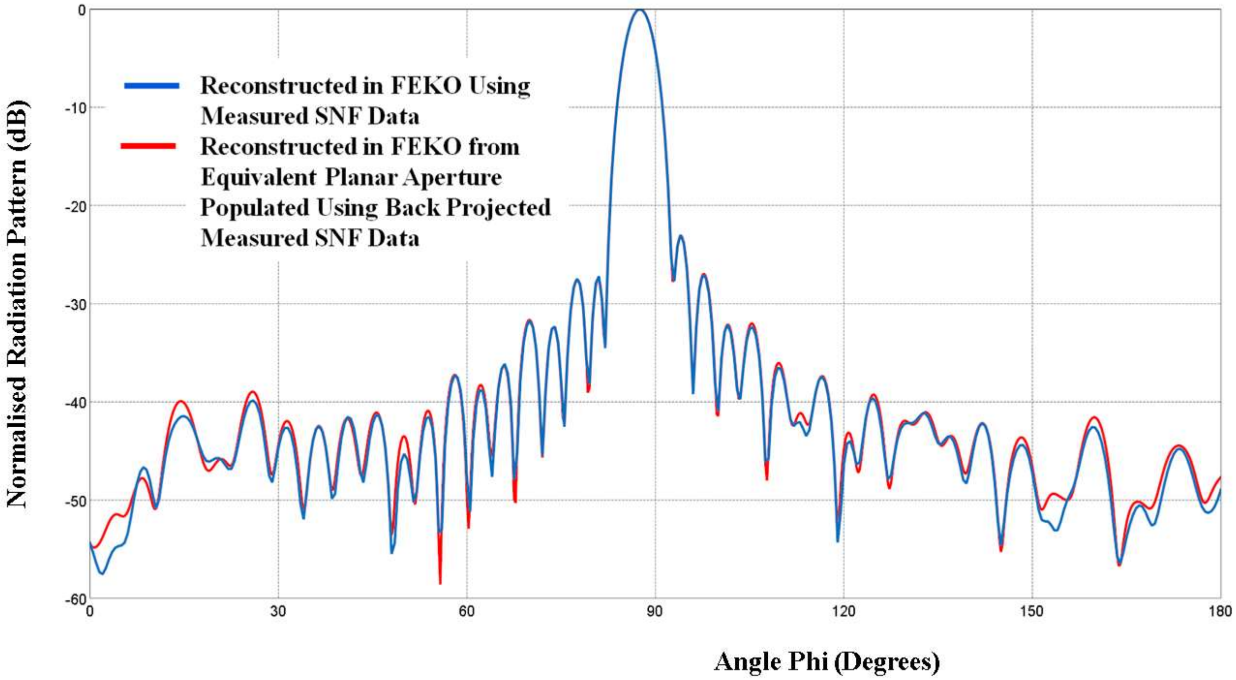

Figure 4.6 Main beam cut at θ=23.5° of the reconstituted radiation patterns produced using the SNF data directly (blue) and planar backprojected (red) at 13.75 GHz.

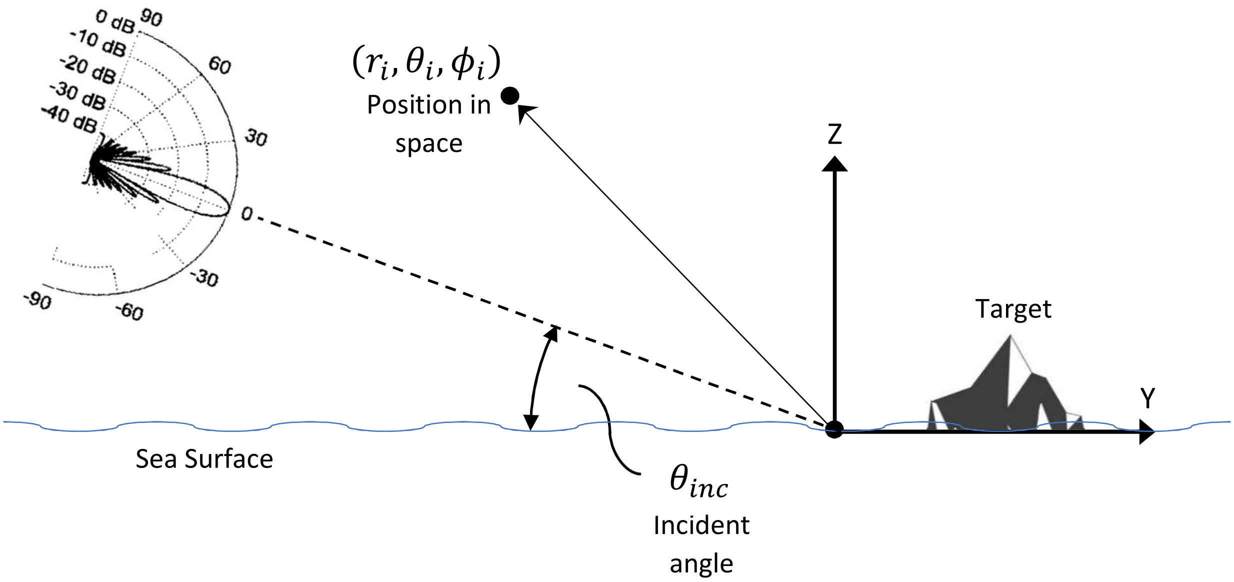

Figure 4.7 Diagram illustrating a radar beam incident on a surface target (iceberg) on a dielectric halfspace (sea surface).

4.8 Construction of Reliable Computational Electromagnetic Scattering Models

Normally, CEM modelling of the backscatter signature from electrically large objects would be done through asymptotic methods. However, these methods could not be used in this study for two reasons. First, one of the key quantities of measure was the cross-polarized backscatter intensity which could not be accurately determined by the asymptotic methods due to the lack of reciprocity in the approximation. Secondly, as discussed in Section 3.7, the seawater ground could not be ignored. Therefore, it was necessary to include a seawater halfspace in the models, which has not been implemented in FEKO for use with asymptotic methods. This meant that the only viable remaining method was the method of moments solution of the surface formulation of the Combined-Field Integral Equation - CFIE mentioned in Section 3.10.

The CFIE solution is computationally resource intensive for electrically large objects due to the significant number of unknowns (order O^3). It is therefore necessary to reduce the number of unknowns and the computational hardness of the equation as much as possible while maintaining sufficient confidence in the resulting computations. This was accomplished by:

a. Conducting convergence testing on a sample target to determine the minimum mesh size at which relatively accurate results are obtained;
b. Exploring the use of a Fresnel dielectric (seawater) or Perfect Electric Conductor halfspace as an alternative to a Sommerfeld halfspace; and
c. Observing the effects of scaling the model on the overall backscattered far-field pattern.

Section 4.7.3, 4.7.4 and 4.7.5, respectively, present the results of the convergence testing, halfspace analysis and scaling study.

Once an appropriate mesh level, halfspace representation and scaling factor were determined, the models were run for FYI, MYI and GI and validated against the experimental results from Haykin et al. [13], discussed in Section 3.11. The model validation and exploration of scattering from marine ice are presented in Chapter 5.

4.8.1 Quantity of Measure

As stated in Section 3.8, the measure of backscattering from ice objects used in this thesis will be the backscatter intensity, which is the magnitude of the term $\bar{F}_{scat}(\theta_i, \phi_i)$ in the far-field expression of the scattered field given by:

$$\bar{E}_{scat}(r_i, \theta_i, \phi_i) = \bar{F}_{scat}(\theta_i, \phi_i)\frac{e^{-jkr}}{r} \tag{4.6}$$

The quantity $20\log|\bar{F}_{scat}(\theta_i, \phi_i)|$ will be the backscatter intensity in decibel Volts (dBV).

The CEM software used in this thesis (FEKO) provides the option to present the results as electric field quantities in Volts (or dBV) or as radar cross-section quantities in square metres (or dBsm). However, the radar cross-section presentation will not be used, because it is the opinion of the author that, even when a halfspace (eg. sea surface) is present in the scattering model, FEKO is calculating this value using the incident plane wave field, as would be the case in free space as the incident field. This is supported by the fact that the radar cross-section values provided by FEKO are simply the backscatter intensity (which is used in this work) multiplied by the factor of 4π, which is correct for the free space radar cross-section situation. It is, therefore, neither the apparent radar cross-section, σ_{app}, nor the normalized radar cross-section, σ^0, from Section 3.8.

4.8.2 Method of Comparison

In section 4.7.3 and 4.7.4, a convergence study and a halfspace study will be conducted to determine an appropriate mesh level and halfspace representation that produce accurate results and minimize the computational resources required to solve the system of linear equations. Therefore, it is necessary to quantify the difference or uncertainty between two far-field radiation patterns using some objective and quantifiable method.

A common method used in antenna measurement [84] is to calculate the value of the difference at each sample point, $\Delta(\theta_i, \phi_j)$, by subtracting the normalized values of data set A from the normalized values of data set B in linear at each point, such that:

$$\Delta(\theta_i, \phi_j) = \left|\bar{F}^A_{norm}(\theta_i, \phi_j)\right| - \left|\bar{F}^B_{norm}(\theta_i, \phi_j)\right| \tag{4.7}$$

The difference is normally expressed and plotted in decibels, namely:

$$\Delta(\theta_i, \phi_j)\big|_{dB} = 20log\left|\Delta(\theta_i, \phi_j)\right| \tag{4.8}$$

The normalized values of data set A are given by:

$$\bar{F}^A_{norm}(\theta_i, \phi_j) = \frac{\bar{F}^A(\theta_i, \phi_j)}{|\bar{F}^A_{max}(\theta_0, \phi_0)|} \tag{4.9}$$

where $|\bar{F}^A_{max}(\theta_0, \phi_0)|$ is the absolute value of the maximum value of $\bar{F}^A(\theta_i, \phi_j)$, with (θ_0, ϕ_0) being the point at which the maximum occurs.

Similarly, when comparing the curves of the plot (eg. far-field pattern), regardless of the relative values of data set A and B, the normalized values of data set B are given by:

$$\bar{F}^B_{norm}(\theta_i, \phi_j) = \frac{\bar{F}^B(\theta_i, \phi_j)}{|\bar{F}^B_{max}(\theta_0, \phi_0)|} \tag{4.10}$$

When comparing the relative values at each sample point, the normalized values of data set B are given by[23]:

$$\bar{F}^{B}_{norm}(\theta_i,\phi_j)=\frac{\bar{F}^{B}(\theta_i,\phi_j)}{|\bar{F}^{A}_{max}(\theta_0,\phi_0)|} \tag{4.11}$$

If the believable dynamic range is 0 dB to some minimum detectable signal level (MDS, then before calculating the difference, $\Delta(\theta_i,\phi_j)$, the pattern values can be limited, such that:

$$\bar{F}_{norm}(\theta_i,\phi_j)=\begin{cases}\bar{F}_{norm}(\theta_i,\phi_j) & if\ 20log\left(\bar{F}_{norm}(\theta_i,\phi_j)\right)\geq MDS\\ 10^{MDS/20} & Otherwise\end{cases} \tag{4.12}$$

An estimate of the error, or uncertainty, between data sets A and B can be expressed as:

$$Uncertainty|_{dB}=20log\left(1\pm\Delta(\theta_i,\phi_j)\right) \tag{4.13}$$

or

$$Uncertainty|_{dB}=20log\left(1\pm 10^{\left(\frac{\Delta(\theta_i,\phi_j)|_{dB}}{20}\right)}\right) \tag{4.14}$$

Two values or patterns are generally considered to be the same, or have converged, when the difference value or the maximum difference between the two patterns is less than the believable dynamic range. In radio frequency receivers and systems, such as radars, this is referred to as the minimum detectable signal level (MDS). Two values or set of values (eg. backscatter patterns) are considered the same, or to have converged, when the difference or maximum difference value is less than the minimum detectable signal level or some other value. For this study, convergence will be considered to have occurred at -50 dB, which is associated with an uncertainty to be equal to 0.03 dB in the normalized backscatter pattern.

4.8.3 Convergence Study

The convergence study was conducted using a 10 GHz unit amplitude plane wave (1 V/m) incident at a 1° grazing angle (θ=89°). A MYI object, as shown in Figure 4.8, was placed directly on the Sommerfeld halfspace. The below water portion of the ice target was removed and the bottom face of the ice object was set to PEC. This was done to take advantage of image theory to simulate a below water portion, but was also required by the CEM software, which did not allow a dielectric material to be in contact with the halfspace.

This model contains all the features that would be expected in marine ice targets for this study: it contains flat angled faces, flat and curved sides, curved edges and a pinnacle-like top resembling a hummock, ridge or pinnacle found on FYI, MYI or GI. The ice target is approximately 0.5 m

---

[23] Carefully note the denominators in equations 4.10 and 4.11.

high and between 0.5 m and 1 m wide, depending the azimuth angle at which it is observed. The Sommerfeld halfspace was used as this is the most accurate representation for a dielectric halfspace. The model was meshed at three mesh levels: lambda/6, lambda/5 and lambda/4. The co-polarized and cross-polarized mono-static backscatter intensity was calculated at 181 points throughout the 360° of azimuth and the resulting patterns were compared, as described in Section 4.7.2, to determine convergence.

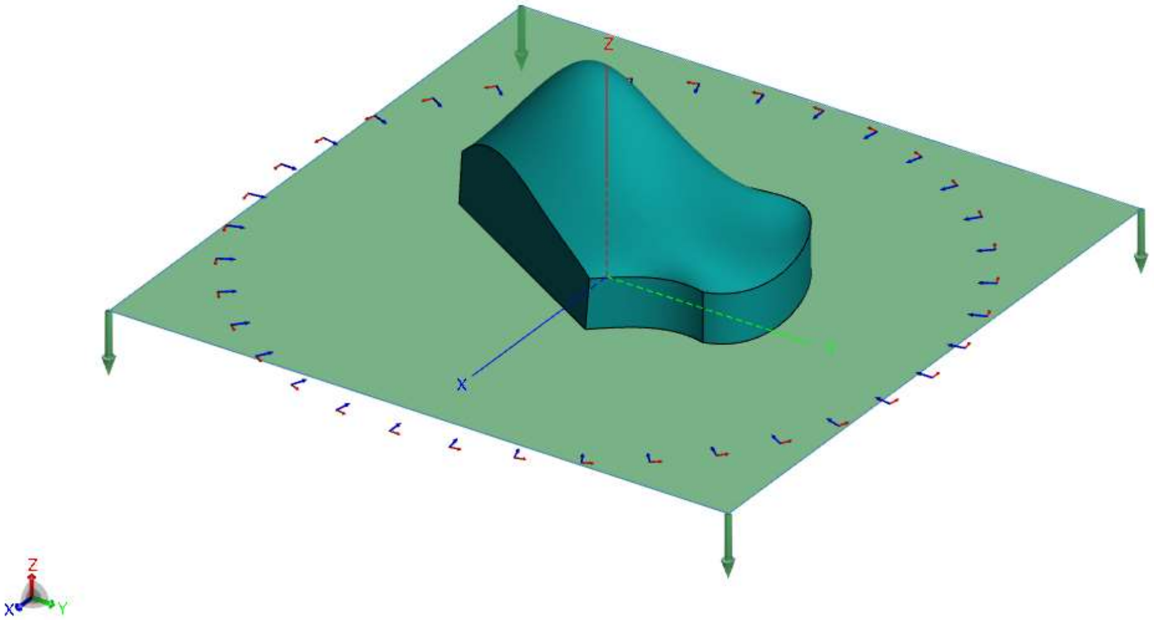

Figure 4.8 Marine ice target over a seawater sea used for model validation.

The results are shown in Figures 4.9 and 4.10 for the mono-static co-polarized and cross-polarized backscatter intensity respectively. The roughness of the graph should not be taken as inaccuracy; rather the graph should be viewed as a point by point comparison at 181 sample points (eg. azimuth angles).

As discussed in Section 4.7.2, two patterns are generally considered to have converged, when the difference is less than – 50 dB. Using equations 4.9 and 4.11, the difference between the sample values were calculated and plotted in Figure 4.11. As expected, as the mesh level increased, the mono-static backscatter patterns converge. Using -50 dB as the limit for convergence, it is evident that the solution has not converged at lambda/5. However, the maximum values of the difference between lambda/5 and lambda/6 for co-polarization and cross-polarization are -31.84 dB and -18.49 dB respectively. Using equation 4.14, this equates to an uncertainty of 0.23 dB for the co-polarization values and 1.10 dB for the cross-polarization values of the normalized backscatter intensity. In this work, the goal is to compare the co-polarized and cross-polarized backscatter intensity differences between FYI, MYI and GI such that they can be definitively classified. To do so, the pattern differences will need to be significant (eg. greater than 5 dB). Lambda/5 for the mesh level was used over lambda/6 to reduce the computational burden and run the models on the available server (eg. RAM). Therefore, an uncertainty of 0.23 dB for co-polarized and 1.10 dB for cross-polarized, normalized backscatter intensity was deemed acceptable: particularly given that as the frequency of test decreases, maintaining the mesh level of lambda/5 at 10 GHz causes the uncertainty in the calculations to decrease.

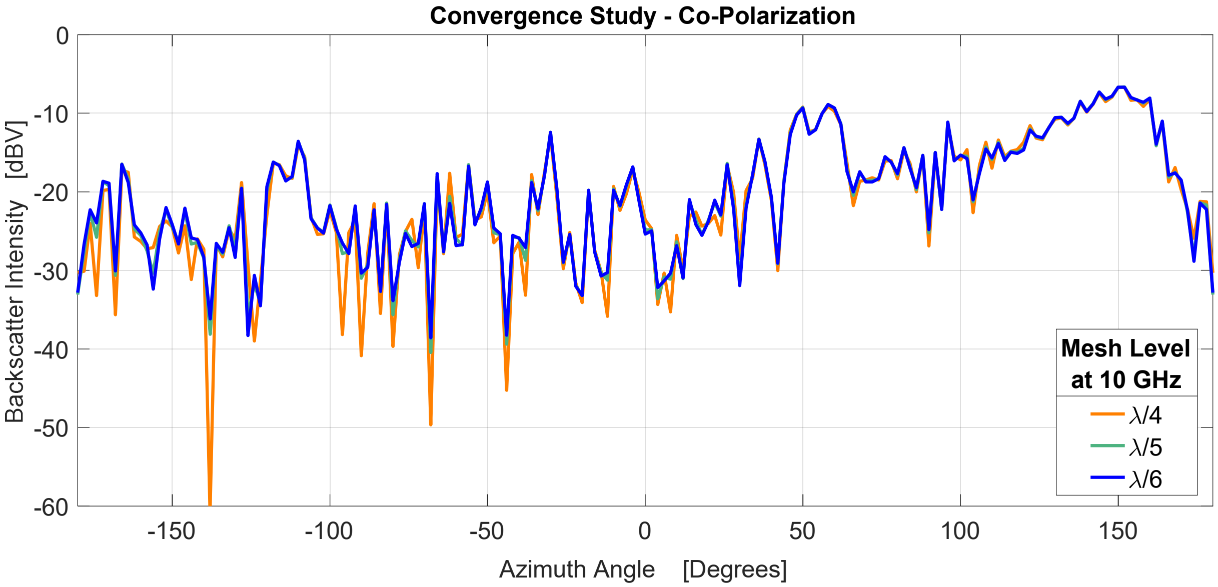

Figure 4.9 Convergence study results for the co-polarized backscatter intensity at 181 sample points.

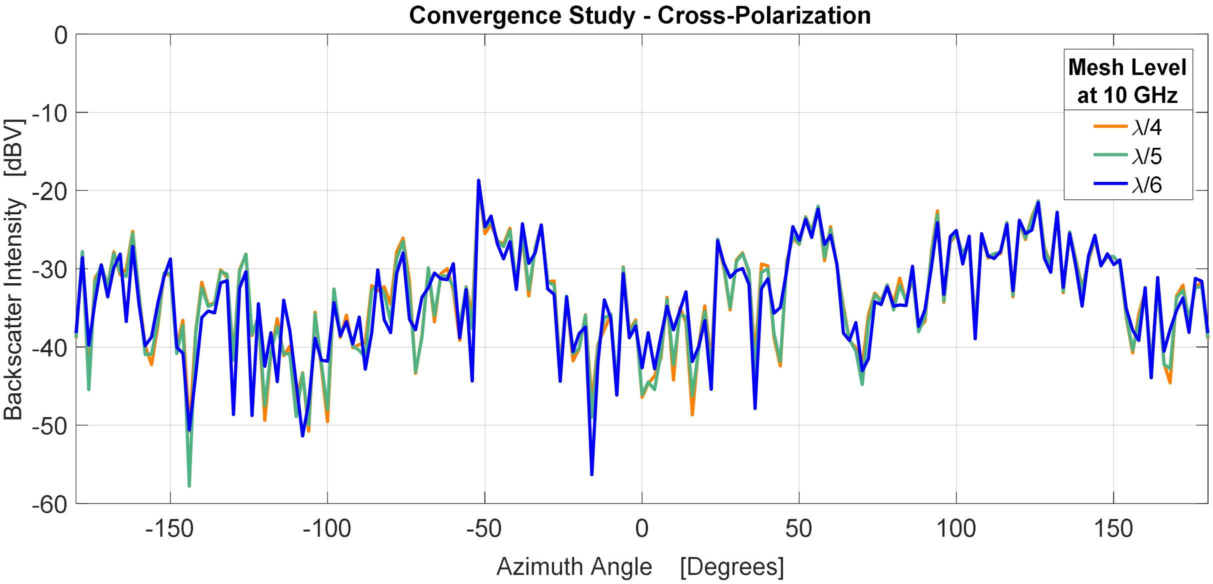

Figure 4.10 Convergence study results for the cross-polarized backscatter intensity at 181 sample points.

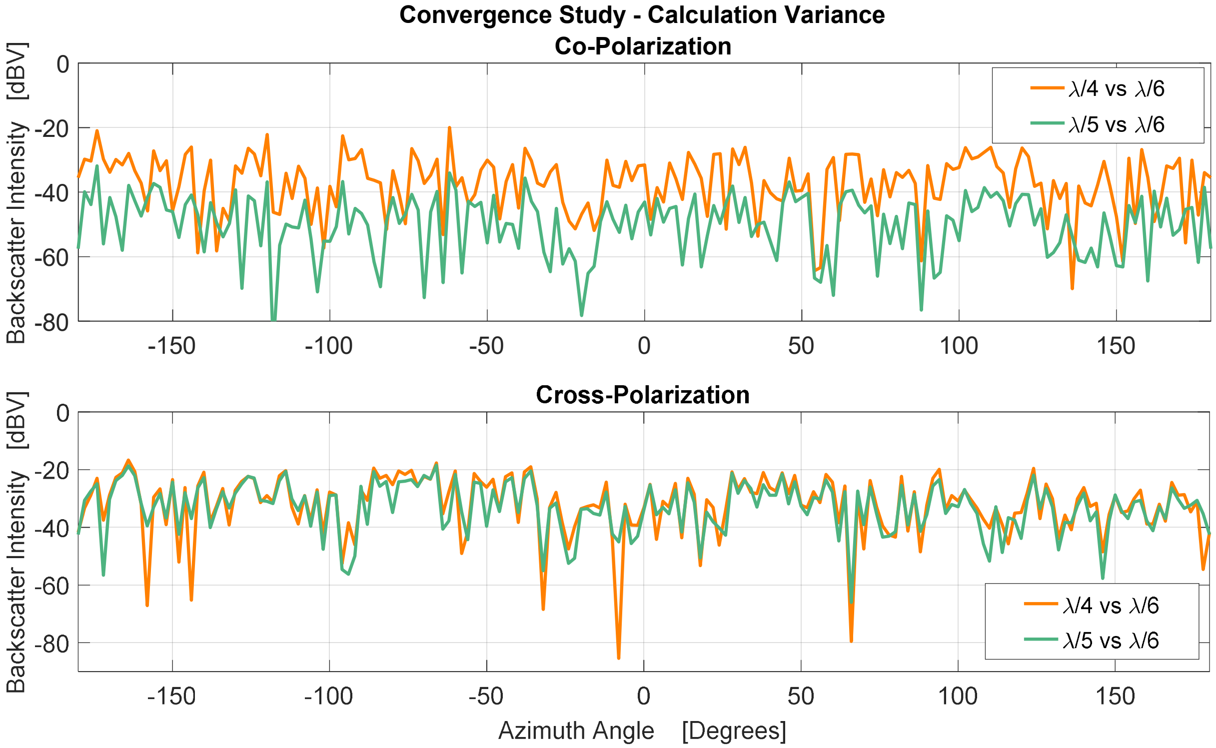

Figure 4.11 Convergence study results showing the difference between (top) co-polarized backscatter intensity patterns and (bottom) cross-polarized backscatter intensity patterns when meshed at lambda/4 and lambda/5 versus lambda/6.

4.8.4 Seawater Halfspace Study

During the literature review for this work, a paper by Baussard et al. [85] suggested that the RCS[24] of a surface target modelled on a Fresnel halfspace or even a PEC halfspace could be used in place of the Sommerfeld halfspace at low grazing angles (ie. high incident angles near 90°)[25]. Figure 4.8 compares the Physical Optics/Method of Equivalent Currents (PO/MEC) method of [85] for a rough and flat sea compared to a PEC flat sea modelled in FEKO (identified as FMP in the figure). In the work by Baussard et al., shown in Figure 4.12, the results for the PEC flat sea using FEKO and their PO/MEC model for the seawater sea (SEA) coincide between 85° and 90° for a horizontally polarized incident wave. For a vertically polarized incident wave, there appears to be less coincidence. Because of this paper, it was decided to conduct a seawater halfspace study to explore the possibility of using a Fresnel halfspace representation of the seawater sea, or a PEC

---

[24] The problems associated with defining the radar signature for a target on a sea surface were discussed in Section 3.8. Here the term radar cross-section (RCS) is used as this is the term used by the authors of [85]. It is unclear how the authors defined the quantity RCS shown in Figure 4.7.

[25] Such approximations have been used in antenna work [94] when only the far-zone fields, and not the near-fields needed for antenna input impedance, are required.

halfspace, as opposed to a Sommerfeld halfspace of seawater. In this work, these will be referred to as a Sommerfeld sea (SS), Fresnel sea (FS) and PEC sea (PS).

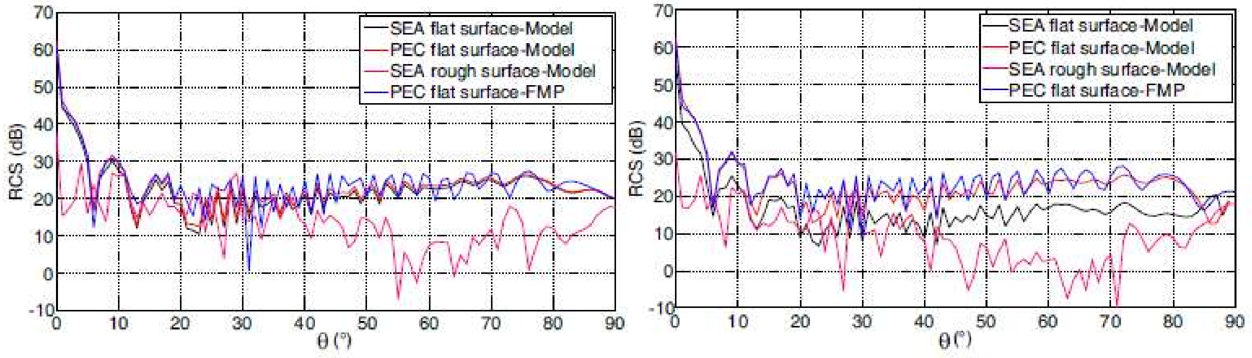

(a) (b)

Figure 4.12 Monostatic radar cross-section[4] of a PEC cube on a flat PEC surface, a flat sea surface and a rough (Sea state 3) surface for (a) the horizontally polarized and (b) the vertically polarized incident electric field. Nadir is θ = 0°. Figure courtesy of [85].

The Sommerfeld Green's function is the most accurate representation of a dielectric halfspace and was used as the baseline for the halfspace study. However, if the Fresnel or PEC halfspace representation can be used, it greatly reduces the computational complexity of the CFIE solution discussed in Section 3.10. The model meshed at lambda/6[26] in the convergence study was used for the seawater halfspace study and used for comparison with the Fresnel and PEC halfspace representations. Other than changing the halfspace representation, the only other modification was to place a lambda/12 air gap between the ice object and the halfspace in the Fresnel model. This was done to overcome a limitation with the implementation of this halfspace representation in FEKO, which would not allow a dielectric or PEC material to be in contact with the halfspace. The results are presented in Figures 4.13 and 4.14.

Using the equations presented in Section 4.8.2 to compare the results of the halfspace study, in the same manner as the convergence study in Section 4.7.8, the difference and uncertainty was calculated and plotted in Figure 11. Interestingly, the results for the co-polarized backscatter intensity using the PEC halfspace representation closely matches the Sommerfeld representation (see Figure 4.13) at a grazing angle of 1°, with a maximum uncertainty of 0.22 dB in the normalized backscatter intensity. However, the Fresnel representation is also a good approximation, with a maximum uncertainty of 1.07 dB. The results of the cross-polarized backscatter intensity show that the Fresnel representation is more accurate, with a maximum uncertainty of 2.88 dB, whereas the PEC representation has a maximum uncertainty of 19.27 dB.

---

[26] The decision to use a mesh level of lambda/5 in the engineering models was made after the halfspace study, in order to reduce the computational requirement of the models, while maintaining sufficient accuracy to conduct that analysis of the backscatter signatures. "Perfect is the enemy of good enough" - Voltaire 1770

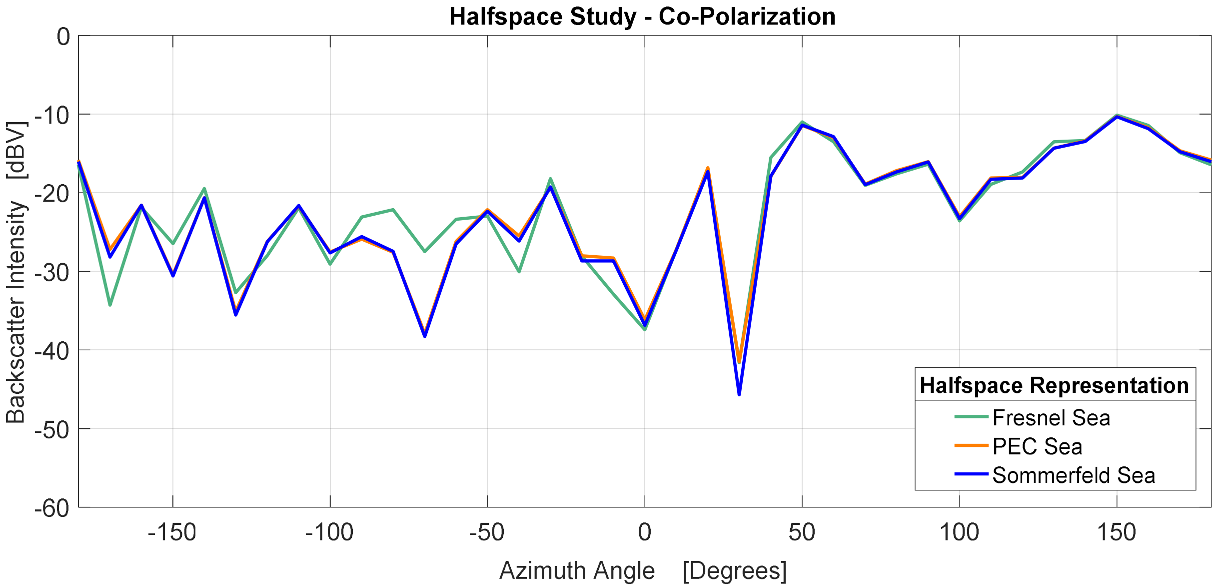

Figure 4.13 Comparison of the co-polarized mono-static backscatter intensity for the Sommerfeld and Fresnel seawater halfspace, and the PEC halfspace over 37 azimuth samples, excited by a 1° incident angle plane wave.

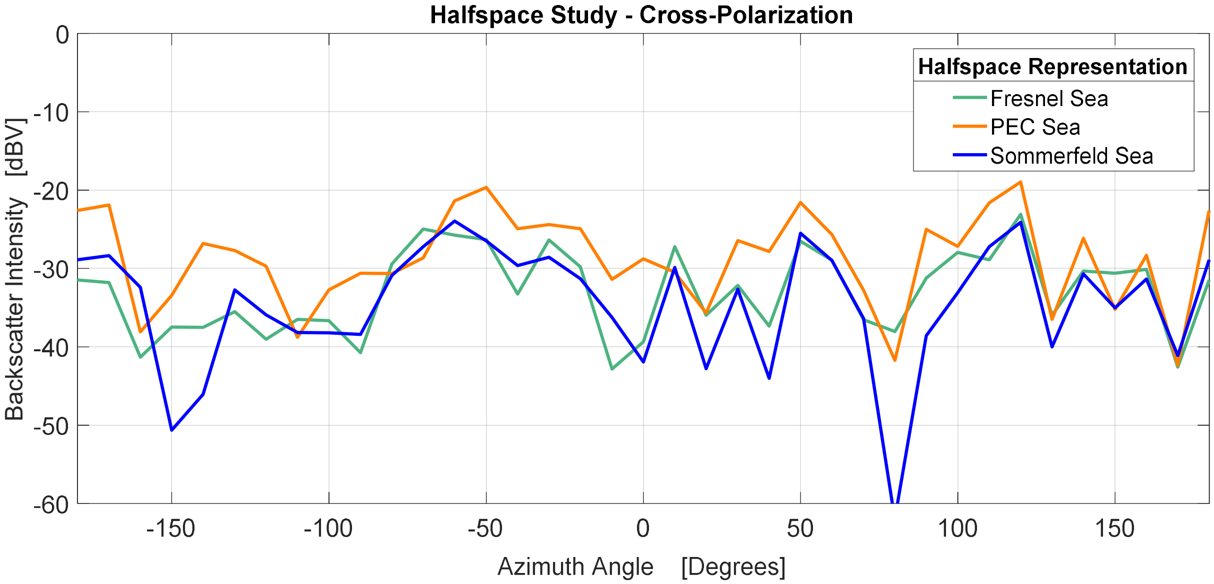

Figure 4.14 Comparison of the cross-polarized mono-static backscatter intensity for the Sommerfeld and Fresnel seawater halfspace, and the PEC halfspace over 37 azimuth samples, excited by a 1° incident angle plane wave.

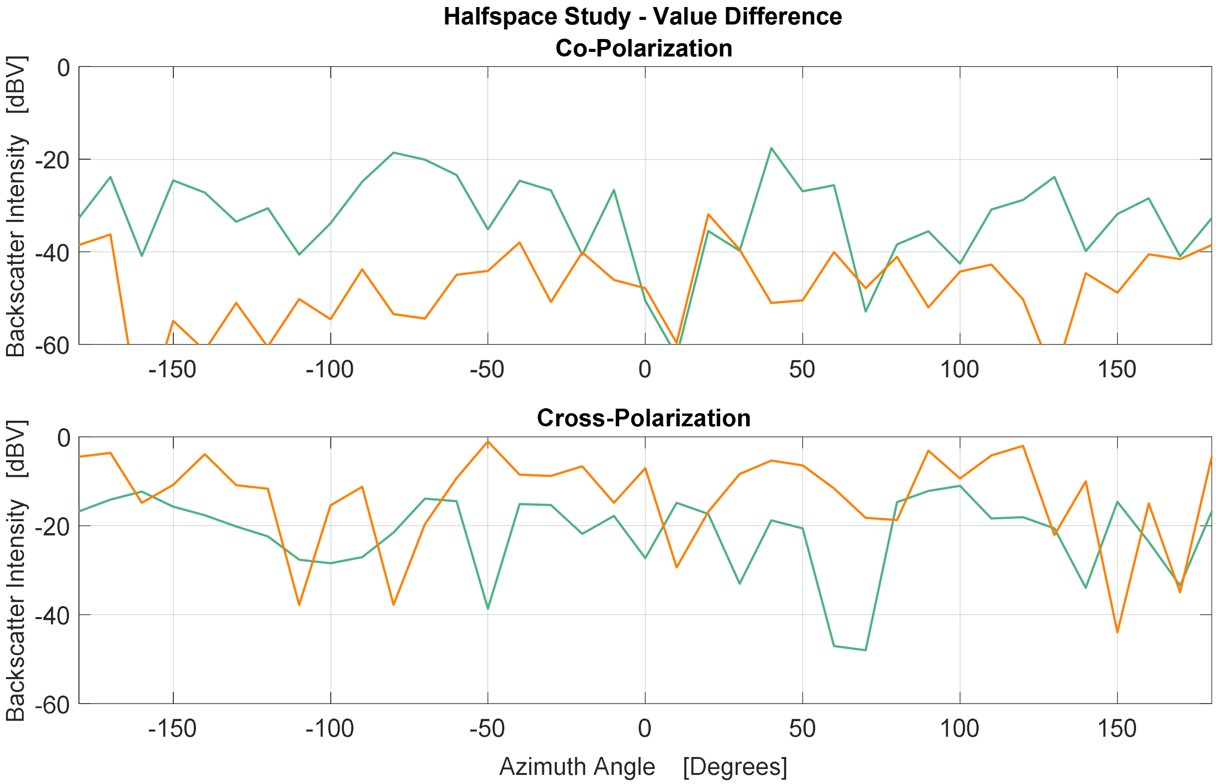

Figure 4.15 Halfspace study results showing the difference between (top) co-polarized backscatter intensity patterns and (bottom) cross-polarized backscatter intensity patterns for the PEC representation (orange) and the Fresnel representation (green).

Therefore, if one was only interested in the co-polarized backscatter intensity, as would be the case for most surface-based radars (ie. transmit and receive in one polarization only), then the PEC halfspace representation could be used with a high degree of confidence (0.22 dB uncertainty) in the results. Overall though, the Fresnel halfspace provides the next best representation to the Sommerfeld representation, with a co-polarization uncertainty of 1.07 dB and a cross-polarization uncertainty of 2.88 dB.

Ideally, one would use the Sommerfeld halfspace representation as this is generally accepted as the most accurate representation. However, there are significant differences in the computational resources required for each halfspace. Figure 4.16 shows that although there is only a slight reduction in memory requirements between a Sommerfeld sea and a Fresnel sea, there is a significant (72%) savings in CPU hours between the Sommerfeld sea and the Fresnel sea.

Although the Fresnel sea representation diverges from the Sommerfeld sea for the cross-polarization results, it will be used in this work because of the significant savings in CPU hours (computation time). The models in this work are electrically large and therefore any method that reduces computational time and memory resources must be exploited.

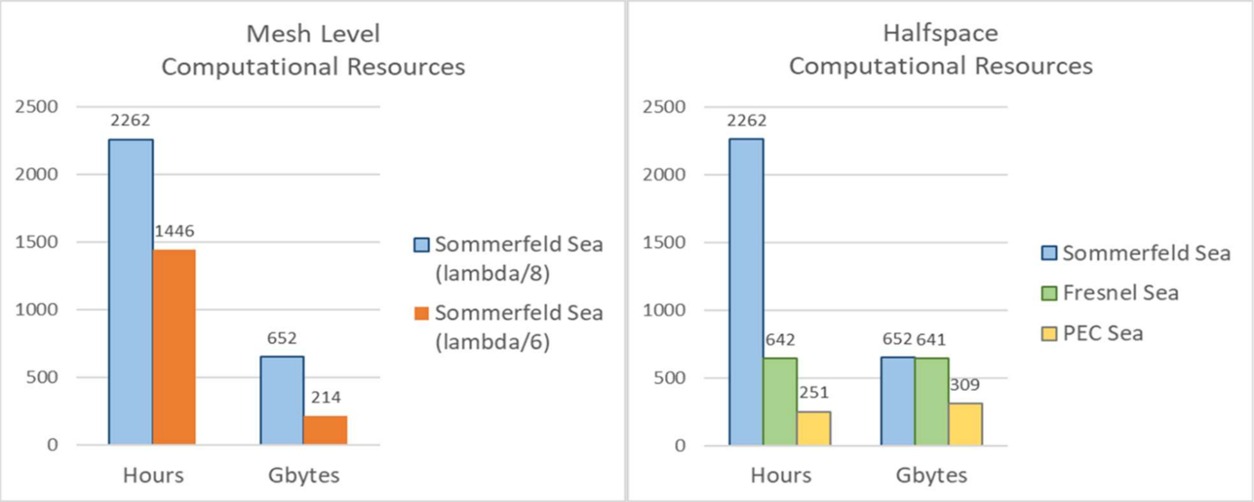

Figure 4.16 Left: Comparison of computational resources by mesh level. Right: Comparison of computational resources by halfspace representation of the seawater sea.

4.8.5 Scaling Study

Due to the electrically large nature of the marine ice targets and the computational resources (CPU time) to solve the resulting set of linear equations, it was decided to conduct a scaling study to see if conclusions could be drawn about larger targets from scaled models of the targets. The theory being that as the size of the target increases, the relative contribution of the individual scatterers will remain the same and the backscatter signature would have a similar normalized backscatter intensity pattern.

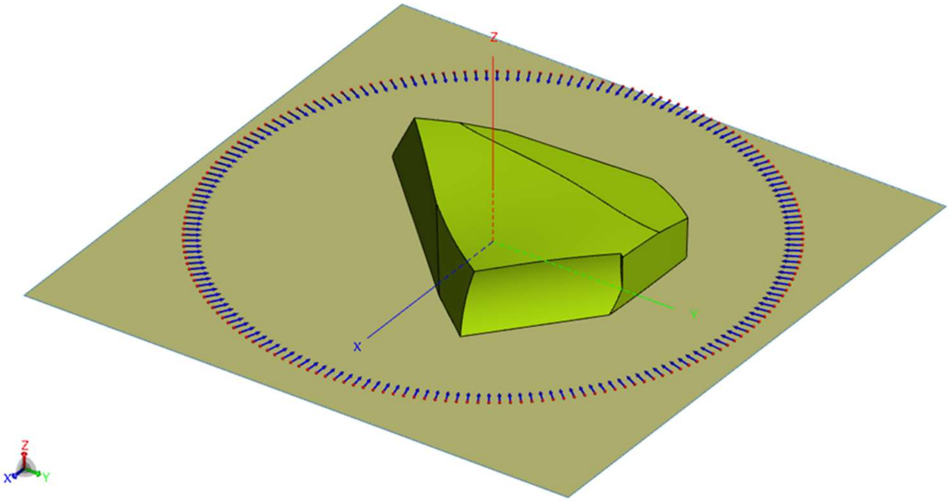

Figure 4.17 Tabular FYI object used in the scaling study. The full scale object is approximately 0.2m high by 1.5m wide.

To test this theory, the models of the FYI, MYI and GI were scaled by a factor of 0.1, 0.2, 0.4 and 0.75. The maximum scaling factor of 0.75 was selected based on the memory capacity of the available server (1 TB of RAM and 96 CPUs). Once the available RAM is exceeded, the solution must be read/written to the hard drive adversely impacting the computational time. Table 4.5 provides an example of the memory and CPU time required as the target is scaled up in size while maintaining the lambda/5 meshing.

Table 4.5 Example of the computational resources required for the method of moments solution of the tabular ice target model.

Scale	0.1	0.2	0.4	0.75
Memory (RAM)	0.994 GB	15.6 GB	252.6 GB	932.9 GB
CPU Time	0.354 hrs	6.6 hrs	283.5 hrs	1521.6 hrs

The scaling study was conducted using a 10 GHz unit amplitude plane wave (1 V/m) incident at a 1° grazing angle (θ=89°). A tabular FYI target, as shown in Figure 4.13, was placed at a distance of lambda/12 above a Fresnel halfspace of seawater. This ice object was chosen for the scaling study and the main results presented in Chapter 5 because it is possible to find FYI, MYI and GI targets with this shape. The results of the scaling study are presented in Figures 4.18 through 4.20.

At a scaling level of 0.1, the target is roughly 2 cm high by 15 cm wide. At 10 GHz the wavelength is 3 cm, which means the target is less than one wavelength high by approximately 5 wavelengths wide. By comparison of the co-polarized backscatter intensity in Figure 4.18, at a scaling factor of 0.1, the effects of the individual scatters of the object are not easily observable. As the target is scaled up to 0.4 and subsequently 0.75, peaks associated with individual scatterers (flat or curved faces) of the target become evident. In fact, as evident in plot to the right in Figure 4.18, scaling up from 0.4 to 0.75 does not significantly change the far-field pattern. Comparing the results in Figure 4.19 shows that the cross-polarized backscatter intensity shows the same convergence. As the size of the object and the individual scatterers increases, the cross-polarized return of the FYI target decreases and although not exact, produces similar intensity measurements. Finally, comparing the co-polarized and cross-polarized backscatter intensity yields similar results for both the 0.4 scaling factor and the 0.75 scaling factor. The target at the 0.4 scaling factor is approximately 8 cm high and 60 cm wide, with the flat faces on this target being approximately 30 cm wide. At the 0.75 scaling factor, the target is approximately 15 cm high by 112.5 cm wide, with the flat faces being approximately 50-60 cm wide. Therefore, it appears that a scaling factor of 0.4 is sufficiently large for this target to draw conclusions about the response of larger targets. The deciding factor being whether the individual scatterers are at least one wavelength by one wavelength in size.

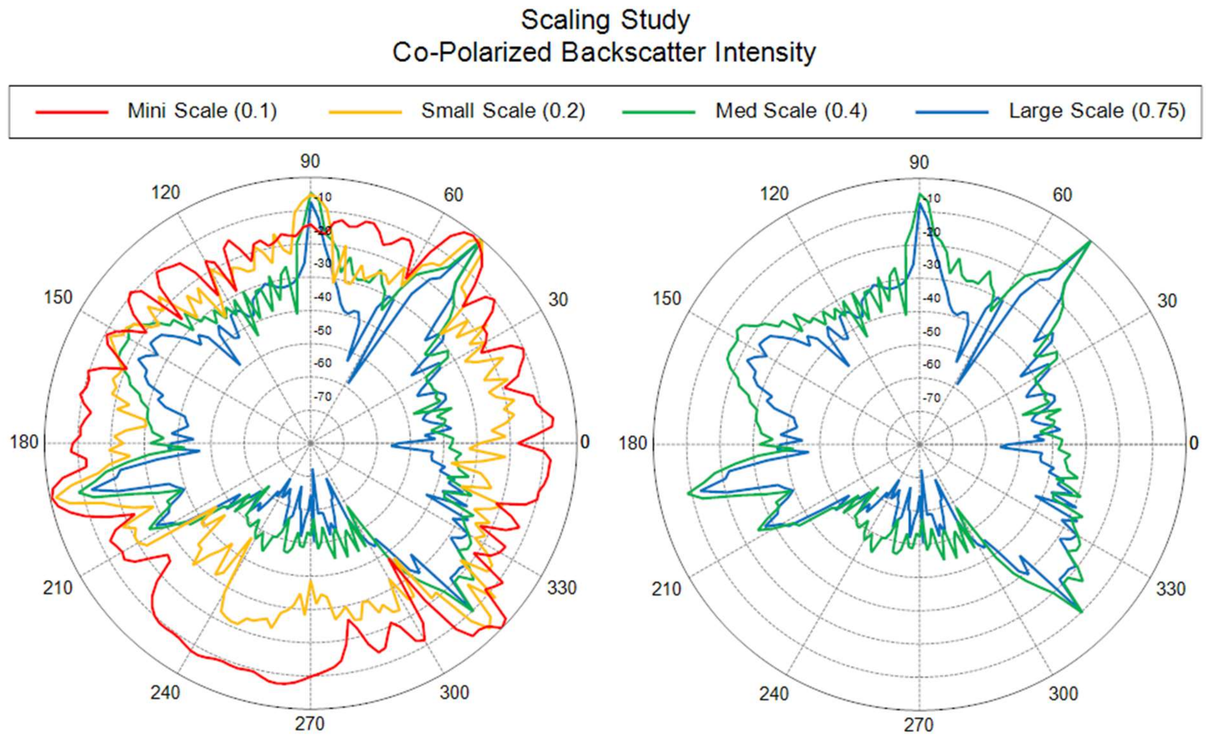

Figure 4.18 Normalized co-polarized backscatter intensity of a 0.2m high by 1.5m wide FYI target at various scaling levels. Left: Results for all (4) scaling levels. Right: 0.4 and 0.75 scaling level only.

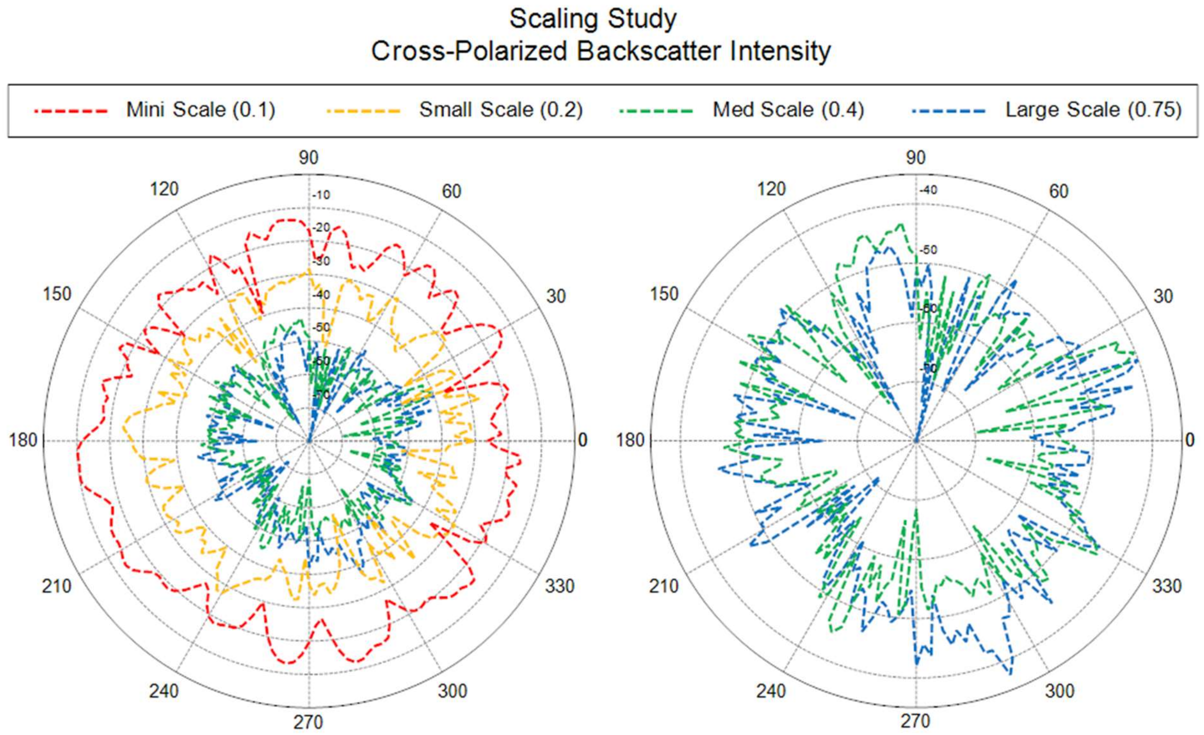

Figure 4.19 Normalized cross-polarized backscatter intensity of a 0.2m high by 1.5m wide FYI target at various scaling levels. Left: Results for all (4) scaling levels. Right: 0.4 and 0.75 scaling level

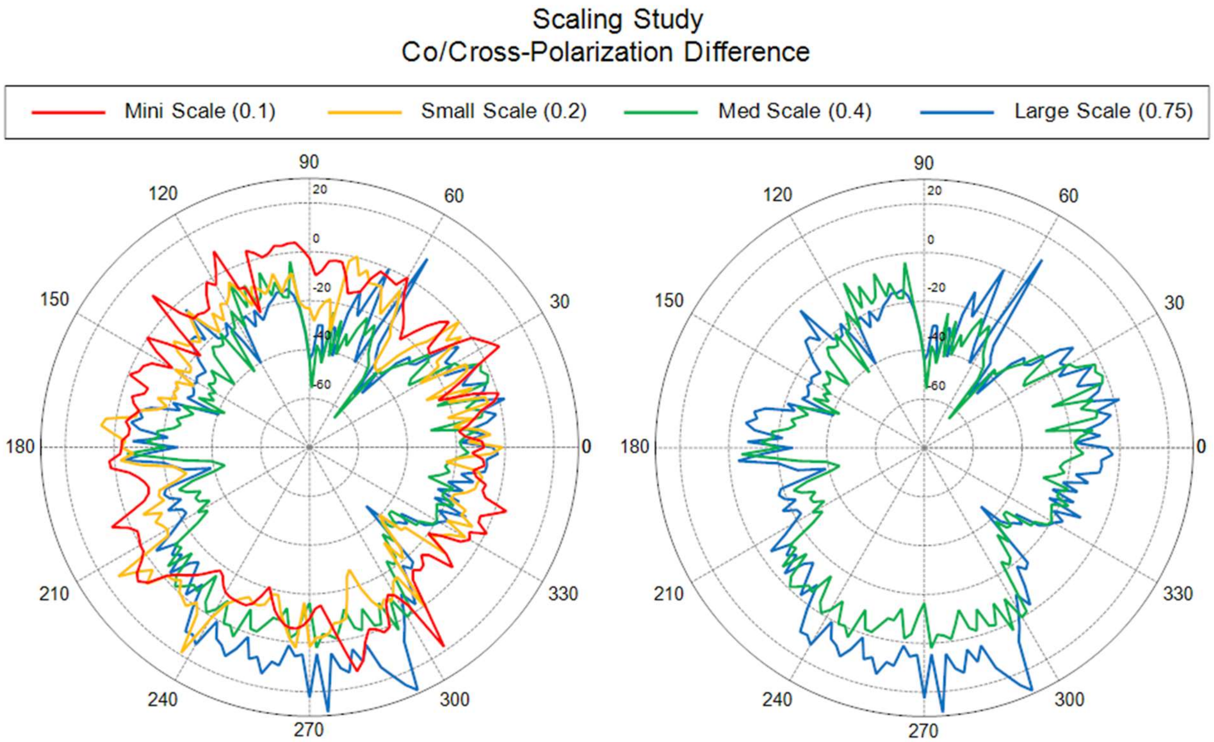

Figure 4.20 Polarization difference between the cross-polarized backscatter intensity and the co-polarized backscatter intensity of a 0.2m high by 1.5m wide FYI target at various scaling levels. Left: Results for all (4) scaling levels. Right: 0.4 and 0.75 scaling level only.

4.9 Conclusions

The goal of the present work is to determine the feasibility of using computational electromagnetics to improve our understanding of backscattering from the three marine ice types of interest to Arctic navigation (safe FYI, and hazardous MYI and GI). In principle this can always be done, if unlimited computational power is available. The issue is whether it is feasible with excellent but "reasonable" computer resources.

Three useful pieces of information have been determined in this chapter using computational experimentation (i.e. the convergence study, comparison of three half-space analysis method selections, and the scaling study) [27]. It has been determined that, for reliable backscatter intensity computations up to 10GHz:

a. A mesh level of a fifth of a wavelength ($\lambda/5$) is sufficient; and
b. The seawater ground plane can be adequately represented using the Fresnel reflection coefficient halfspace representation.

---

[27] As stated earlier, the highest frequency at which computational electromagnetics modelling is done here is 10 GHz. Convergence studies have been performed at this frequency.

If we are principally interested in the relative trends of the co- and cross-polarized backscatter intensity computations, then:

c. The actual ice target size can be scaled by a factor of 0.4 or greater, without affecting the co- and cross-polarized backscatter intensity relative intensity; the limiting factor appears to be that the reduced target's smallest characteristic dimension must be greater than one wavelength.

With these "modelling rules" that have been determined, there is a combined uncertainty of only 1.3 dB and 4.0 dB in the co-polarized and cross-polarized normalized backscatter intensity, respectively. This must be considered when comparing the model results for FYI, MYI and GI. This uncertainty is a maximum at 10 GHz and decreases as the frequency decreases.

Using a mesh level of $\lambda/5$ reduces both the memory required to store the moment method matrices and the computational time to solve the PMCHWT matrix equation for electrically large targets. The computational time is similarly reduced if the Fresnel halfspace approach can be used. Despite this, the mono-static backscatter intensity of an ice target cannot be easily computed without significant computational resources.

Chapter 5 will use the modelling rules established in this chapter to perform a case study of scattering from an ice object.

5. Case Study & Validation

5.1 Introduction

This chapter is organized into the following sections:

Section 5.2 –Backscatter from Marine Ice from 6 to 10 GHz;

Section 5.3 – Surface and Volume Scattering Phenomena at 10 GHz;

Section 5.4 – Effects of Small Target Movements;

Section 5.5 – Validation of the Engineering Models; and

Section 5.6 – Conclusions.

Now that the methodology for electromagnetic modelling of marine ice objects has been established in Section 4.8, it is necessary to validate the engineering models by showing they represent real-world marine ice targets and produce real world backscatter signatures[28]. This chapter will present the modelled results for backscatter from marine ice targets from 6 to 10 GHz and compare these results to the experimental data referred to in Section 3.11. In the end, the feasibility of using computational electromagnetics to model marine ice will be demonstrated, and it will be shown that an optimum frequency appears to exist above 10 GHz which will enable reliable classification of marine ice using a dual-polarization radar.

Sections 5.2 will present the results of the case study of backscatter from marine ice and Section 5.3 will interpret these in terms of the surface- and volume-scattering phenomena, mentioned in Section 3.9. Section 5.4 will explore the effects of small target movements, of the kind expected from an ice object floating on a wavy sea, on the backscatter from marine ice. And finally, Section 5.5 will compare the modelled results to the existing experimental results, as a validation of the engineering model methodology.

Section 5.6 concludes the chapter and summarizes the key findings of this case study and validation.

---

[28] The backscatter signature is a combination of the co-polarized and cross-polarized backscatter intensity and the degree of depolarization of the backscattered field.

For the validation of the engineering models and the case study of backscatter from marine ice presented here, the tabular ice object, as shown in Figure 5.1, will be modelled as detailed in Section 4.8.5. The full-scale object (approximately 0.2m high by 1.5m wide) has been scaled by a factor of 0.75. All models will be meshed at lambda/5 with lambda equal to the wavelength associated with 10 GHz (the maximum frequency of study), regardless of the frequency of test. The effective permittivity of the ice targets and seawater used in this study are presented in Tables 4.3 and 4.4.

The following colour scheme will be used for all plotted results:

Green – First-year ice (FYI). FYI is also referred to as "safe" ice.

Amber – Multi-year ice (MYI)

Red – Glacier ice (GI)

MYI and GI are also referred to as "hazardous" ice.

Any departures from this format will be noted in the discussion and figures.

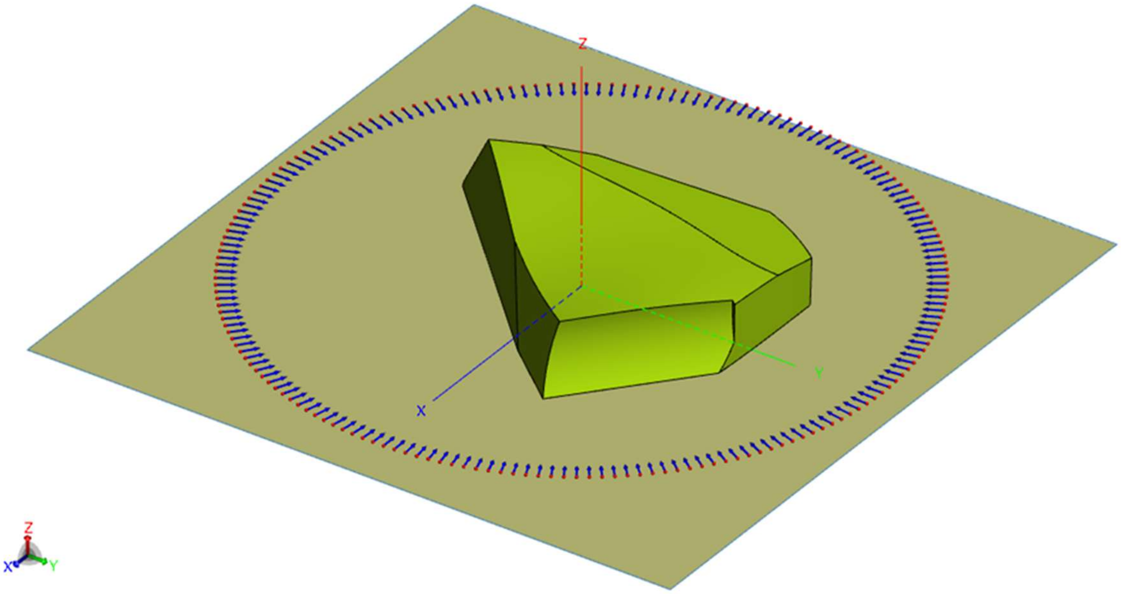

Figure 5.1 Tabular ice object used in the study of backscattering from marine ice.

All results from the backscatter study will be presented as the mono-static backscatter intensity $\bar{F}_{scat}(\theta_i, \phi_i)$ expressed in dBV. This was deemed to be the best quantity of measure, as explained in Section 4.8.1, and is especially so because the method of ice classification being explored only needs to know the relative difference between the co-polarized and cross-polarized backscatter intensity of the marine ice types. If the backscatter intensity were to be converted to σ_{app} or σ^0 the difference between the co-polarized and cross-polarized values would be the same as the difference between the co-polarized and cross-polarized backscatter intensity values.

The term "backscatter signature" will be used here to denote the combination of the co-polarized and cross-polarized backscatter intensity and the degree of depolarization of the backscattered field. Depolarization was defined in Section 3.10 as the ratio of the cross-polarized backscatter intensity over the co-polarized backscatter intensity, such that:

$$Depolarization = \bar{F}_{scat}^{cross}(\theta_i, \phi_i)|_{dB} - \bar{F}_{scat}^{co}(\theta_i, \phi_i)|_{dB}$$

The backscatter intensity will be presented using three methods: a single value average of the backscatter intensity from all sample points, polar plots of the mono-static far-field intensity pattern, and histograms of the backscatter intensity probability density distributions. In remote sensing, it is common to average the measured backscattered field quantities (eg. backscatter intensity or apparent RCS) for a given frequency, incident angle and polarization [69]. From time to time, the average backscatter intensity will be presented in the results, but it should be noted that this is an over-simplification that does not adequately describe the range (or distribution) of backscatter intensity values from real world marine ice targets and would not highlight the overlap in the range of values between marine ice types. Therefore, histograms will be used to show the probability density distribution of the backscatter intensity (eg. return signal strength) of each marine ice type. These diagrams will highlight the overlap in the backscatter intensity between FYI, MYI and GI that can lead to mis-classification of the marine ice type. The histograms were produced by extracting the magnitude of the backscatter intensity, $\bar{F}_{scat}(\theta_i, \phi_i)$, at each sample angle[29] and calculating the probability of the backscatter intensity falling within a defined range of intensity values (or bins)[30]. All histograms uses bin size of 3 dB. Much of the discussion in this section will centre around the interpretation and comparison of the histogram; however, the polar plots will be included as they provide another view of the data which aids in the interpretation and analysis of the data and the overall trends.

The benefit of using CEM numerical modelling to conduct backscatter studies is that the number of variables that change can be controlled. In the real world, to find identical objects, under identical environmental conditions, made of three different types of marine ice is statistically impossible. As a result, experimental data is collected from a variety of ice objects, over a number of days or even years and averaged or examined as probability distribution curves (eg. histograms). Therefore, attributing effects to a particular variable is difficult. Using CEM modelling, the mono-static backscatter intensity at 181 different azimuth angles around a single ice object, as was done in this study, can be calculated in hours[31]. The same ice object can be set to any marine ice type under identical environmental conditions and compared, as was done in this study. Conversely, for the same ice type, the ice object, its physical or electrical properties or the environmental conditions (eg. permittivity, temperature, salinity, etc) can be changed individually to observe the impact on the backscatter signature.

---

[29] FEKO provides an option to export the field data into .dat files that can be converted to .xlsx files in Excel, which can then be easily imported into Matlab and manipulated.

[30] The histograms were produced in Matlab using the histogram() function call.

[31] The largest ice models used in this case study took 15-18 hours using 96 CPUs and 1 TB of RAM.

5.2 Backscatter from marine ice from 6 to 10 GHz

The long-term goal, of which this work forms a part of, is to determine if there is a frequency or range of frequencies at which marine ice can be definitively classified as FYI, MYI or GI (or, at the very least, as safe ice or hazardous ice). This section will explore and discuss the ability to classify marine ice at an operating frequency from 6 to 10 GHz. In Section 5.5, the results from these models will be compared with the experimental results from Haykin et al. [13] as a final validation of the engineering models.

There are noticeable differences in the backscatter signatures of FYI, MYI and GI, which are immediately evident in the polar plots of the backscatter intensity (Figure 5.2 through 5.4):

a. FYI has a distinctly different co-polarized backscatter pattern than MYI and GI;
b. FYI has areas where it has the weakest backscatter intensity but also "spikes" of strong backscatter intensity in five (5) regions that make it indistinguishable from MYI and GI;
c. As the frequency increases, the cross-polarized backscatter intensity of FYI decreases;
d. MYI and GI have similar mono-static co-polarized and cross-polarized backscatter patterns;
e. GI has the strongest backscatter intensity, followed closely by MYI; and
f. GI has the strongest cross-polarized backscatter intensity, followed closely by MYI and then FYI.

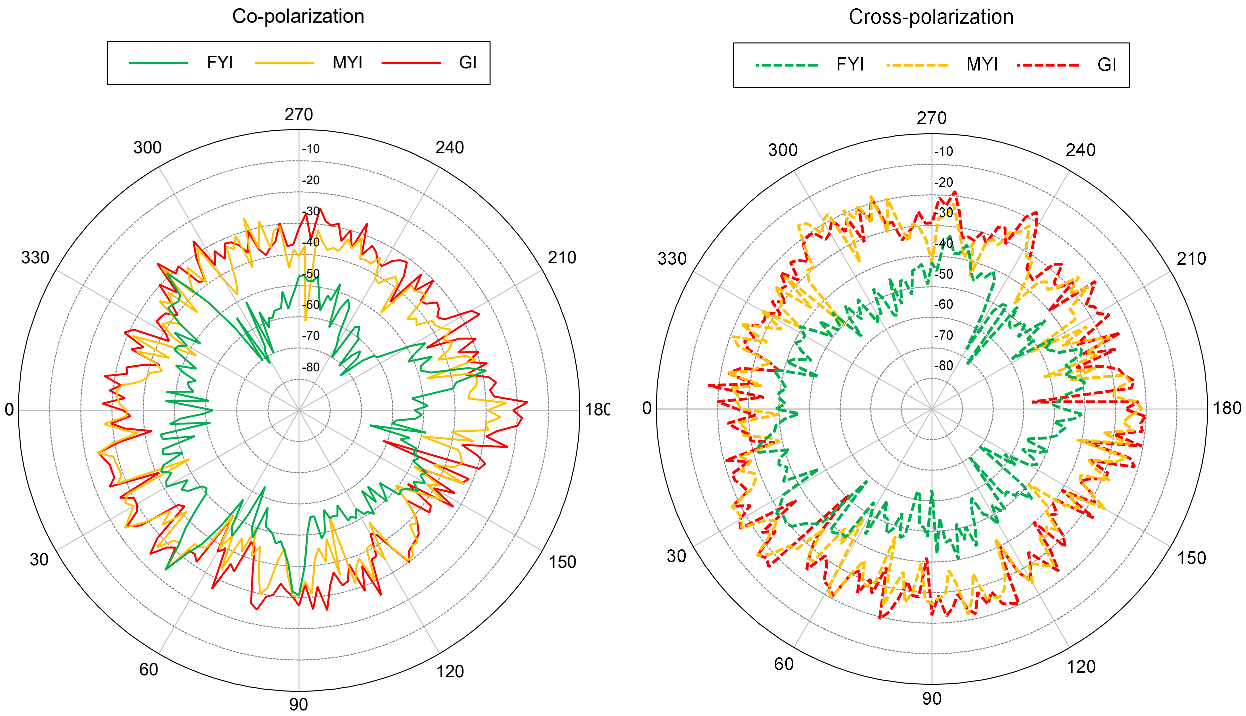

Figure 5.2 Polar plots of the mono-static backscatter intensity from marine ice at 6 GHz. Left: Co-polarized backscatter intensity. Right: Cross-polarized backscatter intensity.

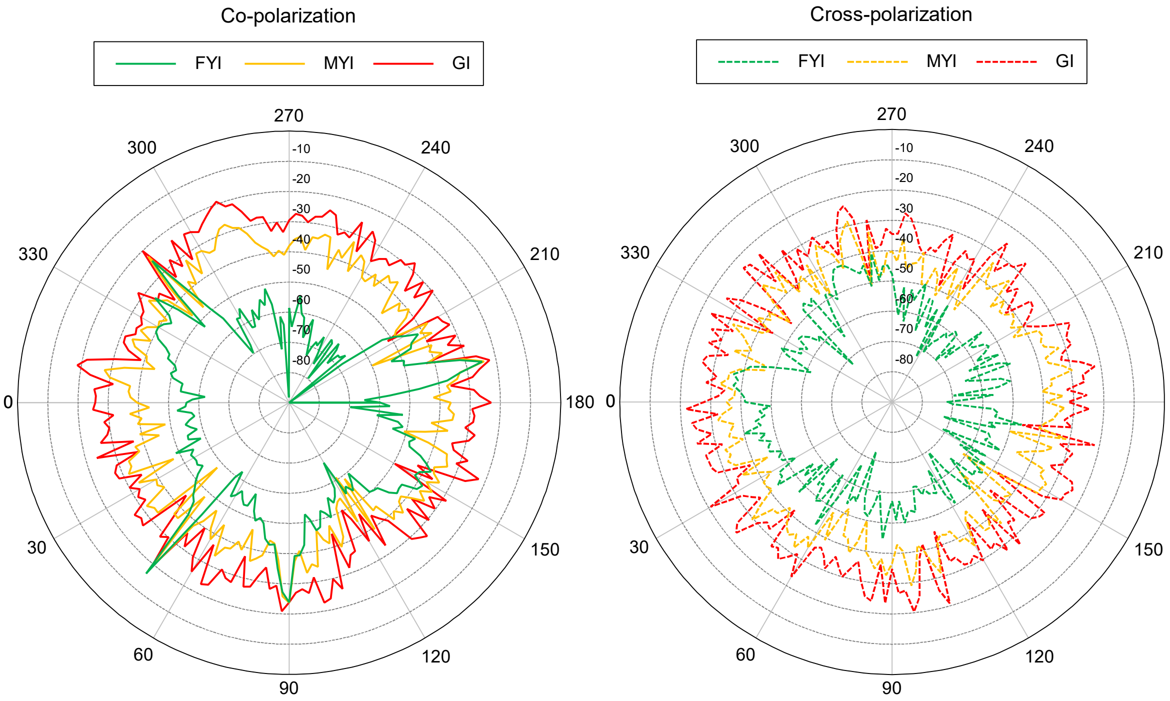

Figure 5.3 Polar plots of the mono-static backscatter intensity from marine ice at 8 GHz. Left: Co-polarized backscatter intensity. Right: Cross-polarized backscatter intensity.

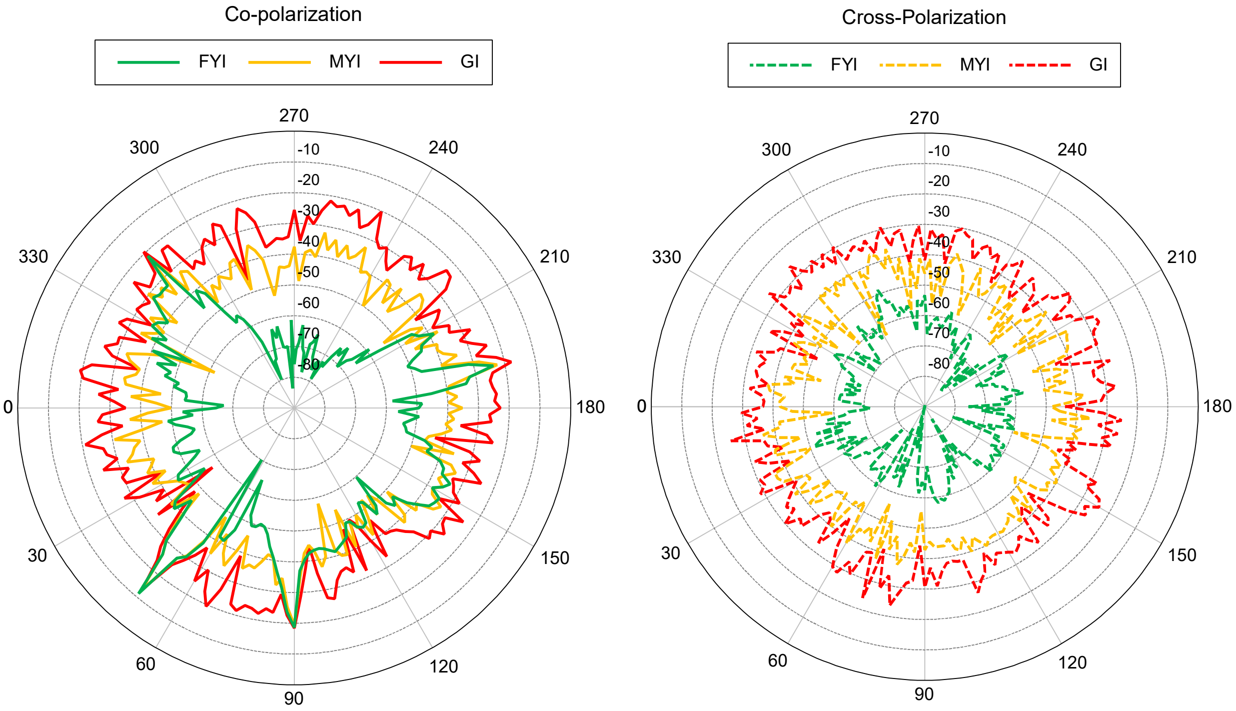

Figure 5.4 Polar plots of the mono-static backscatter intensity from marine ice at 10 GHz. Left: Co-polarized backscatter intensity. Right: Cross-polarized backscatter intensity.

First, the shape of the mono-static co-polarized backscatter pattern of FYI is distinctly different from that of the MYI and GI. This is particularly evident at 10 GHz (Figure 5.4) and to a less degree as the frequency decreases to 6 GHz. FYI has a significantly lower co-polarized backscatter intensity than MYI and GI, but also has azimuth angles where the intensity "spikes". The azimuth angles where these spikes occur are associated with the normal of a relatively large[32] flat or convex face (ie. a reflector) on the ice target. It was theorized that this was related to a higher degree of surface scattering phenomena occurring in FYI than in MYI and GI. This will be investigated in Section 5.3. These spikes are also evident in the MYI and GI plots, but are masked by the overall omni-directional backscatter intensity of these marine ice types.

Second, although the co-polarized backscatter patterns of MYI and GI are similar, in that they are more isotropic than FYI, the average backscatter intensity of MYI decrease from about 5 dB lower than GI at 6 GHz to 10 dB lower at 10 GHz. The same is true about the cross-polarized backscatter intensity of MYI and GI. Despite these differences, there appears to be significant overlap in the co-polarized and cross-polarized backscatter intensity of MYI and GI. The overlap in the intensity of MYI and GI would make it very difficult, if not impossible, to differentiate between the two marine ice types using the co-polarized backscatter at these frequencies. It would also be difficult to differentiate between FYI and the hazardous ice types (MYI and GI), using co-polarization, because of the spikes in intensity that overlap with the MYI and GI. These trends will be further explored in the histograms in Figures 5.5 through 5.7 (left-hand side), and discussed below.

The cross-polarized backscatter intensity is more promising, showing a distinct difference in the backscatter intensity between safe ice and hazardous ice. The average cross-polarized backscatter intensity is almost 10 dB lower than MYI and 20 dB lower than GI at 6 GHz and this difference increases as the frequency increases. Therefore, the cross-polarized backscatter intensity may be a viable method of classifying safe ice (FYI) and hazardous ice (MYI and GI). This will be further explored using histograms of the cross-polarized backscatter intensity in Figure 5.5 through 5.7 (right-hand side).

The histograms provide a better method of viewing the trends and differences in the overall backscatter intensity of three marine ice type[33]. Visually, one can see that as the frequency increases from 6 to 10 GHz, the degree of overlap in the co-polarized backscatter intensity distribution between FYI and the hazardous ice types (MYI and GI) appears to increase. Conversely, the degree of overlap in the cross-polarized backscatter intensity distribution between safe and hazardous ice appears to decrease. The degree of overlap is quantified in Table 5.1.

At 10 GHz, there is minimal overlap (~12%) between safe ice and hazardous ice. Therefore, the cross-polarized backscatter intensity may be used to classify marine ice with approximately an 85% confidence level. This was rounded down from 88%, due to the 4 dB uncertainty in the cross-polarized backscatter intensity caused by the meshing and halfspace representation decisions. This

---

[32] "large" refers to greater than one (1) wavelength.

[33] Nevertheless, we will continue to show the polar plots of the backscatter intensity so that details can be examined if needed.

Table 5.1 Degree of overlap in the backscatter intensity distribution between safe ice (FYI) and hazardous ice (MYI and GI) at 6, 8 and 10 GHz.

Frequency	Co-polarized Overlap	Cross-polarized Overlap	Depolarization Overlap
6 GHz	30%	26%	99%
8 GHz	32%	22%	98%
10 GHz	62%	12%	68%

is good, but far below the desired 95% confidence rate. However, the overall trend suggests that at some higher frequency, the overlap may be negligible.

Figures 5.8 through 5.10 present two methods of viewing the depolarization of the three marine ice types: the left-hand plot is the depolarization difference distribution by intensity and the right-hand plot is a scatter plot of the cross-polarization versus the co-polarization. At 6 and 8 GHz, the depolarization difference of FYI, MYI and GI is essentially equal with greater than 98% overlap. This decreases sharply at 10 GHz to 68% overlap, but is still significant. Therefore, depolarization does not provide any useable information at these frequencies. However, if the co-polarization is plotted in terms of the cross-polarization at each azimuth angle using scatter plot, three distinct regions are evident: one for each marine ice type. The trend in these scatter plots is that as the frequency increases, the degree of overlap between FYI and the hazardous ice types decreases, as well as the degree of overlap in the MYI and GI. The key discriminator in these plot is the cross-polarized backscatter intensity.

In conclusion, regardless of frequency, GI produces the strongest co-polarized and cross-polarized backscatter intensities. MYI has a very similar backscatter response and cannot be easily distinguished from GI at 6 and 8 GHz, but starts to show some separation in intensity at 10 GHz. At certain angles, the strength of the co-polarized backscatter intensity of FYI at all frequencies can be as strong as hazardous ice types (where the intensity spikes), but can be classified as FYI to a high degree of confidence if the cross-polarization is greater than 10 dB lower than the co-polarization. The key discriminator between FYI, MYI and GI appears to be the cross-polarization response: particularly at 10 GHz where FYI has a significantly weaker cross-polarization. In fact, as is evident in Figure 5.10 (right - the scatter plot for 10 GHz) and Table 5.1, hazardous ice can be classified with approximately an 88% degree of confidence at 10 GHz from the cross-polarized backscatter intensity. The overall trend suggests that at 12 GHz or higher, the cross-polarized backscatter intensity could provide classification between safe and hazardous ice to higher degree of confidence.

In Section 5.5, it will be shown that the results at 10 GHz and the trend in the separation between safe and hazardous ice as the frequency increases are supported by the experimental data at 16 GHz.[34]

---

[34] Unfortunately, the computational resources required to study the backscatter signature from marine ice at 16 GHz exceed those available through the Rapid Access Service (limited access) of the Compute Canada High Performance Computing network. This will be an area of future work, if possible, using extended resource allocations obtained through the Resource Allocation Competitions of Compute Canada. We mention this to make known the fact that

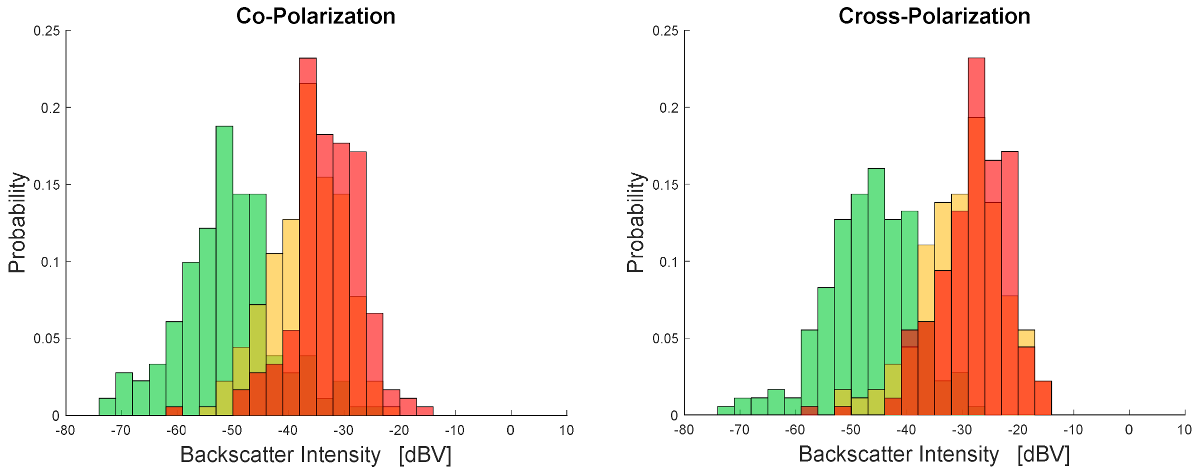

Figure 5.5 Histogram of backscatter intensity probability distribution from marine ice at 6 GHz.

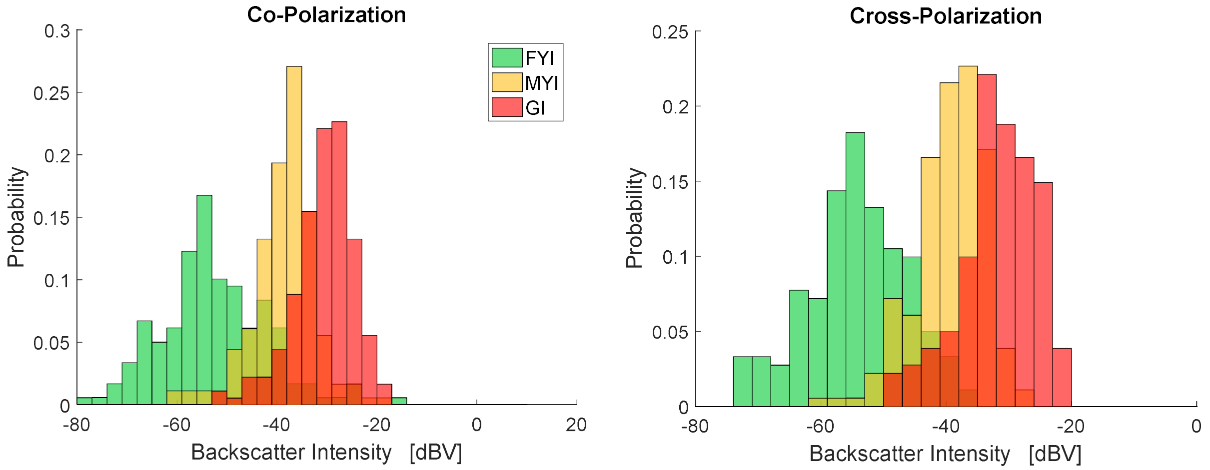

Figure 5.6 Histogram of backscatter intensity probability distribution from marine ice at 8 GHz.

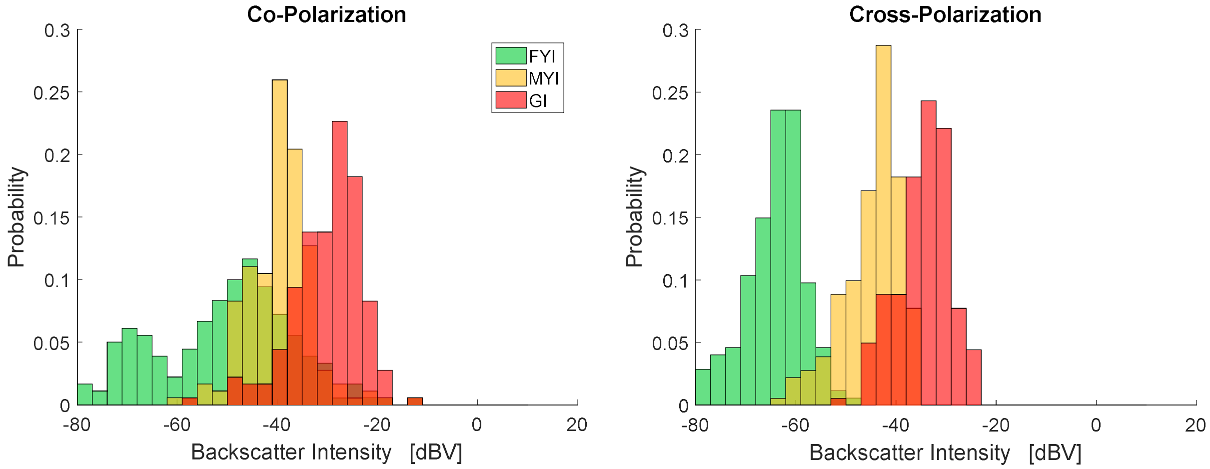

Figure 5.7 Histogram of backscatter intensity probability distribution from marine ice at 10 GHz.

---

access to sufficient compuational resources exist to allow the study of scattering from ice objects at frequencies higher than 10 Ghz using the CEM models presented in this work.

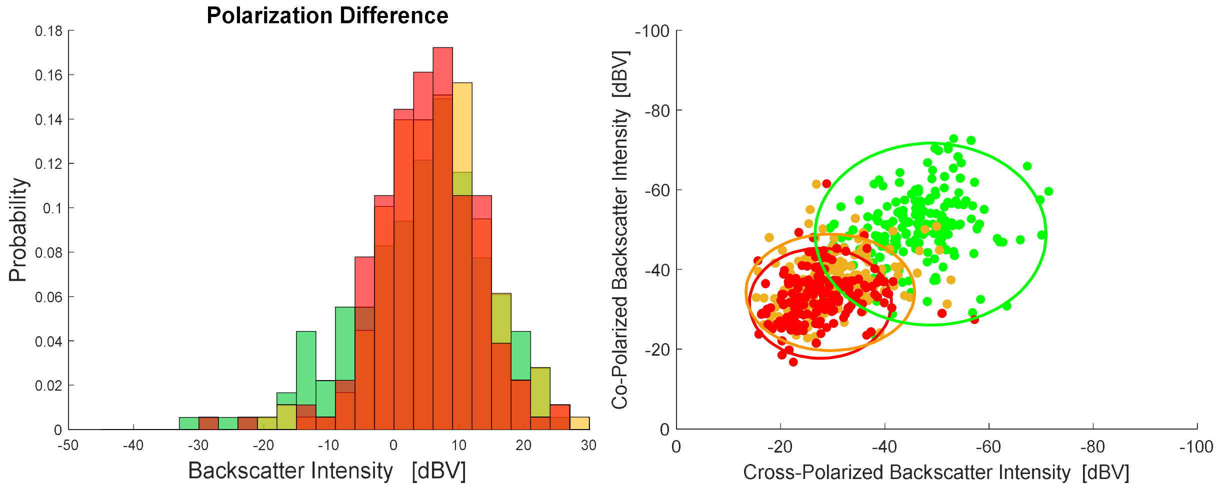

Figure 5.8 Histogram (left) and scatter plot (right) examining depolarization at 6 GHz.

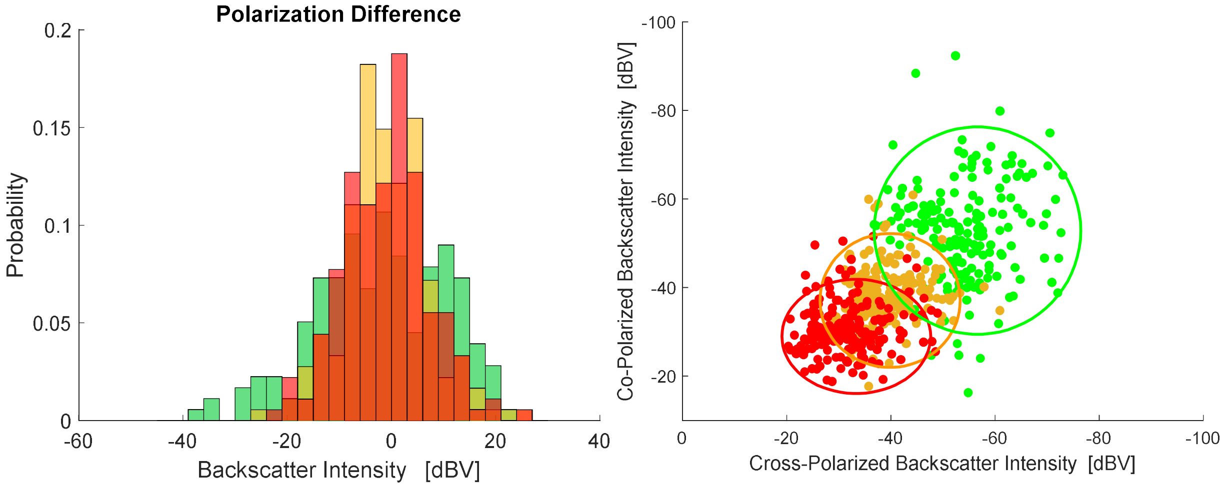

Figure 5.9 Histogram (left) and scatter plot (right) examining depolarization at 8 GHz.

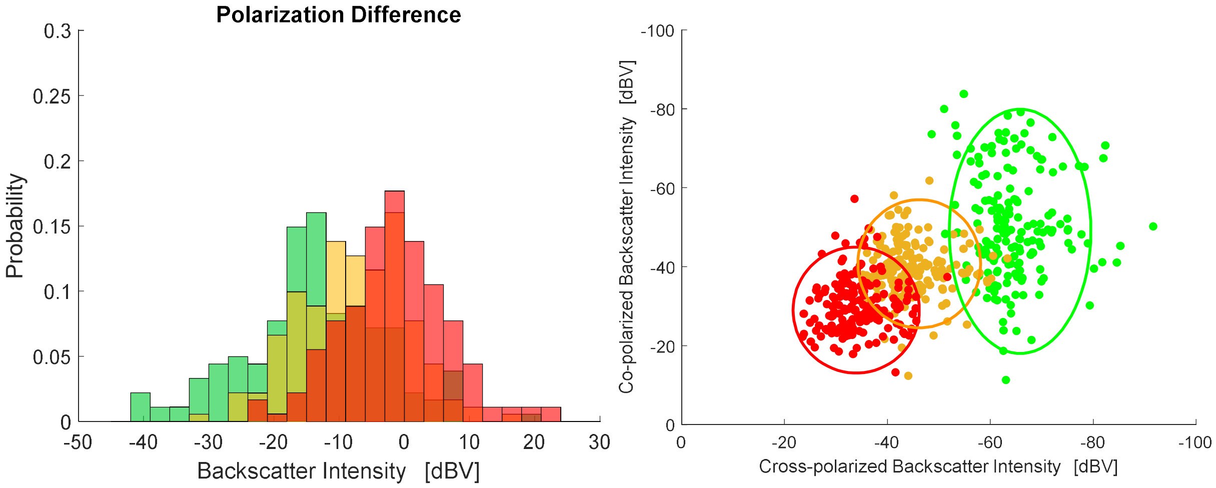

Figure 5.10 Histogram (left) and scatter plot (right) examining depolarization at 10 GHz.

5.3 Surface and Volume Scattering Phenomena at 10GHz

In Section 5.2, it was observed that the FYI co-polarized mono-static backscatter pattern was distinctly different from the MYI and GI. Specifically, FYI has spikes of backscatter intensity that are associated with the normal to a face of the ice object. It was theorized that this was due to a higher degree of surface scattering versus volume scattering phenomena occurring in FYI. This theory is also supported by the fact that the penetration depth of MYI and GI is much greater than that of FYI. Hence, the electromagnetic wave penetrates deeper into the volume and more volume scattering is possible. To test this theory, the backscatter intensity patterns of marine ice were compared to the backscatter from an identical object made of a perfect electrical conductor (PEC).

It is known that scattering from a PEC object is entirely a surface scattering phenomenon. The electromagnetic field anywhere inside a PEC body is equal to zero and no volume scattering can occur. Therefore, the greater the similarity of the backscatter pattern to that of a PEC object of the same size and shape, the greater the surface scattering phenomena.

Figures 5.11 and 5.12 are plots of the normalized mono-static backscatter intensity for the three ice types of interest (FYI, MYI and GI) and the same object made of PEC at 8 and 10 GHz respectively. The plots have been normalized in order to compare the relative intensity of the patterns as opposed to the measured intensity of the backscatter. Visually, the co-polarized mono-static backscatter pattern of FYI is similar to that of the PEC.

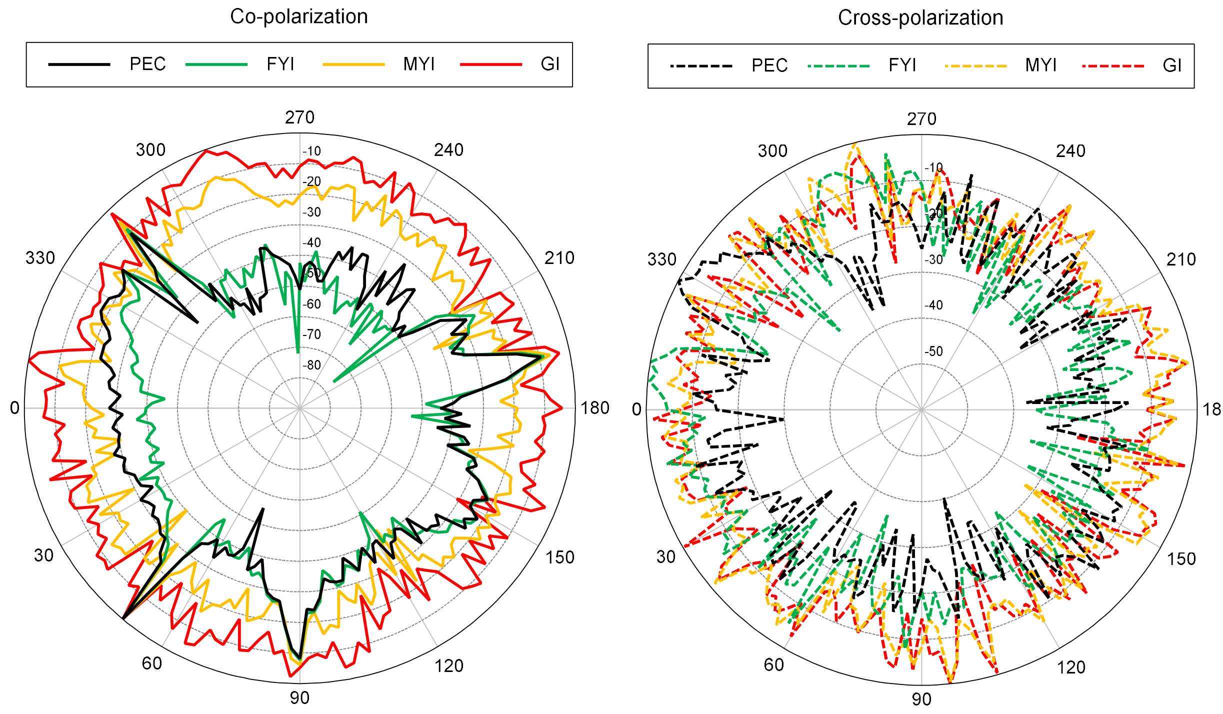

Figure 5.11 The normalized mono-static backscatter intensity from marine ice compared to the ice object made of PEC at 8 GHz. Left: Co-polarized backscatter intensity. Right: Cross-polarized backscatter intensity.

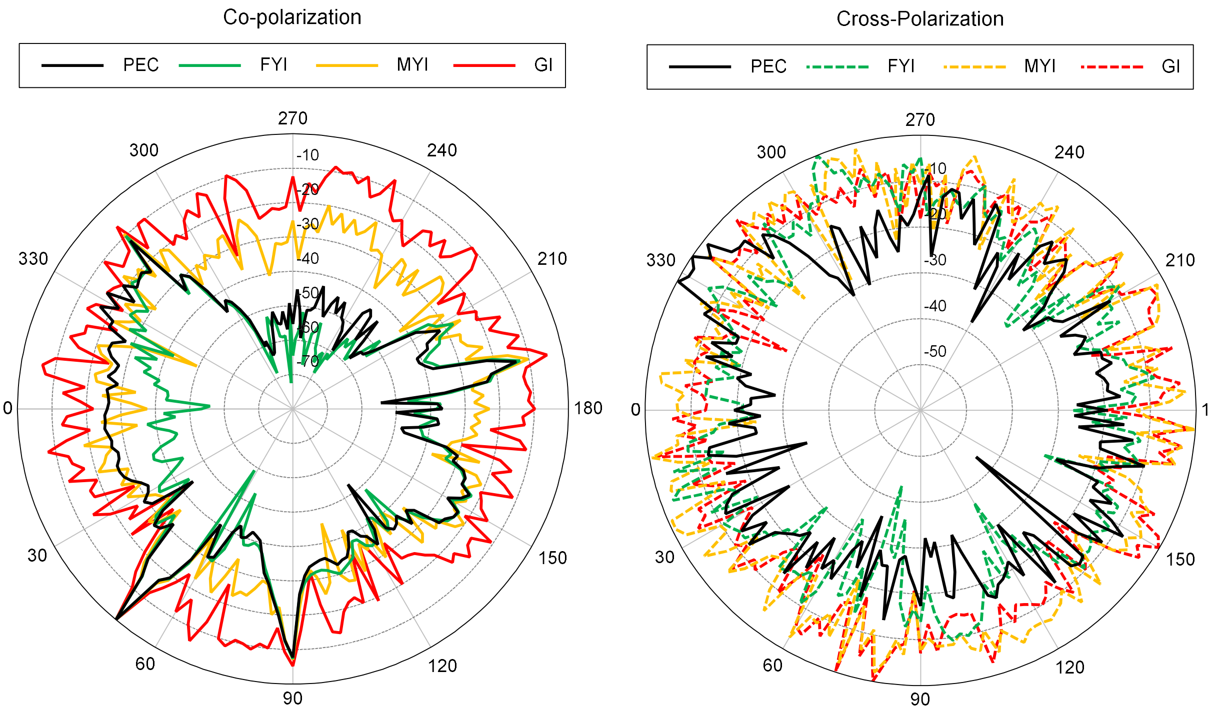

Figure 5.12 The normalized mono-static backscatter intensity from marine ice compared to the ice object made of PEC at 10 GHz. Left: Co-polarized backscatter intensity. Right: Cross-polarized backscatter intensity.

Using the antenna pattern measurement technique from Section 4.8.2, these patterns can be compared and the difference quantified, such that the smaller the difference, the greater the similarity. Using this method, patterns with a -50 to -60 dB difference are generally considered to be equal. Figures 5.13 and 5.14 show the difference between the normalized mono-static backscatter intensity patterns from the three ice types compared to the PEC object, at 8 and 10 GHz respectively. Overall, the co-polarized backscatter pattern of FYI most closely matches that of a PEC (ie. the smallest difference), followed by MYI then GI having the largest difference at all frequencies. Table 5.2 shows the average of the difference values for the co-polarized and cross-polarized backscatter intensity patterns. The average co-polarized backscatter intensity difference for FYI is less than -40 dB at all frequencies, whereas the difference for MYI is greater than -35 dB and for GI is greater than -20 dB. Therefore, this demonstrates that FYI is dominated

Table 5.2 Average co-polarized and cross-polarized normalized backscatter intensity pattern difference for FYI, MYI and GI compared to a PEC object from 6 to 10 GHz.

Frequency	Average Co-polarization Difference			Average Cross-polarization Difference		
	FYI	MYI	GI	FYI	MYI	GI
6 GHz						
8 GHz	-44.2 dB	-25.7 dB	-14.1 dB	-20.3 dB	-15.5 dB	-15.4 dB
10 GHz	-47.2 dB	-34.2 dB	-20.6 dB	-21.6 dB	-13.0 dB	-16.4 dB

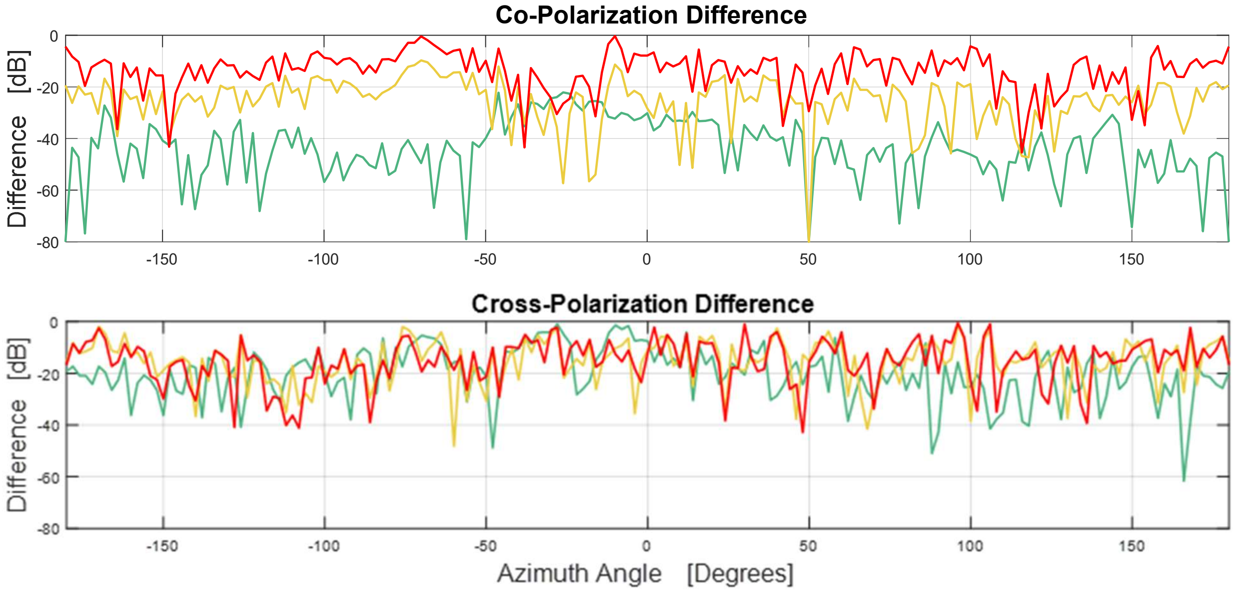

Figure 5.13 Numerical comparison of the difference between the mono-static backscatter intensity of FYI, MYI and GI compared to a PEC target at 8 GHz.

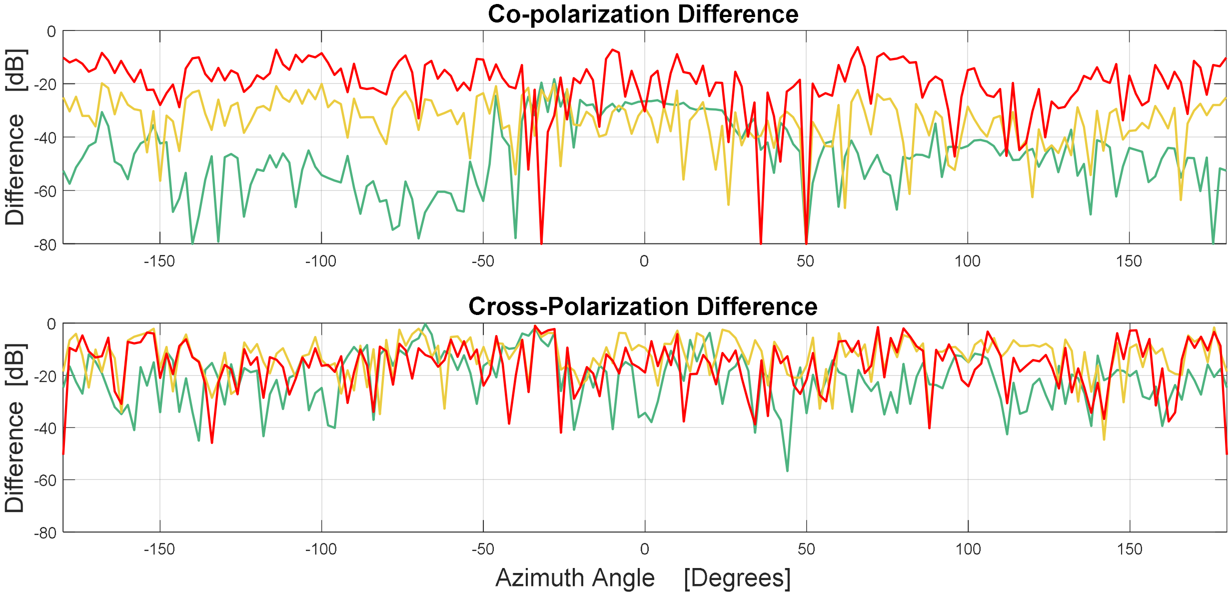

Figure 5.14 Numerical comparison of the difference between the mono-static backscatter intensity of FYI, MYI and GI compared to a PEC target at 10 GHz.

by surface scattering phenomena, whereas MYI and GI are dominated by volume scattering. The cross-polarized backscatter intensity difference does not show this same trend. In fact, the cross-polarization difference does not change significantly as the frequency changes. This suggests that even a small amount of volume scattering causes a significant change in the cross-polarized backscatter intensity. Additionally, as the frequency increases, the pattern difference between for all three ice types decrease.

These results are not unexpected and can be explained by the physics of the respective permittivity of the marine ice types. The real permittivity of the three ice types does not change significantly between 6 and 10 GHz and are relatively similar: between 3.38-3.44 for FYI and approximately 3.01 for MYI and GI (see Table 4.3 for greater detail). Therefore, their reflection coefficients are essentially the same and do not explain the difference in the surface versus volume scattering phenomena as the frequency changes or between ice types. However, the penetration depth changes significantly (by an order of magnitude) between FYI, MYI and GI, as shown in Figure 5.15.

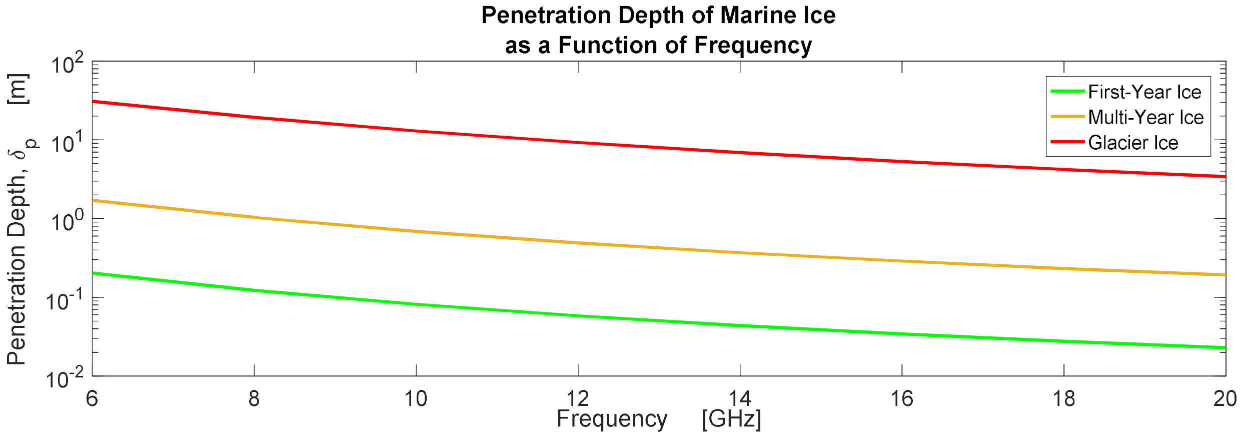

Figure 5.15 Plot of the penetration depth of first-year ice, multi-year ice and glacier ice at a temperature of -2°C as a function of frequency.

The penetration depth is a function of frequency and the imaginary part of the permittivity, given by:

$$\delta_p = \frac{1}{2\alpha} \tag{3.26}$$

where

$$\alpha = \frac{2\pi}{\lambda_o}\left|Im\sqrt{\varepsilon}\right| \tag{3.27}$$

From Figure 5.15 and examining the imaginary part of the permittivity of FYI, MYI and GI from Table 4.3, it is apparent that the order of magnitude difference between ice types is related to the order of magnitude difference in their imaginary permittivity. The decrease in the penetration depth is directly related to the combination of an increase in the imaginary permittivity and the decrease in the wavelength as the frequency increases. Both of which, increase α and decrease the penetration depth. Therefore, the electromagnetic wave attenuates more rapidly and less volume scatter and internal reflection occurs and the object begins to be dominated by the surface scattering phenomena and appear more like a PEC object.

5.4 Effects of Small Target Movements

To simulate and explore the effects of small target movements, as would be expected from an ice target on a wavy sea, the ice objects from the study of backscattering from marine ice in Section 5.2 were tilted 1 degree about the x-axis and 1 degree about the y-axis. The three patterns were then averaged and compared to the original three patterns, as shown in Figures 5.19. This would be similar to integrating the returns between sweeps in the radar post-processing.

The effect of averaging the patterns is to reduce the depth of any nulls, decrease the average intensity of FYI and increase the average intensity of MYI and GI. This is particularly noticeable when comparing the histograms in Figures 5.16 through 5.18. The average backscatter intensity of FYI decreased by 1 dB for co-polarization and 4 dB for cross-polarization. Whereas the average backscatter intensity of MYI increased by 8.5 dB for co-polarization and 9.5 dB for cross-polarization, and GI increased by 11.4 dB for co-polarization and 12.5 dB for cross-polarization. The overall effect of the averaging is to reduce the overlap in the backscatter intensity distribution of safe ice and hazardous ice, such that cross-polarization can be used to classify safe or hazardous ice with 99% confidence.

However, it was decided not to use averaging of multiple orientations (tilts) of the ice targets in the analysis of backscatter from marine ice because the clutter from an ice floe or sea clutter are "stationary" clutter and does not fluctuate from pulse to pulse. Therefore, the clutter will increase at the same rate as the target signal and no advantage in signal-to-clutter would be gained [86]. Integration or averaging of the backscatter intensity would only provide an advantage in a clutter free environment, as is the case in these engineering models due to the flat sea assumption.

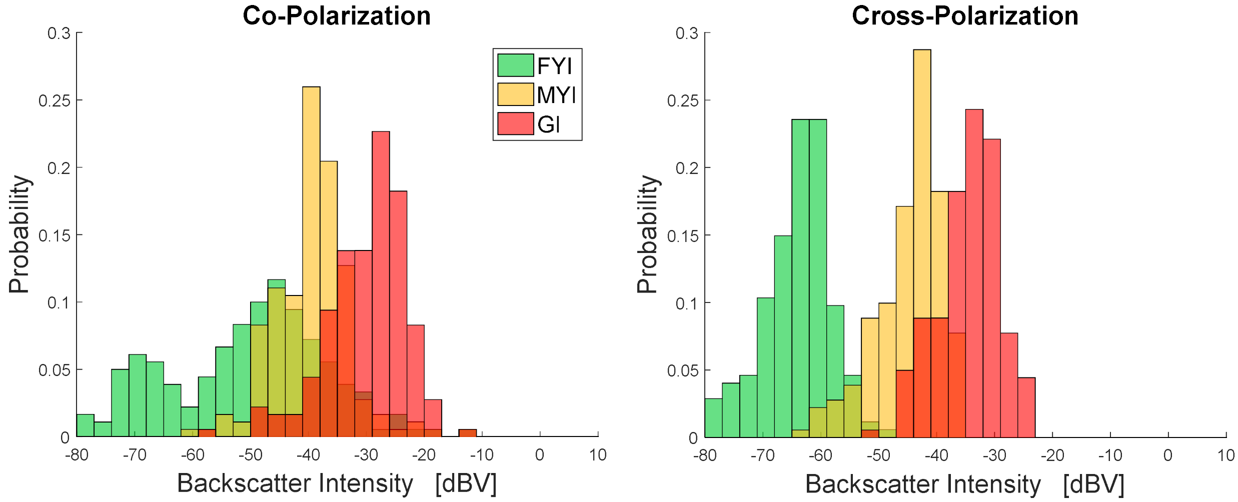

Figure 5.16 Histogram of backscatter intensity probability distribution from marine ice at 10 GHz.

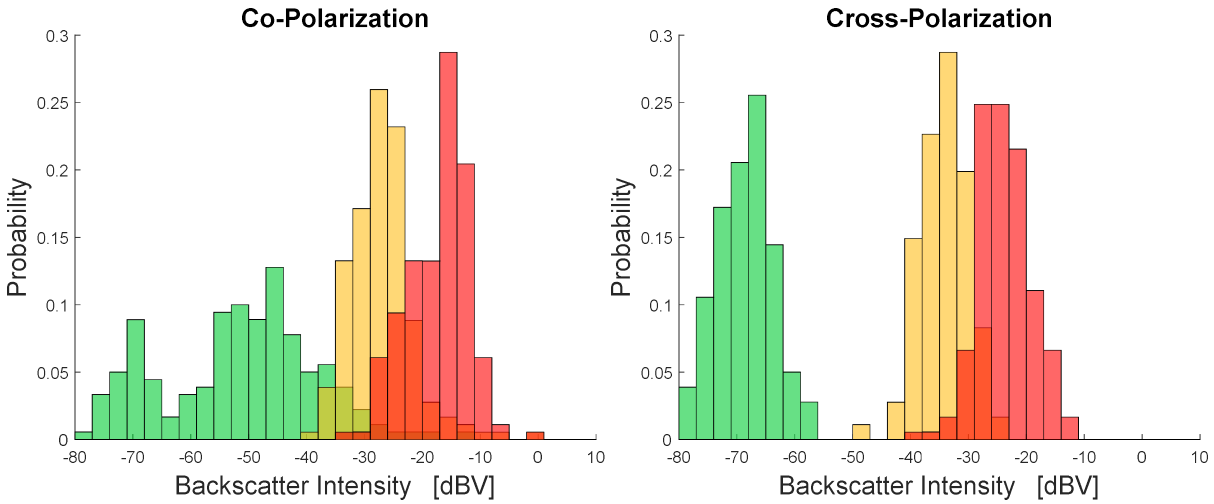

Figure 5.17 Histogram of averaged backscatter intensity probability distribution from marine ice with small target movements (integrated of signal returns) at 10 GHz.

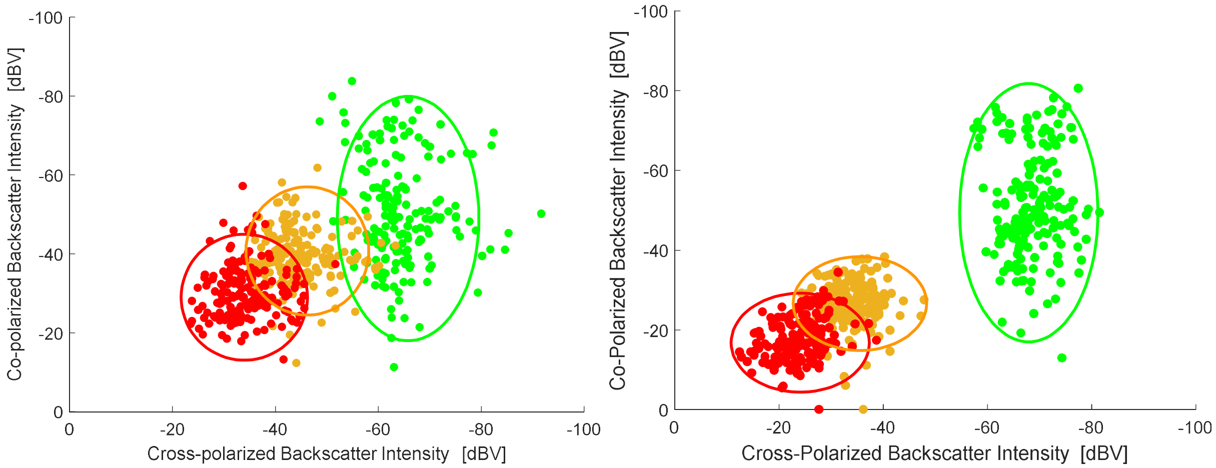

Figure 5.18 Scatter plots of the co-polarized versus cross-polarized backscatter intensity of marine ice at 10 GHz. Left: A single level ice target. Right: Averaged values from three target movements.

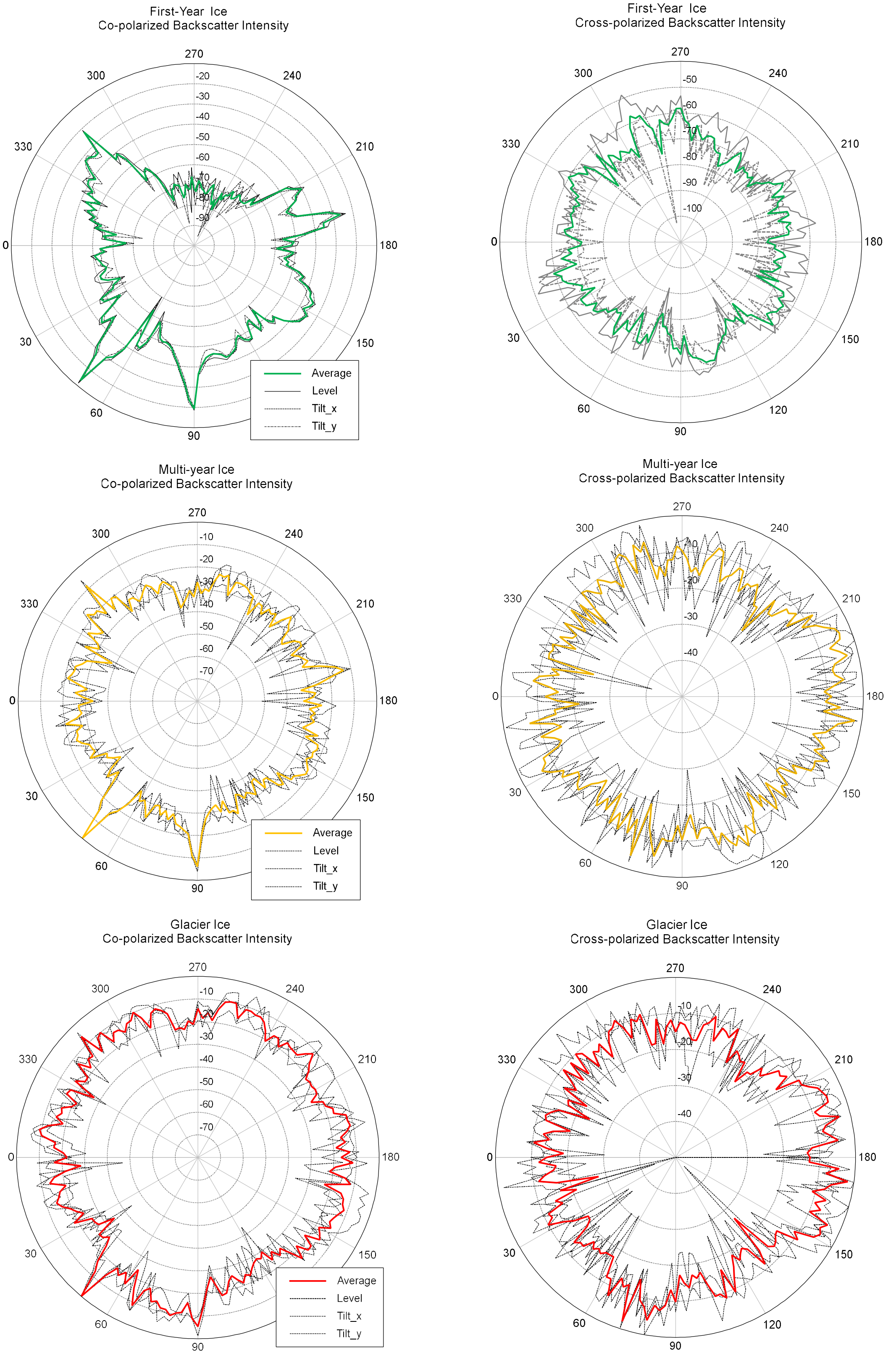

Figure 5.19 Polar plots of the averaged mono-static backscatter intensity from marine ice with small target movements at 10 GHz. Left: Co-polarized backscatter intensity. Right: Cross-polarized backscatter intensity.

5.5 Validation of the Engineering Models

The use of the method of moments to solve the wave equation and model the electromagnetic environment is well established [87] [88], and the methodology presented in this work was validated in Section 4.8. In this Section, the results of the engineering models will be validated against experimental results, to show that the engineering models represent real world marine ice targets.

As stated in Section 3.11, there has been a limited amount of research conducted in surface-based radar remote sensing of marine ice over the past 20-30 years. However, there is data available from Haykin et al. [13] and Orlando et al. [73] which will be used for comparison and validation.

The original intention was to conduct the comparison and validation of the engineering models using data collected at 16 GHz (Ku-band), because this is the best set of data presented by [13] [73]. However, due to limited computational resources, it was not possible to run the engineering models at 16 GHz. The maximum frequency of the backscatter study presented here was 10 GHz (X-band). It should also be noted that the experimental data was collected for MYI and GI targets trapped in a land-fast FYI floe, whereas the modelled targets are tabular FYI, MYI and GI targets floating in open water. Finally, the experimental data was collected prior to the spring thaw, whereas the models presented in this work were for summer condition marine ice expected during the navigation season. Therefore, as opposed to a direct comparison with the experimental data, the trends in the modelled data and the experimental data will be discussed to show that the models are producing results similar to real world marine ice targets.

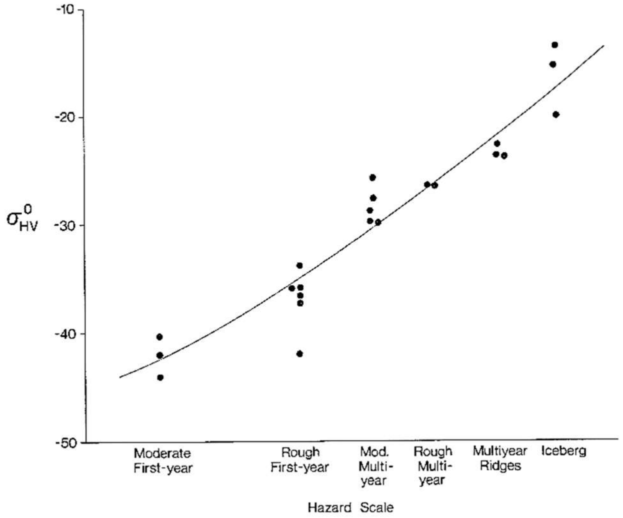

Figure 5.20 Plot of the cross-polarized normalized radar cross-section versus hazard scale for FYI, MYI and GI at 16 GHz (Ku-band). Courtesy of [13].

Haykin et al. [13] conducted their radar experiments at 3 GHz (S-band), 10 GHz (X-band), 16 GHz (Ku-band) and 35 GHz (Ka-band) and found that cross-polarized normalized RCS (σ_{HV}^0) was directly related to the hazard level of the ice. As discussed in Section 3.8.4, the normalized RCS is directly related to the backscatter intensity, and any difference between ice types or between co-polarization and cross-polarization would be equal. Figure 5.20 shows that at 16 GHz, as the backscatter intensity increases (normalized RCS), the ice type transitions from FYI (lowest intensity of return), to MYI, then GI (strongest intensity of return). In [13], Haykin indicates that this trend occurred at X-band but possibly to a lesser degree[35]. This trend in the experimental results directly correlates to the results observed in the engineering models of marine ice at 10 GHz presented in Section 5.2. Additionally, the experimental data shows that the backscatter intensity of MYI targets is approximately 10 dB lower than GI and FYI is approximately 10 to 15 dB lower than MYI. The engineering model of marine ice shows that MYI is approximately 10 dB lower than GI and FYI is 10 dB lower than MYI.

In Figure 5.21, the co-polarized backscatter intensity has been plotted against the cross-polarized backscatter intensity for the engineering models of marine ice similar to a plot of the co-polarized normalized RCS versus the cross-polarized RCS for the experimental data from [13]. Again, it should be noted that the engineering model data is for backscattering from marine ice at 10 GHz, whereas the experimental data was collected at 16 GHz. The goal of this comparison is not to show that the values are similar, but rather to show that the engineering models are producing results similar to experimentally measured marine ice. Specifically, that the FYI, MYI and GI modelled data displays the same clustering and co-polarization versus cross-polarization ratios (depolarization).

In conclusion, this comparison shows that the engineering models of marine ice are behaving in a similar manner to real world marine ice.

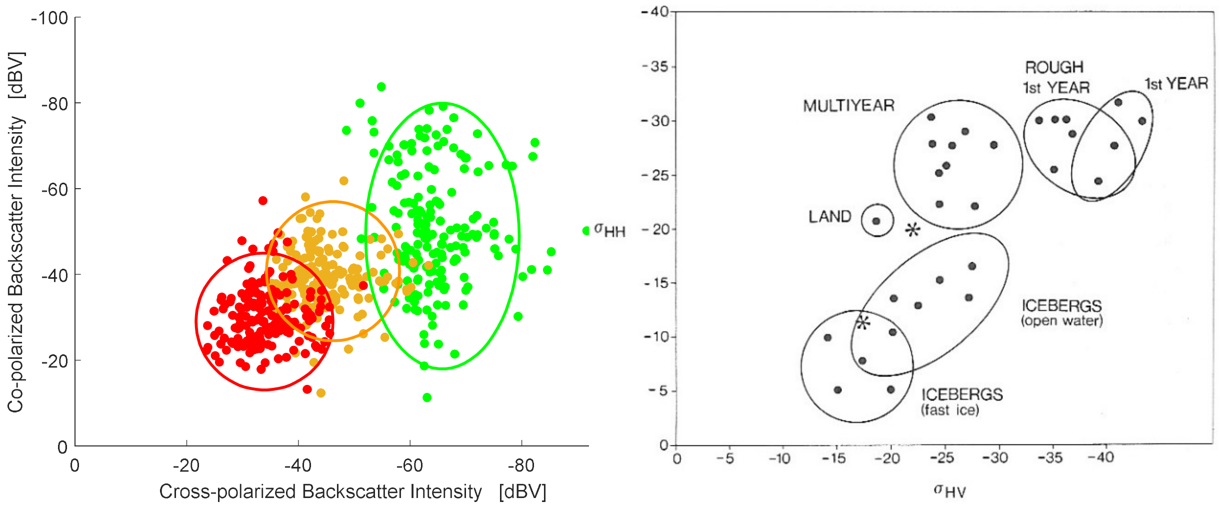

Figure 5.21 Scatter plots comparing the co-polarized and cross-polarized backscatter intensity from the engineering models at 10 GHz (left) with the experimentally measured co-polarized and cross-polarized normalized RCS from [13] at 16 GHz (right).

---

[35] The X-band radar used in the experiments had a wide beamwidth causing significant off-target illumination. As a result of the quality of the data, Haykin indicated the results were not presented but were similar to those collected using Ka-band with respect to the hazard scale indicated in Figure 5.#.

5.6 Conclusions

The engineering models developed in Chapter 4 and used to model summer condition marine ice in Chapter 5 have been validated through comparison with the (albeit limited) experimental data available. This study, and the subsequent comparison with experimental data, verifies the feasibility of using computational electromagnetic modelling to study backscatter from marine ice. Given sufficient access to the high performance, but reasonably accessible, computing resources, vast amounts of backscatter data can be produced for marine ice under any desired physical and environmental conditions within hours or days, and at a fraction of the cost of sending expeditions to the Arctic for weeks or months at a time.

In addition, with respect to the long-term goal of this research to develop requirements for an ice classification radar, the following was found:

a) the results of Section 5.2 suggest that 10 GHz can be used to classify safe ice from hazardous ice to fairly high degree of confidence (approximately 88%);
b) the trend, with respect to the effect of frequency on the backscatter signature, identified in Section 5.3 suggests that an optimal frequency may exist between 10 GHz and 16 GHz, for classification of marine ice during the summer navigation period using a dual-polarization radar to sense both the co- and cross-polarized backscatter.

6. CONCLUSIONS & FUTURE WORK

Although the multi-year ice cap has receded, and the Canadian Arctic has become open to navigation during the summer months, this does not mean it is ice free. The decaying ice floes move with the wind and current, and open channels and bays can quickly become ice-inhabited[36]. As commercial shipping and tourism interest in the Canadian Arctic, so will the number of vessel transiting these waters and the potential for collisions with ice. To improve the safety of navigation in the Arctic, there is a need for shipborne navigation radars capable to distinguish (ie. classify) hazardous multi-year ice (MYI) and glacier ice (GI) from safe first-year ice (FYI). To date, there are no such ice classification radars are commercially available.

In order to fully define the requirements for an ice classification radar, it is necessary to gain a better understanding of the effects of frequency on the co- and cross-polarized backscatter from a great variety of shapes and sizes of the three marine ice types (FYI, MYI and GI) and under a great variety of environmental conditions. To do this through experimentation would require significant resources, time and money. Some 25 years ago, Haykin et al. [13, p. 344] correctly remarked that "… it is very difficult to predict the radar cross section of ice targets …" and that "empirical data remain the most important source of predicted ice-scattering strength". In this thesis, we have shown that such "prediction" is now feasible and could be used to "gather" data on the scattering from marine ice objects in much the same way that engineers have used simulations to fine-tune many aspects of complex communications systems. To the best of our knowledge, this is the only study to date of backscattering from marine ice for surface-based remote sensing, using computational electromagnetic modelling CEM).

6.1 Contributions

The principal contributions of this thesis are:

- A comprehensive study of the literature on the geophysical science of marine ice has been completed. Using this knowledge, and dielectric mixing theory, a set of algorithms were produced to calculate the electromagnetic properties of a homogenised version (ie.

---

[36] The term "ice-infested" is often used, and in the opinion of the author and some ice researchers is incorrect because of its negative connotation and suggestion that ice should not be there. It is correct in suggesting that ice can quickly swarm and cause harm to a vessel though.

effective complex permittivity) of the three marine ice types of interest, namely first-year ice, multi-year ice, and glacier ice. This can now be done over a wide range of frequencies, temperatures and bulk ice salinity values, based on the best scientific evidence available;

- An effective methodology for the computational electromagnetic modelling (CEM) of marine ice as homogenized lossy dielectric objects has been established;
- The engineering models developed, and used to compute the backscattering from summer condition marine ice, have been validated through comparison with (albeit limited) existing experimental data available;
- Computational case studies were performed to determine how large the moment method mesh size can be and yet provide reliable far-zone backscatter predictions;
- Comparative studies of three different orders of computational complexity for the presence of a flat sea were completed, and the Fresnel reflection coefficient representation was found to be suitable for computations of the co- and cross-polarized backscatter. However, if only the co-polarized or total backscatter is of interest, the perfect electrical conductor (PEC) was found to be suitable;
- It was demonstrated that, with access to high performance, yet reasonably accessible, computing resources, vast amounts of backscatter data could be produced for marine ice under any desired physical and environmental conditions within hours or days, and at a fraction of the cost of sending expeditions to the Arctic for weeks or months at a time; and
- This study showed that a dual-polarization radar operating at 10 GHz can be used to classify safe ice from hazardous ice to a fairly high degree of confidence (approximately 88%), and that an optimal frequency for definitive classification of marine ice, during the summer navigation period, may exist between 10GHz and 16 GHz.

Some of the lesser contributions of this thesis are:

- We have clarified and connected otherwise seemingly disparate definitions of various radar cross-section and backscattered electric field related concepts;
- The industry trend is to measure and test antennas using spherical near-field based measurement methods. We have shown how quickly and easily the spherical wave coefficients obtained from this testing method may be imported into most commercial CEM software suites and used to completely describe the pattern of such antennas. In doing so, we have essentially removed the need to ever again discuss whether some approximate model of an antenna (that exists and has been tested) is good enough for use in accurate modelling of the performance of the antenna on the platform; and
- Furthermore, we have shown that, should the spherical wave coefficients not be available from an antenna supplier (for whatever reason), the back-projected data can be used to establish an equivalent planar array model of the antenna and accurately model its pattern in the forward hemisphere. Thus, this will only work well for high-directivity antennas.

6.2 Conference Papers

Preliminary portions of this work have been presented in three conference papers :

R.A.W. Trembinski and D.A. McNamara, "On the modelling of antenna pattern performance using equivalent source distributions for vehicle antenna placement engineering", URSI National Radio Science Meeting Digest, San Diego, USA, July 2017.

R.A.W. Trembinski and D.A. McNamara, "The engineering modelling of electromagnetic wave scattering from sea ice by surface-based radar", URSI National Radio Science Meeting Digest, Boston, USA, July 2018.

R.A.W. Trembinski, D.A. McNamara & D.J. Janse van Rensburg, "Utilizing spherical near-field measurement data in antenna on-platform performance studies", Proc. 18th International Symposium on Antenna Technology and Applied Electromagnetics (ANTEM), Waterloo, Canada, August 2018.

6.3 Future Work

There remain some issues/cases whose investigation in the future might prove useful:

- Foremost would be to explore the co- and cross-polarized backscatter between 10GHz and 16 GHz to identify an optimal frequency for the classification of marine ice using dual-polarization;
- This thesis presented the backscatter signatures of the three marine ice types of interest at one temperature and bulk salinity. The same models should be run for different ice surface temperatures and compositions (ie. different effective permittivities) to ensure the results hold for ice during different periods of the summer melt season;
- Additionally, to ensure year-round operation in ice, once a potential optimal frequency is identified, the models should be run for marine ice temperatures and bulk ice salinity profiles expected during the winter months;
- The incorporation of a rough sea surface in the model, to explore the effects of sea surface roughness on the propagation factor and hence the radar cross-section of the ice target;
- The incorporation of a thin surface layer of fresh water or seawater on the ice object, to explore the effects on the backscatter signature of marine ice;
- Focused on FYI and MYI during the melt and summer season. For year-round operation in ice, models most likely need to be modified for salinity profiles and ice formations during winter (different dielectric properties and structures), and incorporated in the radar's ice classification processing. Model these conditions to determine applicability or modification required;
- Finally, the difference between a horizontally and a vertically polarized plane wave source should also, and can easily, be explored to determine the effects on the backscatter

signature. This thesis only examined the use of a horizontally polarized plane wave source because this orientation minimizes sea clutter intensity and matched the radar transmitter used in the experimental work, which was used to validate the engineering models.

References

[1] M.-J. Vinas, "See how arctic sea ice is losing its bulwark against warming summers," 28 October 2016. [Online]. Available: https://www.nasa.gov/feature/goddard/2016/arctic-sea-ice-is-losing-its-bulwark-against-warming-summers. [Accessed 9 March 2017].

[2] J. Richter-Menge, J. Overland, J. Mathis and E. Osborne, "Arctic Report Card: Update for 2017," http://www.arctic.noaa.gov/Report-Card, 2017.

[3] K. Fox and B. Miller, "Arctic temperatures surge in the dead of winter," 27 February 2018. [Online]. Available: https://www.cnn.com/2018/02/27/weather/arctic-temperatures-record-high-intl/index.html. [Accessed 10 March 2018].

[4] F. Ulaby, R. Moore and A. Fung, "Volume 2 - Radar remote sensing and surface scattering and emission theory," in *Microwave remote sensing: Active and passive*, Reading, MA, Addison-Wesley Publishing, 1 January 1982, pp. 457-1047.

[5] Geophysical Monograph 68, Microwave Remote Sensing of Sea Ice, F. Carsey, Ed., Washington, DC: American Geophysical Union, 1992.

[6] B. O'Connell, "Ice Hazard Radar," Canadian Coast Guard, Ottawa, ON, Canada, 2016.

[7] Environment and Natural Resources - Northwest Territories, "Trends in shipping in the Northwest Passage and the Beaufort Sea," 29 May 2105. [Online]. Available: http://www.enr.gov.nt.ca/en/state-environment/73-trends-shipping-northwest-passage-and-beaufort-sea. [Accessed 9 March 2018].

[8] Fraunhofer-Gesellschaft, "Safe navigation through the Northwest Passage," 3 November 2016. [Online]. Available: https://phys.org/news/2016-11-safe-northwest-passage.html. [Accessed 10 March 2018].

[9] C. Mooney, "The Arctic dilemma," *The Washington Post,* 21 December 2017.

[10] N. Vanderklippe, "China reveals plans to ship cargo across Canada's Northwest Passage," 20 April 2016. [Online]. [Accessed 10 March 2018].

[11] Arctic Council, "Arctic Marine Shipping Assessment 2009 Report," Protection of the Arctic Marine Environment, April 2009.

[12] JCOMM Expert Team on Sea Ice, "Sea-Ice Nomenclature - Report No. 259, Vols. 1, 2 & 3," March 2014. [Online]. Available: https://www.jcomm.info/index.php?option=com_oe&task=viewDocumentRecord&docID=14598. [Accessed 25 March 2018].

[13] S. Haykin, E. Lewis, R. Raney and J. Rossiter, Remote sensing of sea ice and icebergs, New York, NY: John Wiley & Sons, 1994.

[14] G. Timco and M. Johnston, "Guide for understanding and identifying old ice in summer," in *Global Cryosphere Watch - IceTech - Report No. ICETECH08-149*, 2008.

[15] J. Rossiter, J. Guigne, C. Hill, R. Pilkington, E. Reimer, J. Ryan and B. Wright, "Remote Sensing Ice Detection Capabilities - East Coast," Environmental Studies Research Funds Report No. 132, Calgary, AB, Canada, 1995.

[16] J. Luse, "A brief history of the use of marine radar," *Journal of the Institute of Navigation,* vol. 28, no. 3, pp. 199-205, Fall 1981.

[17] S. Haykin, E. Lewis, R. Raney and J. Rossiter, "History of Surface-based Ice Remote Sensing," in *Remote Sensing of Sea Ice and Icebergs*, New York, NY, John Wiley & Sons, 1994, pp. 362-363.

[18] E. Lewis, B. Currie and S. Haykin, "Chapter 1: Introduction," in *Detection and classification of ice*, Great Yarmouth, Great Britain, Galliards Printers Ltd, 1987, pp. 1-12.

[19] Rutter Inc., "http://www.rutter.ca/," 2018. [Online]. Available: http://www.rutter.ca/. [Accessed 17 May 2018].

[20] Raytheon, "Raytheon Canada Ltd," 2018. [Online]. Available: https://www.raytheon.com/ourcompany/global/americas/canada. [Accessed 17 May 2018].

[21] Fednav, "Fednav Homepage," 2018. [Online]. Available: http://www.fednav.com/en. [Accessed 17 May 2018].

[22] National Petroleum Council, "Arctic Potential, Part 2: Technology & Operations," 27 March 2015. [Online]. Available: http://www.npcarcticpotentialreport.org/documents.html#epub. [Accessed 17 May 2018].

[23] Rutter Inc, "Ice Navigator," Rutter Inc, 2018. [Online]. Available: http://www.rutter.ca/ice-navigator. [Accessed 17 May 2018].

[24] Sea Hawk, "Polar/Ice Operations," Sea Hawk, 2013. [Online]. Available: http://www.sea-hawk.com/Polar-Ice-Operations/default.aspx. [Accessed 17 May 2018].

[25] G. Timco and M. Johnston, "Sea ice strength during the melt season," in *Proceedings of the 16th IAHR International Symposium on Ice*, Dunedin, New Zealand, 6 December 2002.

[26] M. Serreze and R. Barry, "Chapter 2: Physical characteristics and basic climate features," in *Arctic Climate System*, New York, NY, Cambridge University Press, 2005, pp. 17-54.

[27] E. Pounder, "Chapter 2: Sea Ice," in *Physics of Sea Ice*, Glasgow, Scotland, Pergamon Press, 1965, pp. 11-30.

[28] G. Frankenstein and R. Garner, "Short Note : Equations for determining the brine volume of sea ice from -0.5 degrees to -22.9 degrees celcius," *Journal of Glaciology,* vol. 6, no. 48, pp. 943-944, 1967.

[29] W. Weeks and S. Ackley, "The growth, structure and properties of sea ice," U.S. Army Cold Regions Research and Engineering Laboratory, CRREL Monograph 82-1, Hanover, NH, 1982.

[30] G. Cox and W. Weeks, "Equations for determining the gas and brine volumes in sea-ice samples," *Journal of Glaciology,* vol. 29, no. 102, pp. 306-317, 1983.

[31] S. Arcone, A. Gow and S. McGrew, "Microwave dielectric, structural and salinity properties of simulated sea ice," *IEEE Transactions on Geoscience and Remote Sensing,* Vols. GE-24, no. 6, pp. 832-840, November 1986.

[32] A. Gow, S. Arcone and S. McGrew, "Microwave and structural properties of saline ice," U.S. Army Cold Region Research and Engineering Laboratory: Report 87-20, Hanover, NH, October 1987.

[33] M. Vant, R. Gray, R. Ramseier and V. Makios, "Dielectric properties of fresh and sea ice at 10 and 35 GHz," *Journal of Applied Physics,* vol. 45, no. 11, pp. 4712-4717, 1974.

[34] M. Vant, R. Ramseier and V. Makios, "The complex-dielectric constant of sea ice at frequencies in the range 0.1-40 GHz," *Journal of Applied Physics,* vol. 49, no. 3, p. 1264, March 1978.

[35] M. Nakawo and N. Sinha, "Growth rate and salinity profile of first-year sea ice in the high Arctic," *Journal of Glaciology,* vol. 27, no. 96, pp. 315-331, 1981.

[36] A. Stogryn and G. Desargant, "The dielectric properties of brine in sea ice at microwave frequencies," *IEEE Transactions on Antennas and Propogation,* vol. 33, no. 5, pp. 523-533, May May 1985.

[37] A. Kovacs, M. R.M. and G. Cox, "Modeling the electromagnetic property trends in sea ice, part I," *Cold Regions Science and Technology,* vol. 14, no. 3, pp. 207-235, 1987.

[38] G. Timco and W. Weeks, "A review of the engineering properties of sea ice," *Cold Regions Science and Technology,* vol. 60, no. 2, pp. 107-129, February 2010.

[39] B. Holt and S. Digby, "Processes and imagery of first-year fast sea ice during the melt season," *Journal of Geophysical Research,* vol. 90, no. C3, pp. 5045-5062, 20 May 1085.

[40] W. Whitman, "Elimination of salt from sea-water ice," *American Journal of Science,* vol. 11, no. 62, pp. 126-132, February 1926.

[41] MANICE, *Manual of Standard Procedures for Observing and Reporting Ice Conditions,* Canadian Ice Service - Environment Canada, ISBN 0-660-62858-9, Catalogue No. En560175/2005, 2005.

[42] J. Addison, "Electrical properties of saline ice," *Journal of Applied Physics,* vol. 40, no. 8, pp. 3105-3114, 1969.

[43] A. Sivhola and J. Kong, "Effective Permittivity of Dielectric Mixtures," *IEEE Transactions on Geoscience and Remote Sensing,* vol. 26, no. 4, pp. 420-430, July July 1988.

[44] W. Weeks and G. Cox, "Salinity variations in sea ice," *Journal of Glaciology,* vol. 13, no. 67, pp. 109-120, 1974.

[45] D. McNamara, *Topics in Electromagnetics I: Momemt Method Course Pack,* Ottawa, ON: University of Ottawa, Winter 2017.

[46] A. Sihvola, Electromagnetic Mixing Formulas and Applications, London, UK: The Institution of Engineering and Technology, 2008, pp. 1-11.

[47] O. Mossotti, "Discussione analitica sull'influenza che l'azione di un mezzo dielettrico," *Memoire di matematica e di fisica della Societa` Italiana delle scienze, residente in,* vol. 24, no. 2, pp. 49-74, 1850. (Included for historical reference)

[48] A. Sihvola, "Lorenz-Lorentz or Lorentz-Lorenz," *IEEE Antennas and Propagation Magazine,* vol. 33, no. 4, p. 56, August 1991.

[49] J. Garnett, "Colours in metal glasses and metal films," *Transactions of the Royal Society,* vol. CCIII, pp. 385-420, 1904.

[50] A. Sihvola, "Mixing rules with complex dielectric coefficients," *Subsurface Sensing Technologies and Applications,* vol. 1, no. 4, pp. 393-415, 2000.

[51] D. Polder and J. van Santen, "The effective permeability of mixtures of solids," *Physica,* vol. XII, no. 5, pp. 257-271, 1946.

[52] A. Sihvola, "Self-consistency aspects of dielectric mixing theories," *IEEE Transactions on Geo-science Remote Sensing,* vol. 27, no. 4, pp. 403-415, 1989.

[53] R. Morey, A. Kovacs and G. Cox, "Electromagnetic properties of sea ice," *Cold Regions Science and Technology,* vol. 9, pp. 53-75, 1984.

[54] T. Matsuoka, S. Fujita and S. Mae, "Effect of temperature on dielectric properties of ice in the range 5-39 GHz," *Journal of Applied Physics,* vol. 80, no. 10, pp. 5884-5890, 15 November 1996.

[55] C. Matzler and U. Wegmuller, "Dielectric properties of freshwater ice at microwave frequencies," *Journal of Physics D: Applied Physics,* vol. 20, no. 12, pp. 1623-1630, 1987.

[56] P. Auty and R. Cole, "Dielectric properties of ice and solid D20," *Journal of Chemical Physics,* vol. 20, no. 8, p. 13091304, 1952.

[57] W. Phillips, "The permittivity of air at a wavelength of 10 centimeters," *Proceedings of the IRE,* vol. 38, no. 7, pp. 786-790, July 1950.

[58] A. Stogryn, "Equations for calculating the dielectric constant of saline water," *IEEE Transactions on Microwave Theory and Techniques,* vol. 19, no. 8, pp. 733-736, 1971.

[59] R. King, G. Smith, M. Owens and T. Wu, "Antennas in matter: Fundamentals, theory and applications," NASA STI/Recon Technical Report A, 1981.

[60] T. Meissner and F. Wentz, "The complex dielectric constant of sea water from microwave satellite observation," *IEEE Transactions on Geoscience and Remote Sensing,* vol. 42, no. 9, pp. 1836-1851, 2004.

[61] A. Stogryn, H. Bull, K. Rubayi and S. Iravanchy, "The microwave permittivity of sea and fresh water," GenCorp Aerojet, Azusa, CA, 1995.

[62] IEEE, "The Authoritative Dictionary of IEEE Standards Terms, Seventh Edition," in *IEEE Std 100-2000*, 11 Dec 2000, pp. 1-1362.

[63] M. Skolnik, "Introduction to radar systems," in *Chapter 2: The radar equation*, New York, NY, McGraw Hill, 2001, pp. 30-103.

[64] E. Knott, J. Shaeffer and M. Tuley, Radar Cross Section, Raleigh, NC: Scitech Publishing, 2004.

[65] D. Barton, Radar system analysis and modeling, Norwood, MA: Artech House, 2005.

[66] E. Shtager, "An Estimation of Sea Surface Influence on Radar Reflectivity of Ships," *IEEE Transactions on Antennas and Propagation,* vol. 47, no. 10, pp. 1623-1628, 1999.

[67] D. Barton, Modern Radar Systems Analysis, Norwood, MA: Artech House, 1988.

[68] FEKO, "Altair FEKO Overview," 2018. [Online]. Available: https://altairhyperworks.com/product/feko. [Accessed 29 July 2018].

[69] M. Hallikainen and D. Winebrenner, "Chapter 3: The physical basis for remotes sensing of sea ice," in *Microwave Remote Sensing of Sea Ice*, F. Carsey, Ed., Washington, DC, American Geophysical Union, 1993, pp. 29-46.

[70] C. Livingston, K. Singh and A. Gray, "Seasonal and regional variances of active/passive microwave signatures of sea ice," *IEEE Trans. on Geoscience and Remote Sensing,* Vols. GE-25, no. 2, pp. 159-174, 1987.

[71] M. Drinkwater, R. Kwok, E. Rignot, H. Israelsson, R. Onstott and D. Winebrenner, "Ch 24: Potential application of polarimetry to the classification of sea ice," in *Microwave Remote Sensing of Sea Ice*, American Geophysical Union, 1992, pp. 419-431.

[72] B. Campbell, T. Cheng, V. Garas and D. Mitchell, "Summary of Current Ice Characterization Research," National Petroleum Council, Washington, DC, September 2015.

[73] J. Orlando, R. Mann and S. Haykin, "Classification of sea-ice images using a dual-polarized radar," *IEEE Journal of Oceanic Engineering,* vol. 15, no. 3, pp. 228-238, July 1990.

[74] T. Nohara, "Detection of growlers in sea clutter using an X-band pulse-doppler radar," McMaster University, Hamilton, ON, Canada, February 1991.

[75] Rutter, "Experience: Delivering innovation and possibilities," 2018. [Online]. Available: http://www.rutter.ca/files/download/58386f1fa4766fa. [Accessed 29 July 2018].

[76] A. Parsa, "Ice age classification using cross-polarization measurement with X-band radar," in *Proceedings of the 23rd International Offshore and Polar Engineering*, Anchorage, AL, 30 June - 5 July 2013.

[77] FEKO, "FEKO Product Page," Altair Engineering, 2018. [Online]. Available: https://altairhyperworks.com/product/feko. [Accessed 29 July 2018].

[78] W. Burnside and R. Marhefka, "Antennas on Aircraft, Ships, or Any Large, Complex Environment," in *Antenna Handbook*, New York, NY, Van Nostrand Reinhold, 1988, pp. 1435-1534.

[79] M. Kragalott, M. S. Kluskens, D. A. Zolnick, W. M. Dorsey and J. A. Valenzi, "A toolset independent hybrid method for calculating antenna coupling," *IEEE Trans. Antennas Propagation,* vol. 59, no. 2, pp. 443-451, February 2011.

[80] Dassault Systemes, "CST Studio Suite Brochure," 2018. [Online]. Available: https://www.3ds.com/fileadmin/PRODUCTS/SIMULIA/PDF/brochures/CST-S2-2018_web.pdf. [Accessed 24 September 2018].

[81] ANSYS, "ANSYS HFSS Product Brochure," 2015. [Online]. Available: https://www.ansys.com/-/media/ansys/corporate/resourcelibrary/brochure/ansys-hfss-brochure-160.pdf. [Accessed 25 September 2018].

[82] A. C. Newell, B. Schluper and R. J. David, "Holographic projection to an arbitrary plane from spherical near-field measurements," in *Proceedings of AMTA Symposium*, Denver, CO, October 2001.

[83] D. Janse van Rensburg and C. Walker, "Implementation of back projection on a spherical near-field range," in *Proceedings of AMTA Symposium*, Cleveland, OH, November 2002.

[84] C. Parini, S. Gregson, J. McCormick and D. Janse van Rensburg, "Near-field range assessment," in *Theory and Practice of Modern Antenna Range Measurements*, Croydon, United Kingdom, Institution of Engineering and Technology, 2014, pp. 355-480.

[85] A. Baussard, M. Rochdi and A. Khenchaf, "PO/MEC-based scattering model for complex objects on a sea surface," *Progress in Electromagnetics Research,* vol. 111, pp. 229-251, 2011.

[86] M. Skolnik, "Chapter 7: Radar Clutter," in *Introduction to radar systems*, New York, NY, McGraw-Hill, 2001, pp. 403-481.

[87] R. Harrington, Field computation by moment methods, Wiley-IEEE Press, April 1993.

[88] R. Harrington, "The method of moments in electromagnetics," *Journal of Electromagnetic Waves and Applications,* vol. 1, no. 3, pp. 181-200, 1987.

[89] M.-J. Vinas, "See how arctic sea ice is losing its bulwark against warming summers," 28 October 2016. [Online]. Available: https://www.nasa.gov/feature/goddard/2016/arctic-sea-ice-is-losing-its-bulwark-against-warming-summers. [Accessed 9 March 2017].

[90] G. Timco and R. Frederking, "Compressive strength of sea ice sheets," *Cold Regions Science and Technology,* vol. 17, no. 3, pp. 227-240, 1990.

[91] F. Ulaby, R. Moore and A. Kung, Microwave Remote Sensing: Active and Passive, Reading, MA: Addison-Wesley Publishing, 1982.

[92] V. Gregers-Hansen and R. Mital, "An empirical sea clutter model for low grazing angles," in *IEEE Radar Conference*, Pasadena, CA, 2009.

[93] Oxford University, "Garnett, (James Clerk) Maxwell," in *The Oxford Dictionary of National Biography*, Oxford, UK, Oxford University Press, 2004.

[94] W. Stutzman and G. Thiele, Antenna Theory and Design, Hoboken, NJ: John Wiley & Sons, 2013.

[95] Vexels, "Polygonal iceberg drawing," Vector open stock, 7 May 2016. [Online]. Available: https://www.vexels.com/vectors/preview/77902/polygonal-iceberg-drawing. [Accessed 28 September 2018].